FORMATION AND PROPERTIES OF METALLIC NANOPARTICLES ON COMPOUND SEMICONDUCTOR SURFACES

by

Myungkoo Kang

A dissertation submitted in partial fulfillment
of the requirements for the degree of
Doctor of Philosophy
(Materials Science and Engineering)
in the University of Michigan
2014

Doctoral Committee:
Professor Rachel S. Goldman, Chair
Associate Professor Pei-Cheng Ku
Assistant Professor Vanessa Sih
Assistant Professor Emmanouil Kioupakis

ACKNOWLEDGEMENTS

First and foremost, I would like to express my heartfelt thanks to my thesis advisor Professor Rachel S. Goldman for guidance and patience throughout my doctoral research. I learned three precious lessons from her as follows. First, any theoretical prediction should be experimentally proved. Second, we must be open to new ideas and ready to modify our opinions if contradictory evidence emerges. Third, everything should be based on intellectual honesty. These simple yet profound principles which she taught me resulted in this dissertation. I believe that her enthusiasm and high standard for work will benefit me in the future.

I would like to thank my thesis committee members. I am deeply indebted to Professor Vanessa Sih. I was very fortunate to have worked and learned optics with her, without which this dissertation would be impossible. I also owe great appreciation to Professor Pei-Cheng Ku and Professor Emmanouil Kioupakis for fruitful discussions, strengthening my research.

This dissertation would not have been possible without the help of my collaborators. Especially, Timothy W. Saucer and Ji-Eun Lee in Professor Vanessa Sih's research group helped me conduct absorption and photoluminescence measurements.

I thank all my fellow students in Professor Rachel S. Goldman's research group for their help. In particular, I would like to thank Simon Huang, Michael V. Warren, and Sunyeol Jeon for their help with various sample characterizations, useful discussions, and encouragement.

I acknowledge the support from the National Science Foundation through the Materials Research Science and Engineering Center at the University of Michigan, grant DMR-1120923.

Finally, I sincerely thank my parents, my sister, and my fiancée. Without their love and support, I would have never finished the journey of a Ph.D. candidate.

TABLE OF CONTENTS

LIST of FIGURES

LIST OF TABLES

LIST OF APPENDICES

ABSTRACT

FORMATION AND PROPERTIES OF METALLIC NANOPARTICLES ON COMPOUND SEMICONDUCTOR SURFACES

by

Myungkoo Kang

Chair: Rachel S. Goldman

When electromagnetic radiation is incident upon metallic nanoparticles (NPs), a collective oscillation, termed a surface plasmon resonance (SPR), is generated. Recently, metallic NPs on semiconductor surfaces have enabled the generation of SPR, promising for enhanced light emission, efficient solar energy harvesting, biosensing, and metamaterials. Metallic NPs have been fabricated by focused ion beam (FIB) which has an advantage of cost-effectiveness over conventional lithography process requiring multi-step processes. Here, we report formation and properties of FIB-induced metallic NPs on compound semiconductor surfaces. Results presented in this thesis study suggest that FIB-induced Ga NPs can be a promising alternative plasmonic material.

In particular, using a combined experimental-computational approach, we discovered a universal mechanism for ion-induced NP formation, which is governed by the sputtering yield of semiconductor surfaces. We also discovered a governing mechanism for ion-induced NP motion, which is driven by thermal fluctuation and anisotropic mass transport. Furthermore, we

demonstrated Ga NP arrays with plasmon resonances with performance comparable to those of traditionally-used silver and gold NPs. We then finally demonstrated the Ga NP plasmon-induced enhancement of light emission from GaAs, which is the first ever combination of a new plasmonic material (Ga) and a new fabrication method (FIB) for the plasmon-enhanced light emission.

Chapter 1

Introduction

1.1. Overview

Surface plasmon resonance (SPR) is the collective oscillation of electrons in a solid or liquid induced by incident light.[1] The resonance occurs when the frequency of incident light matches the natural frequency of electrons oscillating against the restoring force of positive nuclei, as shown in Fig. 1.1.[1] Typical plasmonic materials are metals because of high free electron density. Recently, SPR of metallic NPs on semiconductor surfaces have shown significant promise for various applications including enhanced light emission, efficient solar energy harvesting, high sensitivity biosensing, and negative refractive index metamaterials.[1-3] It has been shown that metallic NPs enable the generation of SPR in the ultraviolet, visible, and infrared ranges, where SPR energies are inversely proportional to diameters of the metallic NPs, as shown in Fig. 1.2.[4-12]

To date, plasmonics research has focused nearly exclusively on Ag and Au NPs.[1-3] Although Ag and Au are widely available in standard wet chemistry and device processing laboratories, they are limited by low SPR energies (< 3.5 eV). On the other hand, SPR in the range 0.8 to 5.8 eV

were recently reported for Ga NPs with average NP diameters ranging from 10 to 300 nm, as shown in Fig. 1.2.[4-12] Also, Ag suffers from SPR damping due to air-induced surface corrosion.[4] Furthermore, a comparison of literature reports for the optical constants of liquid (amorphous) Ga and Ag NPs reveals conductivity values which are of the same order of magnitude, presumably leading to low dissipation losses.[6] Thus, both the plasmon resonance tuning and the low dissipation losses for Ga NPs are very promising for plasmonic nanomaterials.

Existing methods for the fabrication of these metallic NPs require complex multi-level processing such as lithography. Meanwhile, ion irradiation-induced surface NP formation involves the self-assembly process for achieving dense arrays of metallic NPs on semiconductor surfaces. In this thesis, we explore a new plasmonic material (Ga) fabricated via FIB irradiation for enhancing energy conversion efficiencies of semiconductors. Here, we report formation and properties of FIB-induced metallic NPs on compound semiconductor surfaces.

1.2. Device applications of metallic nanoparticles

To date, SPR of metallic NPs on semiconductor surfaces have been utilized for a wide range of applications, which involves light-matter interactions, including enhanced light emission,[13] efficient solar energy harvesting,[14] high sensitivity biosensing,[15] and negative refractive index metamaterials.[16] Figure 1.3(a) shows a schematic diagram of a light emitting device where metallic NPs enhances the light emission of semiconductor layers.[13] Figure 1.3(b) presents a schematic diagram of a solar cell structure where metallic NPs enhance the absorption of incident electromagnetic wave, leading to increased energy conversion.[14] Figure 1.3(c) shows a schematic circuit diagram of a metamaterial consisting of 3D periodic arrays of spherical

metallic NPs where a specific combination of metallic NP diameter, interparticle distance and interplanar spacing is expected to show SPR-induced negative refraction.[15] Figure 1.3(d) presents a diagram of a biosensor where metallic NPs detect biomolecules via SPR-induced energy transfer between metallic NPs and biomolecules.[16]

In particular, this thesis focuses on the influence of metallic NP on optical properties of semiconductors, and therefore, it is important to discuss how SPR of metallic NPs is related to the light emission efficiency of semiconductor surfaces. Figure 1.4(a) shows a typical PL spectra taken from GaAs layers grown on a GaAs substrate in Goldman group Gen-II molecular beam epitaxy system. To enhance the PL efficiency of semiconductors such as GaAs layers, SPR of metallic NPs have been utilized to tailor light-matter interaction in metal-semiconductor composites.[1,13,17] The metallic NP-enhanced light emission efficiency of semiconductor surfaces has been explained mainly in terms of enhanced spontaneous emission rate.[13] Meanwhile, the influence of surface metallic NPs on the incident light absorption efficiency of semiconductor layers has been a remaining issue for the metallic NP SPR-enhanced light emission efficiency of semiconductor surfaces. Figure 1.4(b) and 1.4(c) shows a band diagram and a schematic illustration where the relative influences of metallic NP SPR on absorption and emission processes in semiconductor layers are considered. One of this thesis study's goals is studying the influence of Ga NP diameter-dependent SPR on both absorption and emission processes.

1.3. Optical properties of metallic nanoparticles

We need a new approach to the fabrication and design of plasmonic nanomaterials for tailored light-matter interactions to overcome limitations of traditionally used plasmonic metals

including Ag and Au: this includes (1) new metals and (2) new approaches to the fabrication of ensemble arrays of metals. Ga NPs show promise in a wide spectral range from near-infrared to UV, as shown in Fig. 1.2. Also, Ga NPs do not suffer from SPR damping due to air-induced surface corrosion.[4] Furthermore, Ga (liquid), Ag, and Au NPs possess the quality factor[12-15] and optical loss values[16,17] that are of the same order of magnitude, as shown in Table 1.1. Thus, both tunability and corrosion-induced damping tolerance of SPR and the low dissipation losses for Ga NPs are promising for plasmonic nanomaterials.

Table 1.1 Values of the quality factor and optical loss for Ag, Au, and Ga NPs

	Ag	**Au**	**Ga**
***Q* (quality factor)**[12-15]	3.8 - 9.4	1.0 - 14.0	1.9 - 3.5
ε" (optical loss)[16,17]	0.5 - 3.7	1.0 - 5.8	4.2 - 17.5

1.4. Fabrication of metallic nanoparticles

The formation of Ga NPs have been reported using various Ga-rich conditions including exposure to Ga flux,[18-21] thermal annealing in the absence of a group V flux,[22-26] and ion irradiation,[27-35] as shown in Fig. 1.5. In the case of Ga exposure on III-V semiconductor surfaces, formation of Ga NPs has been reported on both GaAs and GaN surfaces.[18-21] Furthermore, the thermal annealing temperatures at which the surfaces become Ga-rich have been reported for several Ga-V semiconductor surfaces, and, tend to increase in the order of increasing surface binding energies.[22-26] Finally, in the case of FIB irradiation of III-V semiconductor surfaces, group V

elements are preferentially sputtered, forming a group III-rich ion-milled region. With continued FIB irradiation beyond a threshold ion dose, group III-rich NPs are observed.[27-35]

1.5. Dissertation Objectives

The first part of this thesis work focuses on the formation of metallic NPs on ion-irradiated compound semiconductor surfaces. The influence of ion dose on the formation of group III-rich NPs on III-V compounds was examined. We compute the ion doses needed to fully deplete group V elements from the surfaces. We compare the computed group V depletion doses with the measured threshold ion doses for nucleation of group III-rich NPs on a wide variety of III-V compound semiconductor surfaces. We propose a universal mechanism which describes a key role of the total sputtering yield of each III-V compound in the metallic NP formation.

The second part of this thesis is devoted to the motion of metallic NPs on ion-irradiated compound semiconductor surfaces. The origins of ion irradiation-induced Ga NP motion on GaAs surfaces were examined. Ion irradiation of GaAs surfaces induces random walks of Ga NPs, which are biased in the direction opposite to that of ion beam scanning. We investigate the influence of off-normal ion irradiation on the instantaneous and drift velocities of the biased random Ga NPs motion. We discuss the origins of biased random walks in terms of ion irradiation-induced thermal fluctuations and the anisotropic mass transport.

The third part of this thesis describes the optical properties of FIB-fabricated metallic NP arrays on compound semiconductor surfaces. The influence of particle and chain diameter on SPR energy of 2D and 1D Ga NP arrays fabricated using FIB irradiation of GaN surfaces was examined. We present the extinction spectra of Ga NP arrays on GaN surfaces, and discuss their

SPR energies as a function of NP or chain diameter. We also compare the SPR quality factors of Ga NP arrays with those reported from Ag and Au NPs to examine Ga NPs as a promising alternative plasmonic material.

The final part of this thesis discusses the utilization of FIB-fabricated metallic NP arrays for the enhancement of compound semiconductor energy conversion efficiency. The influence of surface Ga NPs on the enhancement of GaAs PL efficiency was examined. We utilize off-normal FIB irradiation of GaAs surfaces to fabricate close-packed Ga NP arrays. We present the enhancement in PL efficiency as a function of the Ga NP diameter. It has been reported that SPR-enhanced PL of semiconductor surfaces has been mainly discussed in terms of the enhanced spontaneous emission rate.[13] However, in our case, we discuss origins of the PL enhancement in terms of roles of SPR in both the absorption and emission processes.

1.6. Outline of the Dissertation

This dissertation is organized as follows. Chapter 2 describes the experimental procedures used for this thesis work, including focused ion beam, scanning electron microscopy, molecular beam epitaxy, atomic force microscopy, transmission electron microscopy, x-ray energy dispersive spectroscopy, and absorption and photoluminescence spectroscopy.

In Chapter 3, we have examined the formation of ion irradiation-induced NPs consisting of Ga droplets on Ga-V surfaces, In islands on In-V surfaces, and Al islands on Al-V surfaces. The computed group V depletion doses agree well with the experimental threshold ion doses for nucleation of group III-rich droplets or islands. Since the group V depletion dose is inversely proportional to the sputtering yield of each III-V compound, we attribute the NP formation to a

mechanism based upon sputtering. This physical mechanism may be used as a guide for nucleation of droplets or islands on a wide variety of compound semiconductor surfaces.

In Chapter 4, we have examined origins of ion irradiation-induced Ga NP motion on GaAs surfaces. FIB irradiation of GaAs surfaces induces random walks of Ga NPs, biased opposite to the ion beam scan direction. The instantaneous velocity of Ga NPs is constant, while the drift velocity of Ga NPs is linearly dependent on off-normal ion irradiation angle, due to an enhanced difference in surface non-stoichiometry. It is hypothesized that the random walks are initiated by ion irradiation-induced thermal fluctuations, with biasing driven by anisotropic mass transport induced by the difference in surface non-stoichiometry.

In Chapter 5, we have demonstrated FIB-induced 2D square (1D chain) arrays of Ga NPs via pre-patterned holes on GaN surfaces where interhole spacing, hole diameter, and hole depth determine interparticle (interchain) spacing, particle (chain) diameter, and the array distribution, respectively. Extinction spectra of 2D square and 1D chain arrays reveal SPR energies in the visible and near-IR ranges. Interestingly, the SPR energies are blue-shifted with decreasing NP or chain diameter, due to particle diameter-dependent dipole interactions within the metallic NPs. This approach provides an opportunity to tune SPR over a wide energy range, with Q_{SPR} values comparable to those reported for Ag and Au NPs.

In Chapter 6, we have examined the influence of surface Ga NPs on the enhancement of GaAs PL efficiency. We computed the absorption spectra of hemispheroidally-shaped Ga NPs on GaAs surfaces using Mie's analytical solution to Maxwell's equations. We fabricated close-packed arrays of Ga NPs via off-normal FIB irradiation of GaAs surfaces, and we measured the enhancement of PL efficiency as a function of Ga NP diameter. The maximum PL enhancement occurs for the value of Ga NP diameter predicted to maximize the incident EM field

enhancement. The PL enhancement is driven by the SPR-induced enhancement of the incident EM field which overwhelms the SPR-induced suppression of the light emission. Finally in Chapter 7, we present a summary and outlines for future work.

1.7. Figures and references

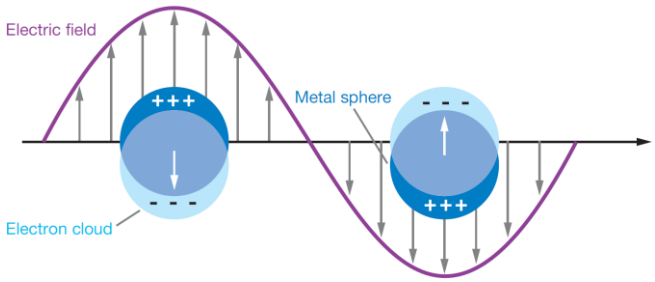

Fig. 1.1 A schematic diagram illustrating surface plasmon resonance (SPR) of metallic NPs induced by electric field. Typical metallic NPs with SPR include Ag, Au, Ga, Al, In, etc.[1]

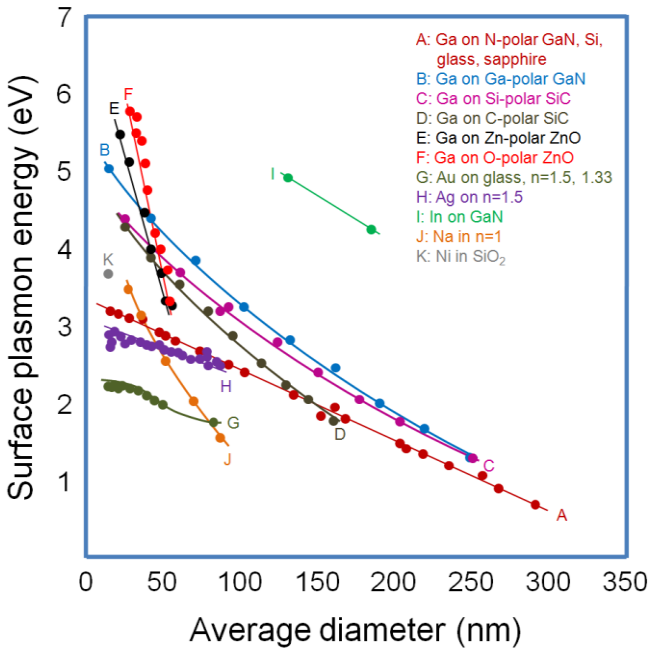

Fig. 1.2 A plot of surface plasmon resonance (SPR) energy vs. average diameter of various metallic nanoparticles (NPs) including Ga, Au, Ag, In, Na, and Ni.[4-12] The plot reveals that SPR energies of metallic NPs decrease with increasing average diameter of NPs. Especially, SPR energies of Ga NPs are tunable in the wide range 0.8 to 5.8 eV.

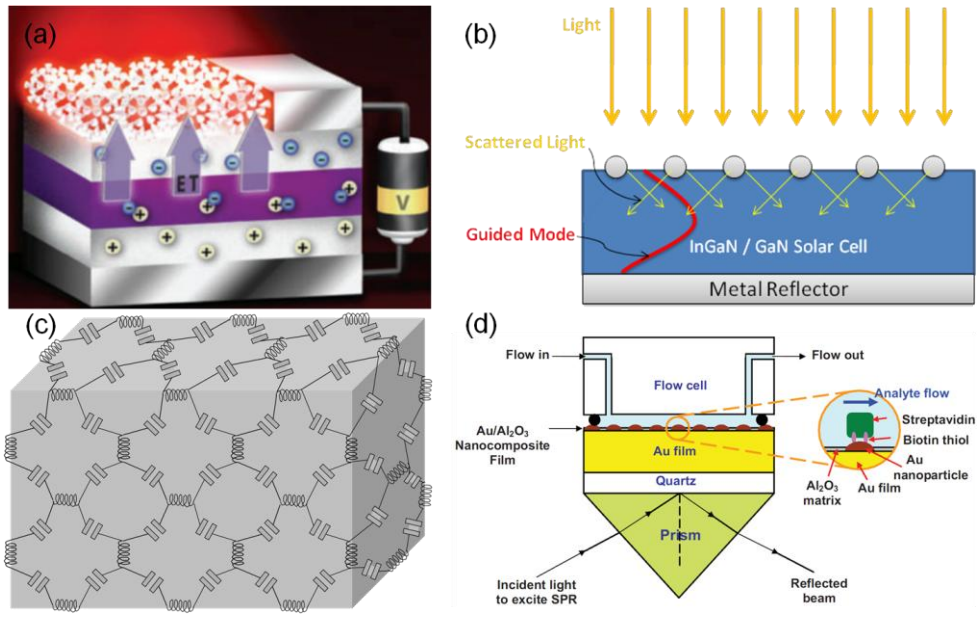

Fig. 1.3 Schematic diagrams of metallic NP SPR-utilized (a) light emitting device,[13] (b) solar cell,[14] (c) metamaterial,[15] and (d) biosensor.[16]

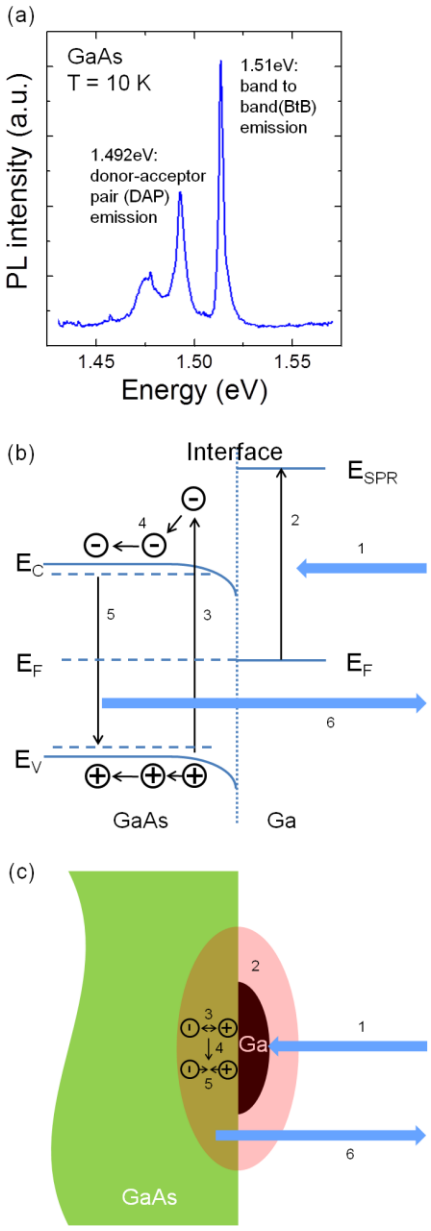

Fig. 1.4 (a) PL spectrum of GaAs layers grown in Goldman group Gen II molecular beam epitaxy system (b) a band diagram showing the process for Ga NP SPR-enhanced GaAs PL efficiency (c) a schematic diagram illustrating the process for Ga NP SPR-enhanced GaAs PL efficiency. In (b) and (c), the process includes 1: EM wave incident upon Ga NPs, 2: SPR-induced Evanescent field, 3: Enhanced absorption, 4: Carrier migration, 5: Carrier recombination, and 6: Emission ($E_{DAP} = E_{SPR}$) or Loss ($E_{DAP} \neq E_{SPR}$).

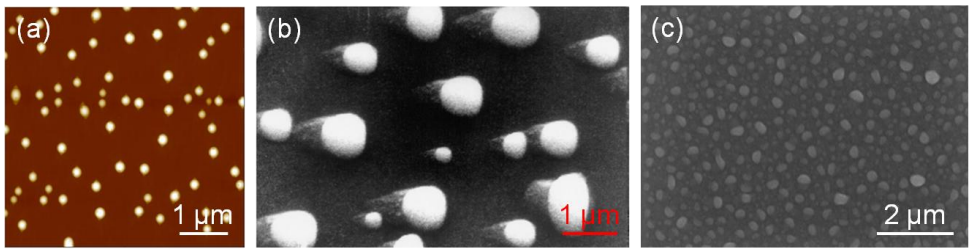

Fig. 1.5 Formation of Ga NPs using various Ga-rich conditions including (a) exposure to Ga flux, (b) thermal annealing in the absence of a group V flux,[22] and (c) ion irradiation.

[1]K. A. Willets and R. P. Van Duyne, *Annu. Rev. Phy. Chem.* **58**, 267 (2007).

[2]S. J. Oldenburg, J. B. Jackson, S. L. Westcott, and N. J. Halas, *Appl. Phys. Lett.* **75**, 2897 (1999).

[3]S. J. Oldenburg, R. D. Averitt, S. L. Westcott, and N. J. Halas, *Chem. Phys. Lett.* **288**, 243 (1998).

[4]P. C. Wu, M. Losurdo, T. H. Kim, M. Giangregorio, G. Bruno, H. O. Everitt, and A. S. Brown, *Langmuir* **25**, 924 (2009).

[5]P. C. Wu, T. H. Kim, A. S. Brown, M. Losurdo, G. Bruno, and H. O. Everitt, *Appl. Phys. Lett.* **90**, 103119 (2007).

[6]P. C. Wu, C. G. Khoury, T. H. Kim, Y. Yang, M. Losurdo, G. V. Bianco, T. Vo-Dinh, A. S. Brown, and H. O. Everitt. *J. Am. Chem. Soc.* **131**, 12032 (2009).

[7]P. C. Wu, M. Losurdo, T. H. Kim, S. Choi, G. Bruno, and A. S. Brown. *J. Vac. Sci. Technol. B* **25**, 1019 (2007).

[8]A. Derkachova and K. Kolwas. *Eur. Phys. J. Special Topics* **144**, 93 (2007).

[9]B. N. Khlebtsov and N. G. Khlebtsov. *J. Phys. Chem. C* **111**, 11516 (2007).

[10]A. Liebsch. *Phys. Rev. B* **48**, 11317 (1993).

[11]K. Kolwas, A. Derkachova, and M. Shopa. *J. Quant. Spectrosc. Ra.* **110**, 1490 (2009).

[12]Z. L. Wang and J. M. Cowley. *Ultramicroscopy* **23**, 97 (1987).

[13]M. Stockman, *Nat. Mater.* **3**, 423 (2004).

[14]V. E. Ferry et al., *Adv. Mater.* **22**, 4794 (2010).

[15]A. Alu, A. Salandrino, and N. Engheta, *Opt. Exp.* **14**, 1557 (2006).

[16]S. Gao et al., *Adv. Funct. Mater.* **20**, 78 (2010).

[17]S. A. Maier, *Plasmonics: Fundamentals and Applications* (Springer, New York, 2007).

[18]Z. Y. AbuWaar, Z. M. Wang, J. H. Lee, and G. J. Salamo, *Nanotechnology* **17**, 4037 (2006).

[19]T. Suzuki and T. Nishinaga, *J. Cryst. Growth* **142**, 49 (1994).

[20]P. C. Wu, M. Losurdo, T. H. Kim, M. Giangregorio, G. Bruno, H. O. Everitt, and A. S. Brown, *Langmuir* **25**, 924 (2009).

[21]M. Zhang, P. Bhattacharya, W. Guo, and A. Banerjee, *Appl. Phys. Lett.* **96**, 132103 (2010).

[22]M. Nouaoura, F. W. O. DaSilva, N. Bertru, M. Rouanet, A. Tahraoui, W. Oueini, J. Bonnet, and L. Lassabatere, *J. Cryst. Growth* **172**, 37 (1997).

[23]F. Riesz, L. Dobos, and J. Karanyi, *J. Vac. Sci. Technol. B* **16**, 2672 (1998).

[24]H. Rokugawa and S. Adachi, *Surf. Interface Anal.* **42**, 88 (2010).

[25]H. Morota and S. Adachi, *J. Appl. Phys.* **105**, 043508 (2009).

[26]S. Y. Karpov, O. V. Bord, R. A. Talalaev, and Y. N. Makarov, *Mater. Sci. Eng. B* **82**, 22 (2001).

[27]F. Krok, *Vacuum* **83**, 745 (2009).

[28]M. Bouslama, C. Jardin, and M. Ghamnia, *Vacuum* **46**, 143 (1995).

[29]A. Lugstein, M. Weil, B. Basnar, C. Tomastik, and E. Bertagnolli, *Nucl. Instrum. Methods Phys. Res. B* **222**, 91 (2004).

[30]J. L. Plaza and E. Dieguez, *Solid State Ionics* **178**, 1576 (2007).

[31]M. Tanemura, T. Aoyama, A. Otani, M. Ukita, F. Okuyama, and T. K. Chini, *Surf. Sci.* **376**, 163 (1997).

[32]S. K. Tan and A. T. S. Wee, *J. Vac. Sci. Technol. B* **24**, 1444 (2006).

[33]M. Tanemura, S. Aoyama, Y. Fujimoto, and F. Okuyama, *Nucl. Instrum. Methods Phys. Res. B* **61**, 451 (1991).

[34]J. H. Wu, W. Ye, B. L. Cardozo, D. Saltzman, K. Sun, H. Sun, J. F. Mansfield, and R. S. Goldman, *Appl. Phys. Lett.* **95**, 153107 (2009).

[35]A. J. Steckl and I. Chyr, *J. Vac. Sci. Technol. B* **17**, 362 (1999).

Chapter 2

Experimental Procedures

2.1 Overview

This chapter describes the experimental procedures used for the fabrication, characterization, and measurements for focused ion beam (FIB)-induced Group III-rich nanoparticles (NPs) on compound semiconductor surfaces. For these experiments, undoped semi-insulating GaAs (001) and (111) substrates, 1 μm GaAs buffer layers grown on GaAs (001) substrate, GaN (001) substrates, GaSb (001) substrates, GaP (001) substrates, InSb (001) substrates, InAs (001) substrates, InP (001) substrates, and AlAs (001) substrate were irradiated with Ga^+ FIB. The post-NP formation (real-time motion) imaging was performed via the collection of electron (ion) beam-induced secondary electrons using the secondary electron detector. Following FIB irradiation, surface morphologies were examined using scanning electron microscopy (SEM) and atomic force microscopy (AFM). The structure and composition of FIB-fabricated NPs were analyzed using transmission electron microscopy (TEM) and x-ray energy dispersive spectroscopy (XEDS) with the assistance of Jia-Hung Wu, Weifeng Ye, and Michael V. Warren in Goldman group. To examine the influence of incident electromagnetic wave on Ga NPs and the influence of Ga NPs on light emission efficiency of

GaAs surfaces, absorption and photoluminescence measurements were carried out with the assistance of Timothy W. Saucer and Ji-Eun Lee in Sih group.

2.2 Focused Ion Beam

All FIB irradiation described in this thesis was carried out in a FEI NOVA 200 dual beam workstation shown schematically in Fig. 2.1. The FIB system consists of an ion beam column, an electron beam column, an energy dispersive x-ray, and secondary electron detectors, in a high vacuum chamber with 10^{-5} torr base pressure. This system combines a high-resolution secondary electron microscope for surface imaging, a Ga^{+} FIB for irradiation and patterning, and x-ray microanalysis for characterization. During FIB irradiation, surface imaging and x-ray microanalysis are achieved via the collection of secondary electrons and characteristic x-rays, respectively.

For details of FIB irradiation parameters and target materials unique to each of projects described in this thesis, we first introduce the "codes" for projects as shown in table 2.1, and the details are followed in table 2.2.

Table 2.1. The "codes" for projects described in this thesis

Project	Code
Universal mechanism for ion-induced nanostructure formation on III-V compound semiconductor surfaces[1]	*Formation*
Origins of ion irradiation-induced Ga nanoparticle motion on GaAs surfaces[2]	*Motion*
Surface plasmon resonances of Ga nanoparticle arrays[3]	*SPR*
Ga nanoparticle-enhanced photoluminescence of GaAs[4]	*PL*

Table 2.2. Ion energy, current, dwell time, dose, dose rate, pitch, magnification, angle, irradiation time, and target materials used in this study

	Formation	Motion	SPR	PL
Ion Energy (keV)	30	30	30	5
Ion Current (pA)	40 - 60	300	50	230
Dwell Time (μs)	10	0.3	100	0.05
Ion Dose (/cm^2)	4.0×10^{14} - 2.0×10^{18}	6.3×10^{17}	1.0×10^{18}	3.0×10^{17}
Ion Dose Rate (/cm^{2}s)	1.8×10^{14} - 2.6×10^{14}	5.3×10^{15}	8.3×10^{14}	1.0×10^{15}
Pitch (nm)	12.7	12.7	7.1	6.1
Magnification (x)	10000	20000	20000	10000
Angle (^{o})	0	0 - 60	0	26 - 82
Irradiation Time (s)	1.8 - 9100	120	1200	300
Target Material	GaAs, GaN, GaP, GaSb, InAs, InP, InSb, AlAs	GaAs	GaN	GaAs

2.3 Scanning Electron microscopy

In-situ FEI Nova 200 Nanolab dual-beam scanning electron microscopy (SEM) system was used to image FIB-fabricated nanostructures on III-V compound semiconductors. For each image, 10 kV voltage, 98 pA current, and 50 ns dwell time were used for electron beams. All SEM images were collected at normal incidence except for studies of Ga NP motion where ion beam-induced secondary electron imaging at θ_{ion} = 0 - 60^o was used to record movies of θ_{ion}-dependent Ga NP motion.

2.4 Atomic Force Microscopy

Atomic force microscopy (AFM) was used to quantify the surface topography following FIB irradiation on III-V compound semiconductor surface. Tapping-mode AFM was performed using a Digital Instruments Nanoscope III AFM. For the AFM probe, we used ultra-sharp Nanoworld AFM probes with tip radius < 10 nm, tip length = 14 μm, resonant frequency = 300 kHz, and force constant 40 N/m. Typically, a bowing occurs in the AFM image, due to the curved motion of the probe over the surface. Thus, AFM images were flattened by subtracting a quadratic background in the lateral directions using Scanning Probe Image Processor (SPIP).

2.5 Transmission Electron Microscopy/X-ray Energy Dispersive Spectroscopy

For transmission electron microscopy (TEM) studies on Ga NPs on GaAs and In NPs on InAs surfaces, cross-sectional samples were prepared by mechanical polishing followed by argon ion milling at 77 K. The samples were then mounted on Mo grid and polished to ~ 100 nm thickness. The TEM samples were subsequently transferred to a FIB workstation for nanostructure fabrication. TEM imaging and selected area diffraction (SAD) were carried out in a JEOL 2010F operating at 200 kV and a JEOL 3011 operating at 300 kV. X-ray energy dispersive spectroscopy (XEDS) maps were collected using scanning transmission electron microscopy (STEM) in the JEOL 2010F.

For TEM studies on Ga NPs on GaN surfaces, cross-sectional specimens of Ga NP arrays on GaN surfaces were prepared by ion milling followed by lift-out processing in a FEI Helios

Nanolab 650 FIB. The sample was then mounted on a Mo grid and ion polished to ~ 100 nm. TEM imaging and SAD were carried out in a JEOL 3011 operating at 300 kV.

2.6 Absorption and Photoluminescence Spectroscopy

Spatially-resolved absorption measurements in the wavelength range 400 nm to 1100 nm were performed using a tungsten halogen lamp and a 0.7 NA objective, in a confocal microscope configuration. Using a liquid nitrogen cooled CCD detector and 0.75 m spectrometer, room temperature transmittance (T) and reflectance (R) spectra were collected from both the patterned and unpatterned regions of the surface. T and R from the patterned area were then obtained by subtracting the background spectra from the unpatterned area. Finally, maxima in the extinction spectra, $E = \log_{10}[(1 - R)/T]$ were attributed to surface plasmon resonances.

Spatially-resolved PL measurements were performed on the samples mounted in a helium flow cryostat operating at 10K, using a 633 nm CW Helium-Neon laser. Pump powers varied from 0.04 to 4.34 mW, as measured before a 0.7 NA infinity corrected objective. The diameter of the normally-incident focused laser on the sample was 5 μm, and a confocal microscope configuration was used to collect the emission from a 3 μm diameter spot within only the FIB-patterned regions. PL was recorded using a 150 G/mm reflection grating in a 0.75 m spectrometer and a liquid nitrogen cooled Si CCD detector. To take into account the Ga NP size dependence of the pump laser absorption and DAP emission, for each sample, the PL spectrum was normalized by the integrated intensity of the absorbed laser light, defined as the difference between the laser spectrum and laser-induced surface reflectivity. PL enhancement ratios were

then defined as the ratio of the normalized PL intensities for regions of the GaAs layer with and without Ga NPs.

2.7. Figures and references

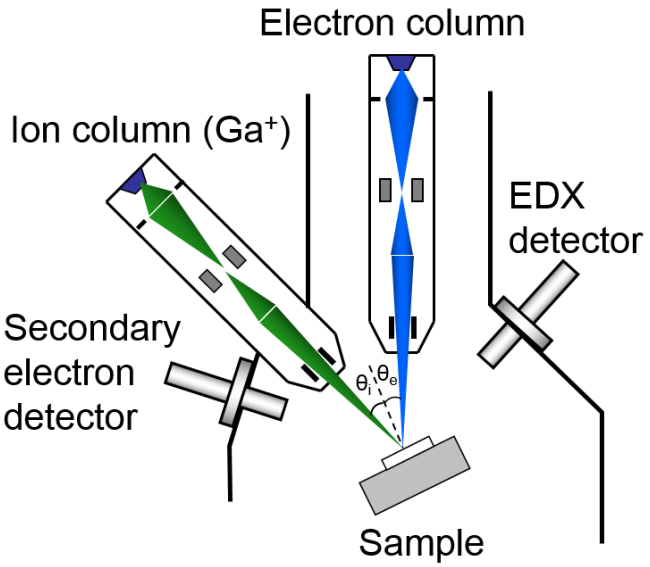

Fig. 2.1. Schematic of NOVA 200 dual beam workstation. The ion (electron) beam angle of incidence, θ_i (θ_e) is defined as the angle between the incident ion (electron) beam and the sample surface normal represented by the dashed line. The angle between the ion and electron beam columns is fixed at 52^o, and the sample can be tilted. Therefore, for example, the sample must be tilted to 52^o with respect to the electron beam for normal-incidence FIB irradiation.

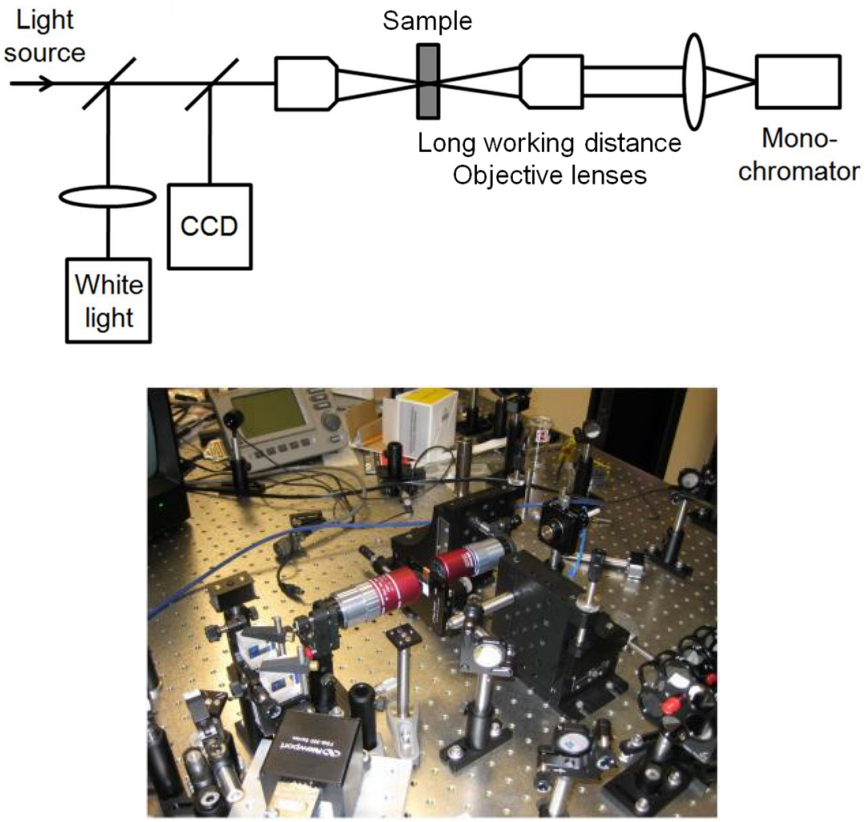

Fig. 2.2. Optics set-up for transmittance, reflectance, and photoluminescence measurements: (a) The incident electromagnetic waves on a sample come from the Tungsten halogen white light source for transmittance and reflectance measurements or the HeNe laser source with specific energy for photoluminescence measurement. The CCD detects responses of a sample under incident electromagnetic waves. (b) A photo of experimental set-up for these measurements in Sih group at Univ. of Michigan, Ann Arbor.

[1]M. Kang, J. H. Wu, S. Huang, M. V. Warren, Y. Jiang, E. A. Robb, and R. S. Goldman, *Appl. Phys. Lett.* **101**, 082101 (2012).

[2]M. Kang, J. H. Wu, D. L. Sofferman, I. Beskin, H. Y. Chen, K. Thornton, and R. S. Goldman, *Appl. Phys. Lett.* **103**, 072115 (2013).

[3]M. Kang, T. W. Saucer, M. V. Warren, J. H. Wu, V. Sih, and R. S. Goldman, *Appl. Phys. Lett.* **101**, 081905 (2012).

[4]M. Kang, A. A. Al-Heji, J. -E. Lee, T. W. Saucer, S. Jeon, J. H. Wu, L. Zhao, A. L. Katzenstein, D. L. Sofferman, V. Sih, and R. S. Goldman, *Appl. Phys. Lett.* **103**, 101903 (2013).

Chapter 3

Universal mechanism for ion-induced nanostructure formation on III-V compound semiconductor surfaces

3.1. Overview

We have examined the formation of nanostructures on ion-irradiated compound semiconductor surfaces. We computed the ion doses needed to fully deplete group V elements from the surfaces. These group V depletion doses are in good agreement with the measured threshold ion doses for nucleation of group III-rich nanostructures on a wide variety of III-V compound semiconductor surfaces. Since the group V depletion doses decrease with increasing sputtering yield, these results suggest a universal nanostructure formation mechanism which depends upon the total sputtering yield of each III-V compound.

This chapter opens with background information, including a review of ion-induced nanostructure formation on compound semiconductor surfaces. Next, the experimental details for the studies of ion-induced nanostructure formation are described. We then discuss the structure and composition of ion-induced nanostructures. Finally, we consider the ion dose dependence of ion-induced nanostructure formation in terms of sputtering yield of each III-V compound. The chapter concludes with a summary.

3.2. Background

Recently, metallic nanostructures within semiconductors have shown significant promise for various applications including enhanced photoluminescence,[1] efficient solar energy harvesting,[2] high sensitivity biosensing,[3,4] and negative index metamaterials.[5] Existing methods for fabrication of ordered nanostructure arrays require complex multi-level lithographic processing. On the other hand, ion-irradiation of semiconductor surfaces has emerged as a promising approach to the self-organization of nanostructures.[6–17] Recently, many groups have reported group III-rich nanostructures on ion-irradiated III-V compound surfaces, attributing their formation to preferential group V sputtering, i.e., $Y_V > Y_{III}$.[6–17] On the other hand, for ultra high vacuum (UHV)-prepared and ion-irradiated GaSb and AlAs, group III-rich nanostructures were not reported. In the case of GaSb, following low energy Ar^+ irradiation, Sb-rich surfaces were observed.[18] For AlAs, following UHV Ga^+ focused ion beam (FIB) irradiation, group III nanostructures were not observed, presumably due to the limited range of ion doses utilized.[16] Here, we report on investigations of FIB irradiation of a wide range of compound semiconductor surfaces. For each surface, we computed the ion dose needed to fully deplete group V elements, which we term the "group V depletion doses." The group V depletion doses are in good agreement with the measured threshold ion doses for nanostructure formation. Since the group V depletion doses are inversely proportional to the sputtering yield of each III–V compound, these results suggest a universal mechanism for group III-rich nanostructure formation which depends on sputtering.

3.3. Experimental procedures

For this study, semi-insulating compound semiconductor surfaces, including InSb, InAs, GaSb, GaAs, InP, GaP, AlAs, and GaN were irradiated using a dual-beam Ga^+ FIB system. Under normal incidence, 30 keV Ga^+ ions, with 40-60 pA ion beam current, were implanted over an area of 143 μm^2, in a continuous raster scan mode. Since sputtering yields are dose rate-dependent,[19] we explore dose rates ranging from 1.8×10^{14} to 2.6×10^{14} /cm^2·s, using ion currents ranging from 40 to 60 pA. For each fixed dose rate, ion doses were varied from ~ 4.0×10^{14} to 2.0×10^{18} /cm^2. Following irradiation, a combination of in-situ scanning electron microscopy (SEM) and ex-situ atomic force microscopy (AFM) were utilized to quantify the size distributions of the nanostructures. The ion doses for which > 60 ± 20 nm-sized nanostructures were visible via ex-situ AFM were identified as the "threshold ion doses." For 40 to 60 pA currents, the threshold ion doses ranged from $6.0 \pm 0.5 \times 10^{14}$ to $1.3 \pm 0.5 \times 10^{18}$ /cm^2, corresponding to minimum and maximum milled depths ranging from 11 ± 1 to 83 ± 2 nm. *Ex-situ* transmission electron microscopy (TEM) and x-ray energy dispersive spectroscopy (XEDS) in the TEM were used by Jia-Hung Wu and Weifeng Ye in Goldman group to determine the structure and composition of FIB-synthesized nanostructures. For TEM studies, cross-sectional samples were prepared by mechanical polishing followed by argon ion milling at 77 K. The samples were then mounted on Mo grid and polished to ~ 100 nm thickness. The TEM samples were subsequently transferred to a FIB workstation for nanostructure fabrication. TEM imaging and selected area diffraction (SAD) were carried out in a JEOL 2010F operating at 200 kV and a JEOL 3011 operating at 300 kV. XEDS maps were collected using scanning transmission electron microscopy (STEM) in the JEOL 2010F.

3.4. Morphology of nanostructures

SEM images of 50 pA FIB-irradiated InSb, InAs, GaSb, GaAs, InP, GaP, AlAs, and GaN surfaces up to the threshold ion doses are presented in Fig. 3.1(a)-3.1(j). In each image, bright features corresponding to In islands on InSb, InAs, and InP; Ga droplets on GaSb, GaAs, GaP, and GaN; and Al islands on AlAs are observed. The size distributions are shown in Appendix B, and fits to a log-normal distribution yield average lateral sizes ranging from 60 ± 20 to 80 ± 20 nm. Due to the log-normal size distributions, the nanostructure formation process is likely dominated by coalescence via nanostructure migration, often termed "dynamic coalescence."[13]

3.5. Structure and composition of nanostructures on GaAs

TEM images and corresponding SAD patterns from FIB-irradiated GaAs and InAs surfaces are shown in Figs. 3.2(a)-3.2(d), respectively. For GaAs surfaces, the TEM image in Fig. 3.2(a) reveals features including a Ga droplet and a ~ 40 nm Ga-rich transition layer between the droplet and GaAs substrate. The corresponding SAD patterns for FIB-irradiated GaAs in Fig. 3.2(b) reveal a diffuse ring due to amorphous Ga and spotty rings with *d*-spacings = 3.26 ± 0.01, 2.00 ± 0.01, and 1.41 ± 0.01 Å, similar to {111}, {220}, and {400} interplanar spacings of pure ZB GaAs, which are 3.26, 2.00, and 1.41 Å, respectively.[13] Figures 3.3(a) and 3.3(b) present a bright-field STEM image and an XEDS map for a Ga droplet on GaAs where red and green correspond to Ga and As, respectively. The red color of the droplet in Fig. 3.3(b) indicates that it is Ga-rich. We note that similar Ga-rich droplets were observed on ion-irradiated

GaSb, GaP, and GaN surfaces. Since the melting temperature for a 60 nm-sized Ga nanostructure is expected to be ~ 290K,[20] it is likely that the Ga droplets are liquid.

3.6. Structure and composition of nanostructures on InAs

For InAs surfaces, the TEM image in Fig. 3.2(c) reveals features including In islands and an In-rich InAs substrate. In Fig. 3.2(d), the corresponding SAD patterns for FIB-irradiated InAs reveal a diffuse ring with *d*-spacing = 2.26 ± 0.01 Å, similar to a {332} interplanar spacing of polycrystalline In_2O_3, and spotty rings with *d*-spacings = 2.41 ± 0.01 and 2.64 ± 0.01 Å, similar to {002} and {101} interplanar spacings of polycrystalline In.[21] Figures 3.3(c) and 3.3(d) present a dark-field STEM image and an XEDS map for an In island on InAs where white, green, and red correspond to In, As, and Ga, respectively. The white color of the island suggests that it is In-rich. Similar In-rich islands were observed on ion-irradiated InSb and InP surfaces. In this case, for a 60 nm-sized In nanostructure, the melting temperature is expected to be ~ 410 K;[22] thus, it is likely that the In nanostructures are solid.

3.7. Nanostructure formation mechanism

Figure 3.4 presents both measured (black) threshold ion doses and computed (red) group V depletion doses vs. sputtering yields for each compound semiconductor, calculated using linear cascade sputtering theory.[23-26] Interestingly, the plot reveals measured threshold ion doses which decrease with increasing sputtering yield. Similar trends were observed for 40, 50, and 60 pA ion currents (1.8×10^{14}, 2.2×10^{14}, and 2.6×10^{14} /cm^2·s dose rates). To consider a mechanism

for nanostructure formation based upon group V depletion, we calculate the non-stoichiometry, δ, defined as $III_{1+\delta}V_{1-\delta}$ in the group III-rich region. During the ion-irradiation process, group III and V elements are both sputtered and re-deposited. However, the re-deposited atoms are only weakly bound to the surface, and are therefore expected to play a negligible role in the nanostructure formation process. We assume that the incident Ga^+ ions contribute to sputtering, but are not incorporated into the nanostructures. Therefore, following ion-irradiation for a time t, δ is given by the following:

$$\delta(t) = \frac{(Y_V - Y_{III}) \cdot \frac{dN_{ion}}{dt} \cdot t}{[2N_{III}(0) - (Y_{III-V})_i \cdot \frac{dN_{ion}}{dt} \cdot t]} \quad (1)$$

where $N_{III}(0)$ is initial number of group III elements at the beam spot prior to irradiation; dN_{ion}/dt is the Ga^+ ion dose rate; t is the irradiation time; $Y_{III(V)}$ and Y_{III-V} are the sputtering yields for group III (V) elements and the $III_{1+\delta}V_{1-\delta}$ compound; i is ith scan in a continuous raster scan mode. For successive passes of FIB irradiation, Y_{III-V} becomes

$$(Y_{III-V})_{i+1} = Y_{III} + (1-\delta_i)Y_V \quad (2)$$

Using Eqs. (1) and (2), we computed δ in the regions of beam spot overlap as a function of ion dose. The dose at which $\delta = 1$ is considered to be the group V depletion dose.[27] It is interesting to note that the group V depletion doses are in good agreement with threshold ion doses on a wide variety of III-V compound semiconductor surfaces. Indeed, both the group V depletion doses and the threshold ion doses are inversely dependent on the sputtering yield of each III-V compound. This result suggests a universal mechanism for group III-rich nanostructure formation, based upon ion-induced sputtering.

3.8. Summary and conclusions

In summary, we have examined the formation of ion irradiation-induced nanostructures consisting of Ga droplets on Ga-V surfaces, In islands on In-V surfaces, and Al islands on Al-V surfaces. The group V depletion doses agree well with the threshold ion doses for nucleation of group III-rich droplets or islands. Since the group V depletion dose is inversely proportional to the sputtering yield of each III-V compound, we attribute the nanostructure formation to a mechanism based upon sputtering. This physical mechanism may be used as a guide for nucleation of droplets or islands on a wide variety of compound semiconductor surfaces.

3.9. Figures and references

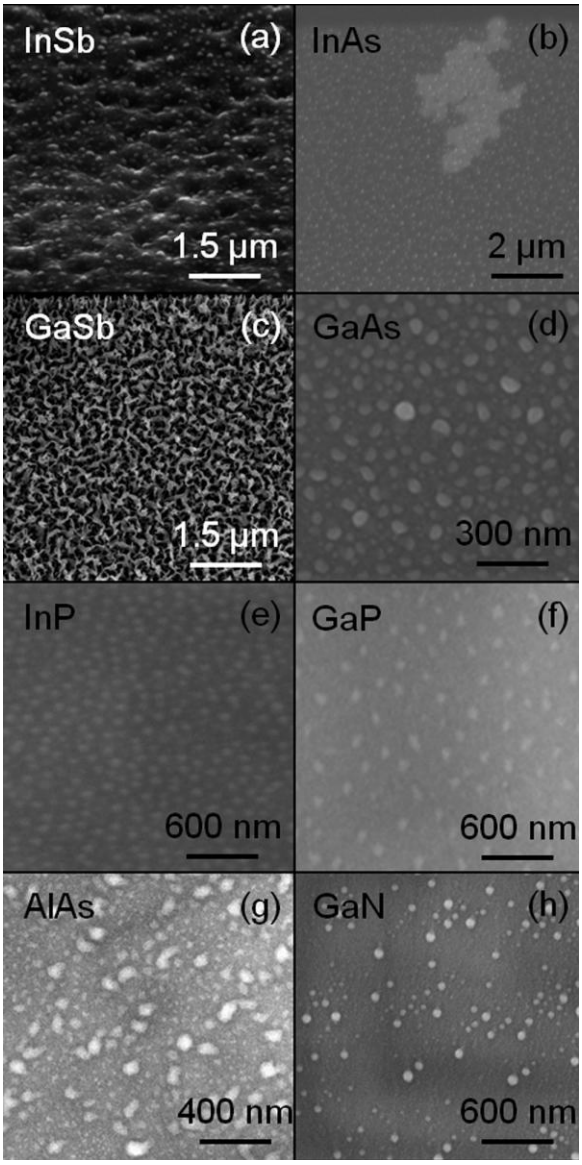

Fig. 3.1. SEM images of ion irradiation-induced nanostructures. Ion irradiation-induced nucleation of group III-rich droplets, islands, or nanorods on III-V compound semiconductor surfaces: (a) In islands on InSb, (b) In islands on InAs, (c) Ga droplets on GaSb, (d) Ga droplets on GaAs, (e) In islands on InP, (f) Ga droplets on GaP, (g) Al islands on AlAs, and (h) Ga droplets on GaN.

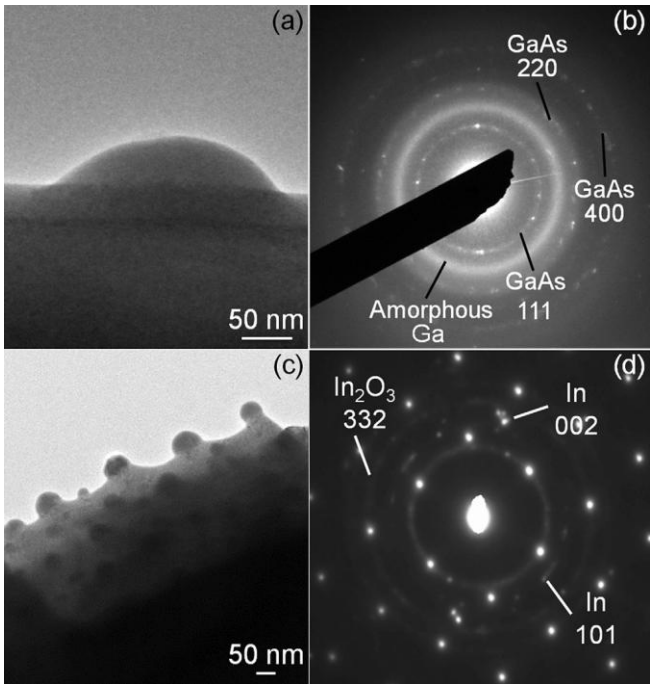

Fig. 3.2. Nanoscale structure of Ga droplets and In islands. (a) Bright-field STEM image and (b) corresponding SAD pattern reveal that Ga droplets consist of amorphous Ga + {111} GaAs with a Ga droplet-GaAs transition layer consisting of ~ 40 nm thick polycrystalline GaAs; (c) bright-field STEM image and (d) corresponding SAD pattern reveal that In islands consist of polycrystalline In_2O_3 and polycrystalline In.

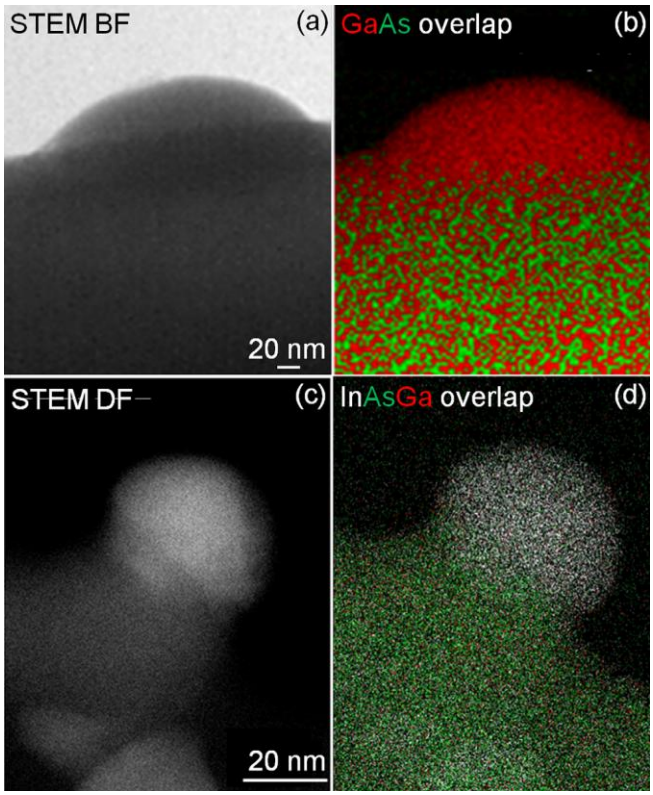

Fig. 3.3. Compositions of Ga droplets and In islands. (a) Bright-field STEM image and (b) An XEDS map reveals a nearly pure Ga droplet on GaAs; (c) dark-field of STEM image and (d) An XEDS map reveals nearly pure In islands on InAs.

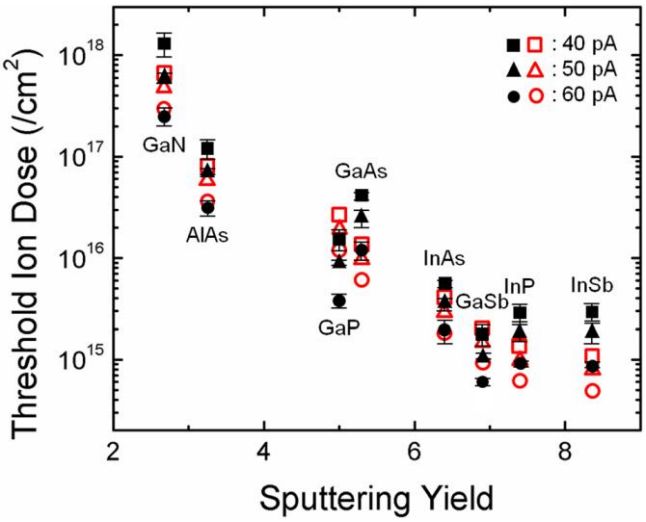

Fig. 3.4. Plots of measured threshold ion doses (black) and computed group V depletion doses (red) for nanostructure formation vs. sputtering yield, Y_{tot} of each III-V compound semiconductor surface. Both measured and computed doses decrease with increasing sputtering yield.

[1]K. Okamoto, I. Niki, A. Shvartser, Y. Narukawa, T. Mukai, and A. Scherer, *Nature Mater.* **3**, 601 (2004).

[2]I. M. Pryce, D. D. Koleske, A. J. Fischer, and H. A. Atwater, *Appl. Phys. Lett.* **96**, 153501 (2010).

[3]S. Gao, N. Koshizaki, H. Tokuhisa, E. Koyama, T. Sasaki, J. K. Kim, J. Ryu, D. S. Kim, and Y. Shimizu, *Adv. Funct. Mater.* **20**, 78 (2010).

[4]A. J. Haes, S. Zou, G. C. Schatz, and R. P. Van Duyne, *J. Phys. Chem. B* **108**, 109 (2004).

[5]S. Xiao, V. P. Drachev, A. V. Kildishev, X. Ni, U. K. Chettiar, H. K. Yuan, and V. M. Shalaev, *Nature* **466**, 735 (2010).

[6]F. Krok, *Vacuum* **83**, 745 (2009).

[7]M. Bouslama, C. Jardin, and M. Ghamnia, *Vacuum* **46**, 143 (1995).

[8]A. Lugstein, M. Weil, B. Basnar, C. Tomastik, and E. Bertagnolli, *Nucl. Instrum. Methods Phys. Res. B* **222**, 91 (2004).

[9]J. L. Plaza and E. Dieguez, *Solid State Ionics* **178**, 1576 (2007).

[10]M. Tanemura, T. Aoyama, A. Otani, M. Ukita, F. Okuyama, and T. K. Chini, *Surf. Sci.* **376**, 163 (1997).

[11]S. K. Tan and A. T. S. Wee, *J. Vac. Sci. Technol. B* **24**, 1444 (2006).

[12]M. Tanemura, S. Aoyama, Y. Fujimoto, and F. Okuyama, *Nucl. Instrum. Methods Phys. Res. B* **61**, 451 (1991).

[13]K. Nozawa, M. Delville, H. Ushiki, P. Panizza, and J. Delville, *Phys. Rev. E* **72**, 011404 (2005).

[14]Q. Wei, J. Lian, W. Lu, and L.Wang, *Phys. Rev. Lett.* **100**, 076103 (2008).

[15]E. Despiau-Pujo and P. Chabert, *J. Vac. Sci. Technol. A* **28**, 1105 (2010).

[16]K. A. Grossklaus and J. M. Millunchick, *J. Appl. Phys.* **109**, 014319 (2011).

[17]Z. L. Liau and J. W. Mayer, *J. Vac. Sci. Technol.* **15**, 1629 (1978).

[18]O. El-Atwani, J. P. Allain, and S. Ortoleva, *Nucl. Instrum. Methods B* **272**, 210 (2012).

[19]U. V. Desnica, J. Wagner, T. E. Haynes, and O. W. Holland, *J. Appl. Phys.* **71**, 2591 (1992).

[20]A. P. Chernyshev, *Mater. Lett.* **63**, 1525 (2009).

[21]R. W. G. Wyckoff, *Crystal Structures* (Interscience, NY, 1963).

[22]C. L. Chen, J.-G. Lee, K. Arakawa, and H. Mori, *Appl. Phys. Lett.* **99**, 013108 (2011).

[23]P. Sigmund, *Phys. Rev.* **184**, 383 (1969).

[24]J. Orloff, M. Utlaut, and L. Swanson, *High Resolution Focused Ion Beams* (Kluwer Academics, NY, 2003).

[25]M. Nastasi, J. W. Mayer, and J. K. Hirvonen, *Ion-Solid Interactions: Fundamentals and Applications* (Cambridge University Press, Cambridge, 1996).

[26]J. Tesmer and M. Nastasi, *Handbook of Modern Ion Beam Materials Analysis* (Materials Research Society, PA, 1995).

[27]See appendix for details of derivations.

Chapter 4

Origins of ion irradiation-induced Ga nanoparticle motion on GaAs surfaces

4.1. Overview

We have examined the origins of ion irradiation-induced nanoparticle (NP) motion. Focused-ion-beam irradiation of GaAs surfaces induces random walks of Ga NPs, which are biased in the direction opposite to that of ion beam scanning. Although the instantaneous NP velocities are constant, the NP drift velocities are dependent on the off-normal irradiation angle, likely due to a difference in surface non-stoichiometry induced by the irradiation angle dependence of the sputtering yield. It is hypothesized that the random walks are initiated by ion irradiation-induced thermal fluctuations, with biasing driven by anisotropic mass transport.

This chapter opens with background information, including a review of various mechanisms proposed to explain origins of NP motion on semiconductor surfaces. Next, the experimental details for the studies of ion-induced Ga NP motion on GaAs surfaces are described. We then discuss the trajectories of ion-induced biased random walks of Ga NP motion. Finally, we consider the instantaneous and drift velocities of the biased random walks in terms of ion-induced thermal fluctuation and anisotropic mass transport, respectively. The chapter concludes with a summary.

4.2. Background

Metallic nanoparticles (NPs) on semiconductor surfaces are promising for a wide range of surface plasmon resonance-enabled applications including enhanced light emission,[1,2] efficient solar energy harvesting,[3] high sensitivity biosensing,[4] and negative refraction.[5] In the case of III-V compound semiconductor surfaces, metallic NPs have been observed following exposure to a Group III molecular beam in the absence of Group V elements, heating in a vacuum, and ion irradiation with either broad area or focused ion beams (FIB).[6-15] During ion irradiation of compound semiconductor surfaces, Ga NP formation and motion are often observed and attributed to ion-induced anisotropic mass transport.[13,16] Similar behavior has been reported on heated GaAs surfaces, in which case Ga NP motion is attributed to a thermal fluctuation-induced gradient in surface tension.[17,18] However, the relative influences of ion-induced anisotropic mass transport and thermal fluctuations on Ga NP motion have not been considered. Here, we present a real-time study of ion irradiation-induced Ga NP motion on GaAs surfaces. FIB irradiation on GaAs surfaces induces biased random walks of Ga NPs. Although the instantaneous NP velocities, v_i, are constant, the NP drift velocities, v_d, increase with the off-normal irradiation angle, θ_{ion}, likely due to a difference in surface non-stoichiometry induced by the θ_{ion}-dependence of the sputtering yield. It is hypothesized that the random and biased walks are initiated by ion-induced thermal fluctuations and ion-induced anisotropic mass transport due to the difference in surface non-stoichiometry, respectively. This mechanism is expected to be applicable to a wide range of compound semiconductor surfaces.

4.3. Experimental procedures

All samples were prepared on semi-insulating GaAs (001) and (111) surfaces using an FEI Nova 200 Nanolab dual beam FIB system. Typical FIB parameters include 30 keV, 0.3 nA current, 12.7 nm pitch, 72.7% beam spot overlap, 0.3 μs dwell time, 2 min total irradiation time, with raster scanning at fast and slow scan rates of 2.5×10^6 μm/min and 4.9×10^3 μm/min, respectively. Assuming that all deposited energy is transformed to heat, these conditions are predicted to lead to a temperature rise, $\Delta T_{FIB} = 1.97\ ^{o}C$.[18,19] For $\theta_{ion} = 0^{o}$, we performed ion beam scanning along both in-plane <110> directions. For the [110] scan direction, we also varied θ_{ion} in 20^{o} increments from 0^{o} to 60^{o}. NP motion was recorded in real-time in the dual-beam FIB, using secondary electrons induced by ion-solid interactions. To quantify the trajectories of Ga NPs, each movie frame was inserted into a code (developed by Jia-Hung Wu in Goldman group and Hsun-Yi Chen in Thornton group) to track the trajectories of NPs via the contrast difference between Ga NPs and GaAs surfaces.[20] For example, Figs. 4.1(a)-4.1(c) show scanning electron micrograph snapshots and corresponding trajectories of the Ga NPs in motion. Initial and final locations of three Ga NPs represented by A, B, and C are marked in Figs. 4.1(a) and 4.1(c), respectively. As shown in Fig. 4.1(b), the Ga NP motion consists of a series of sequential movements in which the direction of each move is randomly determined, i.e., a random walk. Furthermore, the displacement of a Ga NP from its original position is typically in a direction opposite to that of the ion beam slow scan direction, as shown in Fig. 4.2. Therefore, the ion induced Ga NP motion consists of a biased random walk process, which we describe in terms of the average instantaneous velocity, $\langle v_i \rangle$, and the average drift velocity, $\langle v_d \rangle$, as labeled in Fig. 4.1(b).

4.4. Ga nanoparticle velocities

We discuss θ_{ion} dependence of the Ga NP velocities. Figure 4.3 shows plots of $\langle v_i \rangle$ and $\langle v_d \rangle$ vs. θ_{ion}, where closed (opened) symbols denote values of $\langle v_i \rangle$ ($\langle v_d \rangle$), and the dashed line corresponds to calculated values of the average drift velocity, $\langle v_d \rangle_{Comp}$. For both (001) and (111) GaAs surfaces, $\langle v_i \rangle$ is independent of θ_{ion}. Meanwhile, it is interesting to note that $\langle v_d \rangle$ increases with θ_{ion}, also for both (001) and (111) GaAs surfaces. As the Ga^+ ion beam is scanned from region B to region A, a trail of higher non-stoichiometry, δ, defined as $III_{1+\delta}V_{1-\delta}$,[14] is left at the B side of the A/B interface, as shown in Fig. 4.2. Due to the θ_{ion}-dependence of the sputtering yield, a lateral difference in surface nonstoichiometry, $\Delta\delta$, is also dependent on θ_{ion}, as follows:[2,14,21-25]

$$\Delta[\delta(\theta_{ion})] = \Delta\left[\frac{Y_i(\theta_{ion})\frac{Y_P - 1}{Y_P + 1}\frac{dN_{ion}}{dt}t}{\{2N_{III} - Y_i(\theta_{ion})\frac{dN_{ion}}{dt}t\}}\right] \quad (1)$$

where $Y_i(\theta_{ion})$ is the θ_{ion}-dependent total sputtering yield for the ith scan in a continuous raster scan mode;[26] Y_p is the preferential sputtering yield; dN_{ion}/dt is the Ga^+ ion dose rate; t is the dwell time; and N_{III} is the initial number of Group III elements at the beam spot prior to irradiation, respectively.[26] We note that $Y_i(\theta_{ion})$ increases monotonically with θ_{ion}, up to a maximum of 23 at $\theta_{ion} = 65^o$. Furthermore, for our low ion currents, dN_{ion}/dt, and dwell times, t, $2N_{III}$ is orders of magnitude greater than $Y_i(\theta_{ion})[dN_{ion}/dt]t$. Therefore, Eq. (1) is reduced to the following:

$$\Delta[\delta(\theta_{ion})] = \Delta\left[\frac{1}{2N_{III}}Y_i(\theta_{ion})\frac{Y_P - 1}{Y_P + 1}\frac{dN_{ion}}{dt}t\right] \quad (2)$$

Thus, at the A/B interface, $\Delta\delta$ increases with off-normal ion irradiation angle. It is interesting to note that $<v_i>$ is independent of $\Delta\delta$, while $<v_d>$ increases with $\Delta\delta$, as shown in Fig. 4.3.

4.5. Origins of random walks

We discuss the origins of random walks of Ga NP motion. During FIB irradiation, shot noise is expected when the number of ions is small enough to give rise to detectable statistical fluctuations. Therefore, shot noise from the ion beam would decrease with increasing ion dose rate. In our case, $<v_i>$ is independent of ion dose rate over the range 2.0×10^8 /s - 2.0×10^{10} /s. Therefore, it is unlikely that shot noise influences the Ga NP motion. Since $<v_i>$ is independent of θ_{ion}, the random walk is likely driven by ion irradiation-induced thermal fluctuations.[18] At the interface between a Ga NP and GaAs surface, the thermal fluctuation needed to overcome interfacial friction, ΔT_{frict}, is predicted to depend on NP size, ranging from 0.39 to 1.70 ^oC,[18,19] much less than $\Delta T_{FIB} = 1.97\ ^oC$ described above. Since ΔT_{FIB} is greater than ΔT_{frict}, FIB-induced sample heating induces random walks of Ga NPs.

4.6. Origins of biased walks

We now discuss the origins of biased walks of Ga NP motion. At the A/B interface, region B has a higher value of δ than that of region A, as shown in Fig. 4.2, leading to a nonzero value of $\Delta\delta$ at the interface. $\Delta\delta$ induces Ga mass transport from region B toward the Ga NP at the A/B interface.[14,21-25] Thus, excess Ga is built up on the region B side of the Ga NP at the A/B interface, such that the Ga NP expands into region B. At the same time, Ga is sputtered from the

region A side of the Ga NP at the A/B interface. Thus, the Ga NP advances into region B, the direction opposite to that of ion beam scanning. As θ_{ion} is increased, $\Delta\delta$ on each side of the A/B interface increases, inducing higher $\langle v_d \rangle$.[2,21-25] $\langle v_d \rangle$ is expected to be proportional to the mass transport, which in turn is proportional to $\Delta\delta$. Therefore, $\langle v_d(\theta_{ion}) \rangle = A\Delta[\delta_i(\theta_{ion})]$, where A is a constant, and $\langle v_d \rangle_{Comp}$ becomes the following:

$$\langle v_d(\theta_{ion}) \rangle_{Comp} = A\,\Delta\left[\frac{1}{2N_{III}} Y_i(\theta_{ion}) \frac{Y_P - 1}{Y_P + 1} \frac{dN_{ion}}{dt} t\right] \quad (3)$$

In Fig. 4.3, both $\langle v_d \rangle$ and $\langle v_d \rangle_{Comp}$ are plotted as a function of θ_{ion}. Interestingly, both $\langle v_d \rangle$ and $\langle v_d \rangle_{Comp}$ increase monotonically with θ_{ion}. Therefore, it is hypothesized that the random walks are initiated by ion irradiation-induced thermal fluctuations, and the biased walks are driven by an anisotropic mass transport induced by $\Delta\delta$. This mechanism is expected to be applicable to a wide range of compound semiconductor surfaces.

4.7. Summary and conclusions

In summary, we have examined origins of ion irradiation-induced Ga NP motion on GaAs surfaces. FIB irradiation of GaAs surfaces induces random walks of Ga NPs, biased opposite to the ion beam scan direction. v_i is constant, while v_d is linearly dependent on θ_{ion}, due to an enhanced $\Delta\delta$. It is hypothesized that the random walks are initiated by ion irradiation-induced thermal fluctuations, with biasing driven by anisotropic mass transport induced by $\Delta\delta$.

4.8. Figures and references

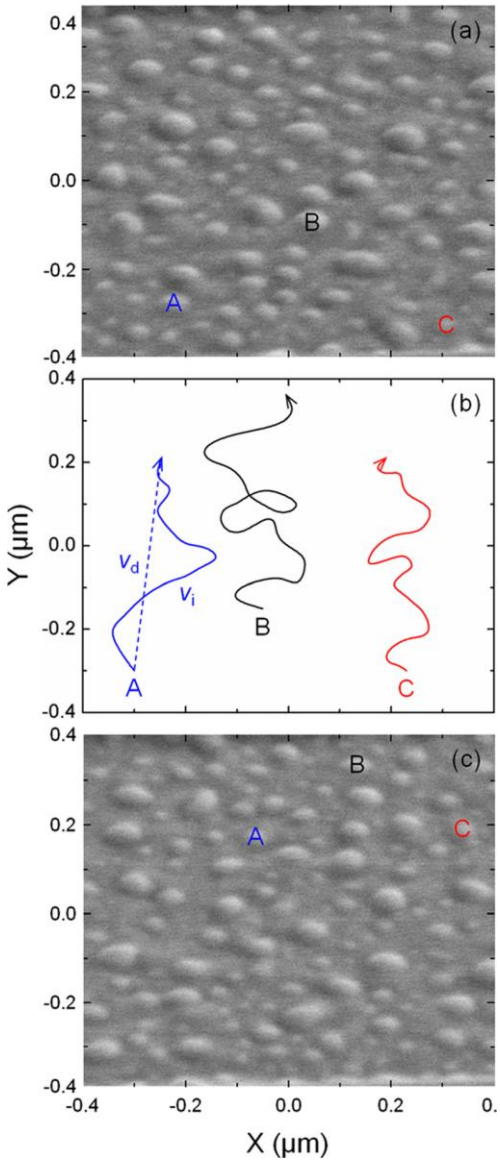

Fig. 4.1. Ion irradiation-induced Ga NP motions with an ion beam scan direction from top to bottom. Scanning electron micrograph snapshots of Ga NPs in motion; (a) initial and (c) final locations of three Ga NPs represented by A, B, and C are marked. (b) Trajectories of Ga NPs in motion showing biased random walks in a direction opposite to that of the ion beam slow scanning.

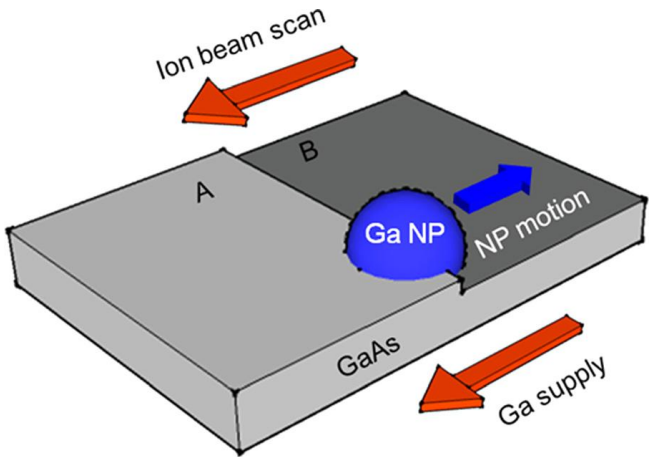

Fig. 4.2. A schematic illustration showing ion irradiation-induced Ga NP motion on a GaAs surface. Scanning of the ion beam from B to A induces Ga mass transport from B to A. The anisotropic Ga mass transport is the driving force for moving Ga NPs from A to B, opposite to the ion beam scan direction.

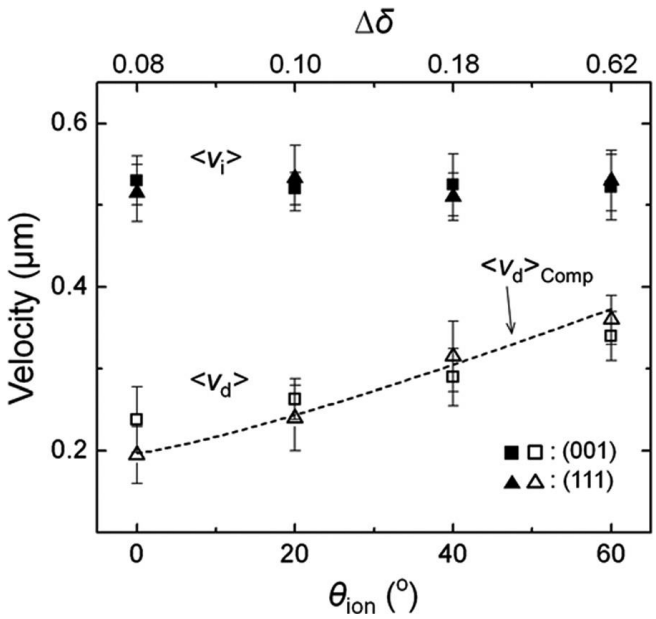

Fig. 4.3. Instantaneous (v_i) and drift velocities (v_d) of Ga NPs on (001) and (111) GaAs surfaces vs. off-normal ion irradiation angle, θ_{eff}, and lateral difference in surface non-stoichiometry, $\Delta\delta$, where closed (opened) symbols represent average instantaneous (drift) velocities, i.e. $\langle v_i \rangle$ ($\langle v_d \rangle$), and the dashed line corresponds to calculated values of the average drift velocity, $\langle v_d \rangle_{Comp}$. On both (001) and (111) GaAs surfaces, $\langle v_i \rangle$ is independent of θ_{ion}, due to ion irradiation-induced thermal fluctuations. Both $\langle v_d \rangle$ and $\langle v_d \rangle_{Comp}$ increase monotonically with θ_{ion}, due to the enhanced $\Delta\delta$.

[1]K. Okamoto, I. Niki, A. Shvartser, Y. Narukawa, T. Mukai, and A. Scherer, *Nature Mater.* **3**, 601 (2004).

[2]M. Kang, A. A. Al-Heji, J. -E. Lee, T. W. Saucer, S. Jeon, J. H. Wu, L. Zhao, A. L. Katzenstein, D. L. Sofferman, V. Sih, and R. S. Goldman, *Appl. Phys. Lett.* **103**, 101903 (2013).

[3]K. Nakayama, K. Tanabe, and H. A. Atwater, *Appl. Phys. Lett.* **93**, 121904 (2008).

[4]A. J. Haes, S. L. Zou, G. C. Schatz, and R. P. Van Duyne, *J. Phys. Chem. B* **108**, 6961 (2004).

[5]C. M. Soukoulis, S. Linden, and M. Wegener, *Science* **315**, 47 (2007).

[6]Q. Wei, J. Lian, S. Zhu, W. Li, K. Sun, and L. Wang, *Chem. Phys. Lett.* **452**, 124 (2008).

[7]M. Bouslama, C. Jardin, and M. Ghamnia, *Vacuum* **46**, 143 (1995).

[8]A. Lugstein, M. Weil, B. Basnar, C. Tomastik, and E. Bertagnolli, *Nucl. Instrum. Methods Phys. Res. B* **222**, 91 (2004).

[9]J. L. Plaza and E. Dieguez, *Solid State Ionics* **178**, 1576 (2007).

[10]M. Tanemura, T. Aoyama, A. Otani, M. Ukita, F. Okuyama, and T. K. Chini, *Surf. Sci.* **376**, 163 (1997).

[11]S. K. Tan and A. T. S. Wee, *J. Vac. Sci. Technol. B* **24**, 1444 (2006).

[12]M. Tanemura, S. Aoyama, Y. Fujimoto, and F. Okuyama, *Nucl. Instrum. Methods Phys. Res. B* **61**, 451 (1991).

[13]J. H. Wu, W. Ye, B. L. Cardozo, D. Saltzman, K. Sun, H. Sun, J. F. Mansfield, and R. S. Goldman, *Appl. Phys. Lett.* **95**, 153107 (2009).

[14]M. Kang, J. H. Wu, S. Huang, M. V. Warren, Y. Jiang, E. A. Robb, and R. S. Goldman, *Appl. Phys. Lett.* **101**, 082101 (2012).

[15]M. Kang, T. W. Saucer, M. V. Warren, J. H. Wu, H. Sun, V. Sih, and R. S. Goldman, *Appl. Phys. Lett.* **101**, 081905 (2012).

[16]S. Lee, L. Wang, and W. Lu, *Surf. Sci.* **606**, 659 (2012).

[17]J. Tersoff, D. E. Jesson, and W. X. Wang, *Science* **324**, 236 (2009).

[18]T. Ishitani and H. Kaga, *J. Electron. Microsc.* **44**, 331 (1995).

[19]For ΔT_{FIB} and ΔT_{frict}, parameters for GaAs include thermal conductivity (55 W/mK) and thermal coefficient of surface tension (-0.66 Kg/s^{2o}C).

[20]J. H. Wu, Ph.D. thesis, University of Michigan, 2013.

[21]Q. Wei, J. Lian, W. Lu, and L. Wang, *Phys. Rev. Lett.* **100**, 076103 (2008).

[22]P. Sigmund, *Phys. Rev.* **184**, 383 (1969).

[23]J. Orloff, M. Utlaut, and L. Swanson, *High Resolution Focused Ion Beams* (Kluwer Academics, New York, 2003).

[24]M. Nastasi, J. W. Mayer, and J. K. Hirvonen, *Ion-Solid Interactions: Fundamentals and Applications* (Cambridge University Press, Cambridge, 1996).

[25]J. Tesmer and M. Nastasi, *Handbook of Modern Ion Beam Materials Analysis* (Materials Research Society, Pennsylvania, 1995).

[26]$Y_i(\theta_{ion}) = Y_{0i}\cos\theta_{ion}\exp[(a^2\sin^2\theta_{ion})/2b^2]$; $Y_0 = 5.17$; $Y_p = 1.9$; $\theta_{ion} = 0 - 60^o$; $a = 40$ nm; $b = 17$ nm; $dN_{ion}/dt = 1.88 \times 10^9$ /s; $t = 0.3$ μs; $N_{III} = 1.58 \times 10^5$, respectively.

Chapter 5

Surface plasmon resonances of Ga nanoparticle arrays

5.1. Overview

We have examined the influence of particle and chain diameter on surface plasmon resonance (SPR) energy of 2D and 1D Ga nanoparticle (NP) arrays fabricated using focused-ion-beam irradiation of GaN surfaces. Maxima in the extinction spectra suggest the presence of SPR at visible and near-infrared wavelengths. The SPR energies increase with decreasing NP or chain diameter, due to particle diameter-dependent dipole interactions within the metallic NPs. The SPR quality (Q) factors are comparable to those reported from Ag and Au NPs, suggesting Ga NPs as a promising alternative plasmonic material.

This chapter opens with background information, including a review of SPR of metallic NPs. Next, the experimental details for the studies of SPR of ion-induced Ga NP arrays on GaN surfaces are described. We then discuss the morphology, structure, and composition of ion-induced Ga NP arrays. Finally, we consider the influence of dimensions of Ga NP arrays on SPR energies along with Q factors. The chapter concludes with a summary.

5.2. Background

It has been shown that metallic nanoparticles (NPs) enable the generation of surface plasmon resonances (SPR) in the ultraviolet, visible, and infrared ranges.[1-6] Recently, metallic NPs on semiconductor surfaces have shown significant promise for various applications including enhanced light emission, efficient solar energy harvesting, high sensitivity biosensing, and negative refractive index metamaterials.[7,8] To date, plasmonics research has focused nearly exclusively on Ag and Au NPs.[9-11] Although Ag and Au are widely available, their optical response is limited to low SPR energies (<3.5 eV). On the other hand, SPR in the range 0.8 to 5.8 eV were recently reported for Ga NP ensembles with average NP diameters ranging from 10 to 300 nm.[1] However, the reports to date have been limited to randomly-distributed and close-packed NP ensembles, for which the relative roles of the particle diameter-dependent dipole interactions NPs and the interparticle spacing-dependent dipole interactions between NPs cannot be isolated. Thus, the Ga NP SPR quality (Q) factor remains unknown. The suppression of dipole coupling between NPs has been reported for ratios of the NP spacing to diameter greater than 2.5.[12,13] Using normal-incidence Ga^+ focused ion beam (FIB) irradiation[14-21] of GaN surfaces, we have fabricated Ga NP ensembles with a range of spacings and diameters, all of which satisfy the condition for suppressed dipole coupling discussed above. We report on the influence of the NP diameter on the SPR energy and Q factor for both 2D and 1D NP arrays. We find SPR energies ranging from 1.6 eV to 2.2 eV with Q factors ranging from 1.9 to 3.5, comparable to those reported for Ag and Au NPs.[9-11]

5.3. Experimental procedure

Size and site-controlled arrays of Ga NPs were seeded by Ga^+ FIB irradiation of the surfaces of 5 μm thick GaN layers grown on sapphire.[22] For the nanofabrication process, arrays of holes of various depths were fabricated using FIB with 30 keV voltage, 50 pA current, 7.1 nm pitch (distance between beam spots), and 100 ns dwell time. We note that the holes have sloped sidewalls, presumably due to preferential redeposition at the sidewalls.[23,24] Subsequently, a Ga^+ ion beam with the same voltage, current, pitch, and 0.1 ms dwell time was scanned over the entire region including pre-patterned holes, leading to the formation of Ga NPs within the holes. Following fabrication, the lateral dimensions and arrangements of the NP arrays were quantified using SEM, and the nanostructure phase was identified using transmission electron microscopy (TEM).[25] For transmission electron microscopy (TEM) studies, cross-sectional specimens of Ga nanoparticle (NP) arrays on GaN surfaces were prepared by ion milling followed by lift-out processing in a FEI Helios Nanolab 650 FIB (conducted by Haiping Sun at Electron Microscopy Analysis Laboratory). The sample was then mounted on a Mo grid and ion polished to ~ 100 nm. TEM imaging and selected area diffraction (SAD) were carried out in a JEOL 3011 operating at 300 kV by Michael V. Warren in Goldman group. For the 2D arrays, particle diameters (d_{Ga}) ranged from 120 to 200 nm and interparticle spacings ($d_{Ga\text{-}Ga}$) ranged from 400 to 800 nm. The 1D chain diameters (d_{chain}) and interchain spacing ($d_{chain\text{-}chain}$) ranged from 80 to 200 nm and 400 to 600 nm, respectively. The diameters and spacings for all samples were controlled via the hole diameters (d_{hole}) and interhole spacings ($d_{hole\text{-}hole}$) of the first FIB irradiation step. In addition, a transition from 2D to 1D arrays was achieved for hole depths (Z_{hole}) greater than 50 nm. Spatially-resolved absorption measurements in the wavelength range 400 nm to 1100 nm were

performed using a tungsten halogen lamp and a 0.7 NA objective, in a confocal microscope configuration by Timothy W. Saucer in Sih group.[26] Although the wavelength of the incident radiation is comparable to $d_{Ga\text{-}Ga}$ and $d_{chain\text{-}chain}$, we will show that any Bragg scattering effects can be ruled out. Using a liquid nitrogen cooled CCD detector and 0.75 m spectrometer, room temperature transmittance (*T*) and reflectance (*R*) spectra were collected from both the patterned and unpatterned regions of the surface. *T* and *R* from the patterned area were then obtained by subtracting the background spectra from the unpatterned area. Finally, maxima in the extinction spectra, $E = \log_{10}[(1 - R)/T]$ were attributed to surface plasmon resonances.

5.4. Morphology of Ga NP arrays

We discuss the influence of $d_{hole\text{-}hole}$, d_{hole}, and Z_{hole} on the array formation. As shown in Figs. 5.1(a)-5.1(c), $d_{hole\text{-}hole}$ of 800 nm, 600 nm, and 400 nm lead to the formation of Ga NPs with $d_{Ga\text{-}Ga} = d_{hole\text{-}hole}$. For d_{hole} ranging from 250 nm to 200 nm to 150 nm, the formation of NPs with average $d_{Ga} = 200 \pm 6$ nm, 160 ± 6 nm, and 120 ± 4 nm are observed, as shown in Figs. 5.1(a)-5.1(c). For the 2D square arrays in Figs. 5.1(a)-5.1(c), within the pre-patterned holes, large NPs are observed near the hole center with small NPs at the periphery. Due to the sloped sidewall of the pre-patterned holes, irradiation at the periphery is effectively off-normal, and therefore a higher sputtering yield is expected.[27] Since the growth of Ga NPs depends on the competition between the sputtering and migration of Ga atoms, the higher sputtering yield leads to the formation of smaller NPs at the hole periphery.[28] Furthermore, as shown in Figs. 5.1(c)-5.1(e), as Z_{hole} increases from 10 nm to 100 nm, the nucleation of small NPs occurs at the expense of the large NPs, eventually leading to 1D arrays of smaller, close-packed NPs. A comparison of 1D

arrays in Fig. 5.1(e) and 5.1(f) reveals that 600 nm and 400 nm-sized $d_{hole\text{-}hole}$ lead to the formation of Ga NPs with $d_{chain\text{-}chain} = d_{hole\text{-}hole}$, and 250 nm- and 150 nm-sized d_{hole} lead to the formation of NPs with $d_{chain} = 200 \pm 6$ nm and 80 ± 6 nm. The size distributions for 2D and 1D NP arrays are shown in Fig. 5.2; fits to a log-normal distribution yield average diameters ranging from 200 ± 6 nm to 160 ± 6 nm to 120 ± 4 nm, corresponding to Figs. 5.1(a)-5.1(c), and from 80 ± 6 nm to 200 ± 6 nm, corresponding to Figs. 5.1(e) and 5.1(f). These results demonstrate that $d_{hole\text{-}hole}$, d_{hole}, and Z_{hole} determine $d_{Ga\text{-}Ga}$ ($d_{chain\text{-}chain}$), d_{Ga} (d_{chain}), and the array distribution, respectively.

5.5. Structure and composition of Ga nanoparticle arrays

Figure 5.3 presents (a) a bright-field TEM image and corresponding selected area diffraction (SAD) patterns collected from (b) a FIB-patterned Ga NP and (c) the GaN substrate, in the vicinity of the Ga NP. The SAD pattern from the Ga NP, shown in Fig. 5.3(b), presents a diffuse ring corresponding to a mean interatomic distance of 2.79 Å, similar to the first nearest neighbor Ga separation reported for α-Ga, 2.78 Å.[29] For the GaN region, Fig. 5.3(c) reveals a single crystal pattern with $R_1/R_2 = 1.778$ and $\theta_{R1\text{-}R2} = 90°$, similar to the $[\bar{1}100]$ zone axis of a-plane wurtzite GaN, with $R_{(11\bar{2}0)}/R_{(0001)} = 1.779$ and $\theta_{(11\bar{2}0)\text{-}(0001)} = 90°$.[30]

5.6. Extinction spectra of Ga nanoparticle arrays

We now discuss the influence of d_{Ga} and d_{chain} on the SPR energy. Figure 5.4(a) contains a plot of extinction spectra vs. energy for 2D square arrays of Ga NPs, including small $d_{Ga} = 120 \pm$

4 nm (with d_{Ga-Ga} = 400 nm), intermediate d_{Ga} = 160 ± 6 nm (with d_{Ga-Ga} = 600 nm), and large d_{Ga} = 200 ± 6 nm (with d_{Ga-Ga} = 800 nm). The observed maxima in the extinction spectra suggest the presence of SPR at 2.2 eV, 1.9 eV, and 1.6 eV for the small, intermediate, and large d_{Ga}, respectively. Similarly, Fig. 5.4(b) contains a plot of extinction vs. energy for 1D chain arrays of Ga NPs, including small d_{chain} = 80 ± 6 nm (with $d_{chain-chain}$ = 400 nm) and large d_{chain} = 200 ± 6nm (with $d_{chain-chain}$ = 600 nm). The observed maxima in the extinction spectra suggest the presence of SPR at 2.2 eV and 1.9 eV for the small and large d_{chain}, respectively. The high frequency oscillations are related to spectral interferences between the GaN surface and the GaN/Al_2O_3 interface.[31] To consider possible dipole interactions between NPs, we examine the influence of d_{Ga-Ga} on the SPR energy from 2D square arrays with d_{Ga} value of 120 ± 4 nm and d_{Ga-Ga} values of 400 nm, 600 nm, and 800 nm. As shown in Fig. 5.4(c), a plot of extinction spectra vs. energy for these arrays demonstrates that the resonances are located at the same energy, independent of d_{Ga-Ga}. Thus, d_{Ga-Ga} ($d_{chain-chain}$) in the range 400nm to 800nm are sufficient to prevent interactions via dipolar coupling and isolate the influence of d_{Ga} (d_{chain}) on the SPR energy.

5.7. Surface plasmon resonance energy of Ga nanoparticle arrays

Figure 5.5 shows a plot of SPR energy vs. d_{Ga} (d_{chain}) for 2D square (1D chain) arrays. As d_{Ga} (d_{chain}) decreases, the resonances shift to higher energy (shorter wavelength), ranging from near-infrared to visible wavelengths. These resonances may be due to particle diameter-dependent dipole oscillations. For metallic NPs, the energy of the dipole resonance increases with decreasing NP size.[32] Intuitively, this can be understood by recognizing that the distance

between the charges at opposite surfaces of the particle decreases with particle size, thus leading to a larger restoring force and, therefore, a higher resonance frequency. Although the SPR wavelengths are similar for similar $d_{Ga\text{-}Ga}$ and $d_{chain\text{-}chain}$, Fig. 5.4(c) shows wavelength-independent SPR for arrays with various $d_{Ga\text{-}Ga}$, suggesting that SPRs occur via dipole interactions within NPs rather than Bragg scattering.

5.8. Quality factor of surface plasmon resonances

The quality factor of an SPR is defined as $Q_{SPR} = f_r/\Delta f_i$, where f_r is the resonance frequency and Δf_i is the broadening of the resonance induced by intrinsic losses.[33] The total broadening includes contributions from Δf_i and the NP size distribution, Δf_{size}, as follows: $\Delta f_{total}^{0.5} = \Delta f_i^{0.5} + \Delta f_{size}^{0.5}$. Polynomial fits to the extinction data were used to determine Δf_{total}. Using a linear fit to the SPR data and the average standard deviations of the log normal fit to the NP size distributions, we extracted Δf_{size}. As shown in Fig. 5, the values of Q_{SPR} range from 1.9 to 3.5. We note that these values are comparable to literature reports of Au and Ag NPs, which range from 1.0 to 14.8,[9-11,34,35] suggesting that Ga NPs can be an alternative plasmonic material.

5.9. Summary and conclusions

We have demonstrated FIB-induced 2D square and 1D chain arrays of Ga NPs via pre-patterned holes on GaN surfaces where $d_{hole\text{-}hole}$, d_{hole}, and Z_{hole} determine $d_{Ga\text{-}Ga}$ ($d_{chain\text{-}chain}$), d_{Ga} (d_{chain}), and the array distribution, respectively. Extinction spectra of 2D square and 1D chain arrays reveal SPR energies in the visible and near-IR ranges. Interestingly, the SPR energies are

blue-shifted with decreasing NP or chain diameter, due to particle diameter-dependent dipole interactions within the metallic NPs. This approach provides an opportunity to tune SPR over a wide energy range, with Q_{SPR} values comparable to those reported for Ag and Au NPs.

5.10. Figures and references

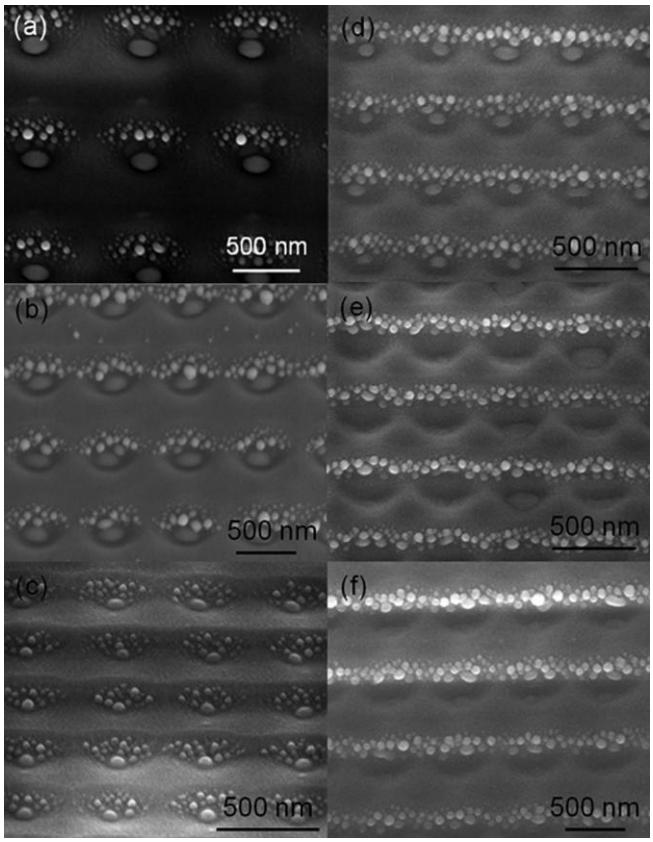

Fig. 5.1. SEM images of FIB-fabricated 2D square and 1D chain arrays of Ga NPs on GaN surfaces, showing the influence of $d_{hole-hole}$, d_{hole}, and Z_{hole} on d_{Ga-Ga} ($d_{chain-chain}$), d_{Ga} (d_{chain}), and the NP distribution; (a) d_{hole} = 250nm (with $d_{hole-hole}$ = 800nm and Z_{hole} = 10 nm), (b) d_{hole} = 200 nm (with $d_{hole-hole}$ = 600 nm and Z_{hole} = 10 nm), (c) d_{hole} = 150 nm (with $d_{hole-hole}$ = 400 nm and Z_{hole} = 10 nm), (d) Z_{hole} = 50 nm (with d_{hole} = 150 nm and $d_{hole-hole}$ = 400 nm), (e) Z_{hole} = 100 nm (with d_{hole} = 150 nm and $d_{hole-hole}$ = 400 nm), and (f) Z_{hole} = 100 nm (with d_{hole} = 250 nm and $d_{hole-hole}$ = 600 nm).

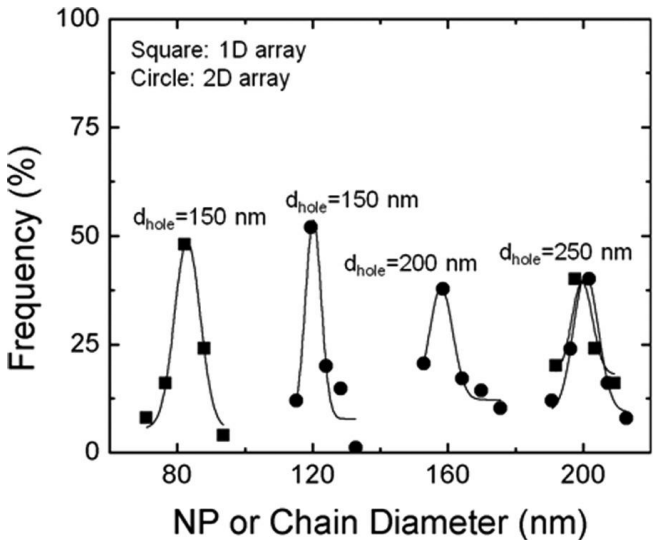

Fig. 5.2. Size distributions for 2D square and 1D chain arrays shown in Figs. 5.1(a)-5.1(f); The frequency is the percentage of NPs with diameters within a specified range. Fits to a log-normal distribution are shown as lines with average diameters (and R^2 values) ranging from d_{Ga} = 200 ± 6 nm in 250 nm-sized hole (0.95) to d_{Ga} = 160 ± 6 nm in 200 nm-sized hole (0.91) to d_{Ga} = 120 ± 4 nm in 150 nm-sized hole (0.87) for 2D square arrays, and from d_{chain} = 80 ± 6 nm in 150 nm-sized hole (0.96) to d_{chain} = 200 ± 6nm in 250 nm-sized hole (0.94) for 1D chain arrays.

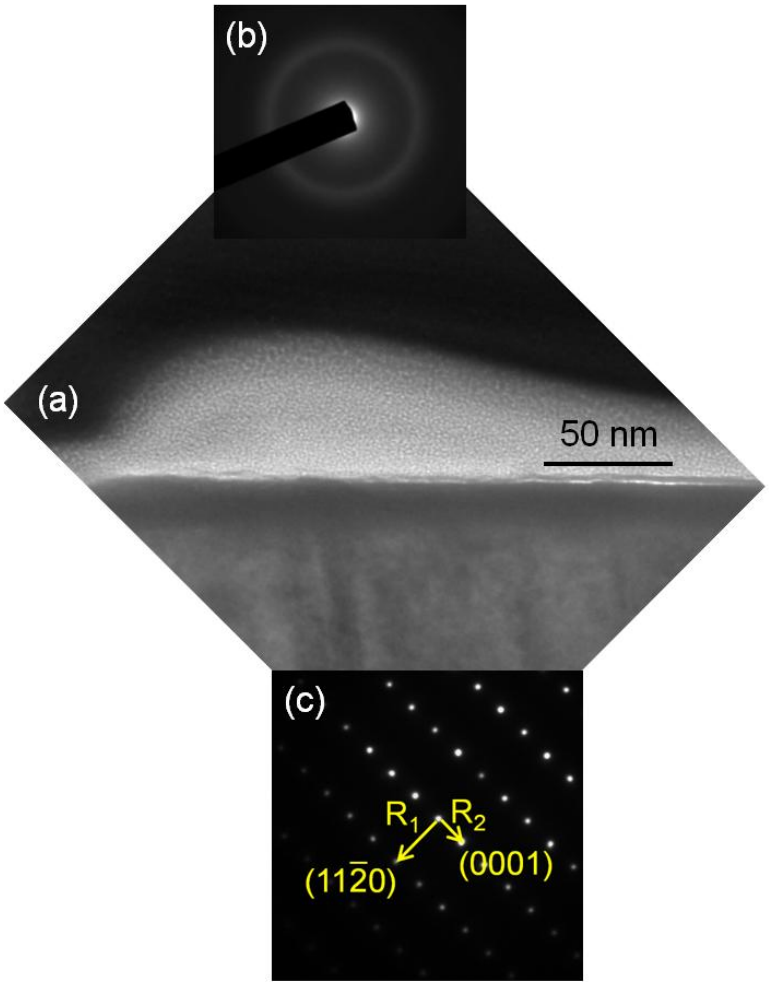

Fig. 5.3. (a) Bright-field transmission electron micrograph of a FIB-fabricated Ga nanoparticle (NP) on a GaN surface; corresponding SAD pattern collected from (b) a Ga NP and (c) the GaN substrate, in the vicinity of the Ga NP.

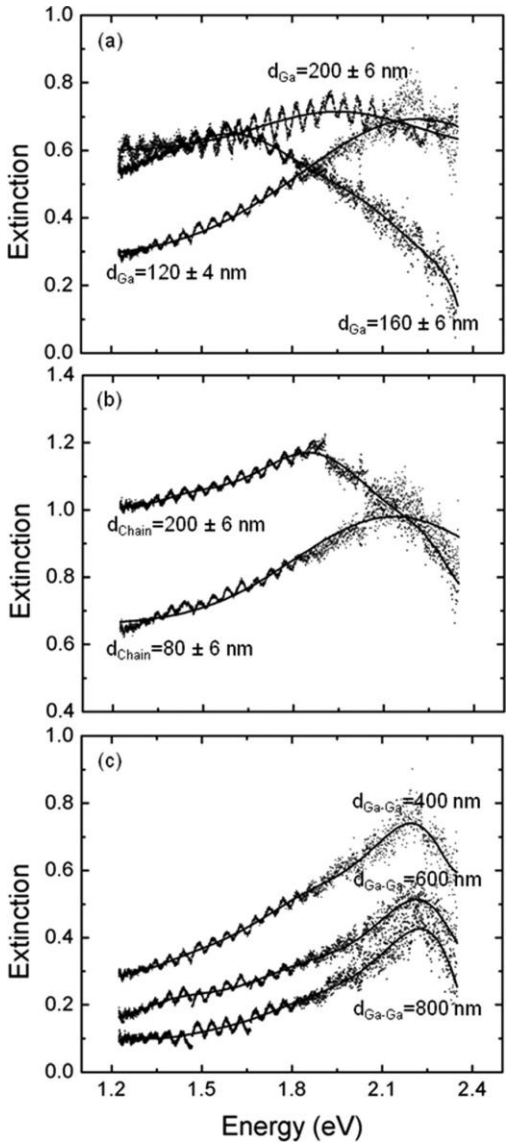

Fig. 5.4. Extinction spectra of 2D square and 1D chain arrays of Ga NPs on GaN surfaces. Fits to polynomial distributions are shown as lines, and corresponding R^2 values range from 0.93 to 0.98. Extinction spectra of (a) 2D square arrays with d_{Ga} = 120 ± 4 nm, 160 ± 6 nm, and 200 ± 6 nm, corresponding to SPR energy at 2.2 eV, 1.9 eV, and 1.6 eV, respectively, (b) 1D chain arrays with d_{chain} = 80 ± 6 nm and 200 ± 6 nm, corresponding to SPR energy at 2.2 eV and 1.9 eV, respectively. (c) 2D square arrays with d_{Ga-Ga} = 400, 600, and 800 nm, corresponding to the same SPR energy at 2.2 eV.

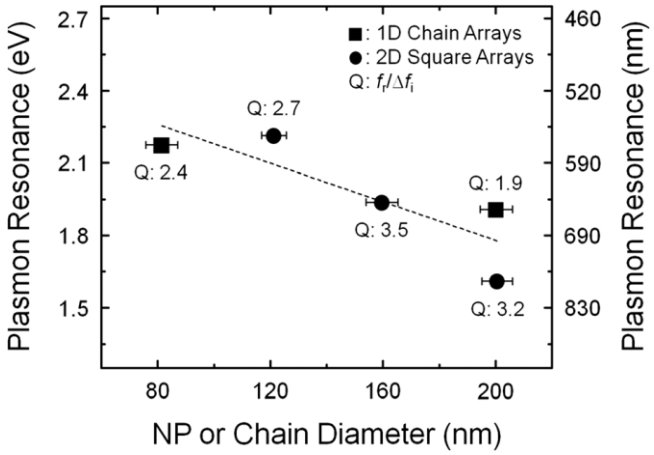

Fig. 5.5. A plot of SPR energy (wavelength) vs. NP or chain diameter. The horizontal error bars correspond to standard deviations of size distributions in Fig. 5.2. The resonance energy (wavelength) increases (decreases) from near-IR to visible ranges with decreasing NP or chain diameter. The values of Q_{SPR} range from 1.9 to 3.5, comparable to the reported values for Ag and Au NPs. A fit to the SPR energies is shown as the dashed line, with $\chi = 0.91$.

[1]P. Wu, T. Kim, A. Brown, M. Losurdo, G. Bruno, and H. Everitt, *Appl. Phys. Lett.* **90**, 103119 (2007).

[2]A. Derkachova and K. Kolwas, *Eur. Phys. J. Spec. Top.* **144**, 93 (2007).

[3]B. N. Khlebtsov and N. G. Khlebtsov, *J. Phys. Chem. C* **111**, 11516 (2007).

[4]A. Liebsch, *Phys. Rev. B* **48**, 11317 (1993).

[5]K. Kolwas, A. Derkachova, and M. Shopa, *J. Quant. Spectrosc. Radiat. Transf.* **110**, 1490 (2009).

[6]Z. L. Wang and J. M. Cowley, *Ultramicroscopy* **23**, 97 (1987).

[7]J. A. Schuller, E. S. Barnard, W. Cai, Y. C. Jun, J. S. White, and M. L. Brongersma, *Nature Mater.* **9**, 193 (2010).

[8]A. Polman, *Science* **322**, 868 (2008).

[9]T. R. Jensen, M. D. Malinsky, C. L. Haynes, and R. P. V. Duyne, *J. Phys. Chem. B* **104**, 10549 (2000).

[10]S. J. Oldenburg, J. B. Jackson, S. L. Westcott, and N. J. Halas, *Appl. Phys. Lett.* **75**, 2897 (1999).

[11]S. J. Oldenburg, R. D. Averitt, S. L. Westcott, and N. J. Halas, *Chem. Phys. Lett.* **288**, 243 (1998).

[12]K. H. Su, Q. H. Wei, X. Zhang, J. J. Mock, D. R. Smith, and S. Schultz, *Nano Lett.* **3**, 1087 (2003).

[13]L. Gunnarsson, T. Rindzevicius, J. Prikulis, B. Kasemo, M. Kall, S. Zou, and G. C. Schatz, *J. Phys. Chem. B* **109**, 1079 (2005).

[14]M. Bouslama, C. Jardin, and M. Ghamnia, *Vacuum* **46**, 143 (1995).

[15]A. Lugstein, M. Weil, B. Basnar, C. Tomastik, and E. Bertagnolli, *Nucl. Instrum. Methods Phys. Res. B* **222**, 91 (2004).

[16]J. L. Plaza and E. Dieguez, *Solid State Ionics* **178**, 1576 (2007).

[17]M. Tanemura, T. Aoyama, A. Otani, M. Ukita, F. Okuyama, and T. K. Chini, *Surf. Sci.* **376**, 163 (1997).

[18]S. K. Tan and A. T. S. Wee, *J. Vac. Sci. Technol. B* **24**, 1444 (2006).

[19]M. Tanemura, S. Aoyama, Y. Fujimoto, and F. Okuyama, *Nucl. Instrum. Methods Phys. Res. B* **61**, 451 (1991).

[20]J. H. Wu, W. Ye, B. L. Cardozo, D. Saltzman, K. Sun, H. Sun, J. F. Mansfield, and R. S. Goldman, *Appl. Phys. Lett.* **95**, 153107 (2009).

[21]M. Kang, J. H. Wu, S. Huang, M. V. Warren, Y. Jiang, E. A. Robb, and R. S. Goldman, *Appl. Phys. Lett.* **101**, 082101 (2012).

[22]The room temperature bandgap energy of GaN is 3.45 eV.

[23]A. A. Tseng, *J. Micromech. Microeng.* **14**, R15 (2004).

[24]A. J. Steckl and I. Chyr, *J. Vac. Sci. Technol. B* **17**, 362 (1999).

[25]See appendix for details of TEM studies.

[26]T. W. Saucer, J.-E. Lee, A. J. Martin, D. Tien, J. M. Millunchick, and V. Sih, *Solid State Commun.* **151**, 269 (2011).

[27]P. Sigmund, *Phys. Rev.* **184**, 383 (1969).

[28]Q. Wei, J. Lian, W. Lu, and L. Wang, *Phys. Rev. Lett.* **100**, 076103 (2008).

[29]A. Bererhi, L. Bosio, and R. Cortes, *J. Non-Crystalline Solids* **30**, 253 (1979).

[30]C. H. Shih, T. H. Huang, R. Schuber, Y. L. Chen, L. Chang, I. Lo, M. M. Chou, and D. M. Schaadt, *Nanoscale Res. Lett.* **6**, 425 (2011).

[31]G. Tittelbach, B. Richter, and W. Karthe, *Pure Appl. Opt.* **2**, 683 (1993).

[32]S. A. Maier, *Plasmonics: Fundamentals and Applications* (Springer, New York, 2007).

[33]we note that the quality factor used in a wide range of fields is different from the figure of merit defined as $-\varepsilon_{real}/\varepsilon_{imaginary}$ where ε_{real} ($\varepsilon_{imaginary}$) is the real (imaginery) dielectric constant of the metallic NPs.

[34]P. M. Jais, D. B. Murray, R. Merlin, and A. V. Bragas, *Nano Lett.* **11**, 3685 (2011).

[35]M. A. Noginov, G. Zhu, A. M. Belgrave, R. Bakker, V. M. Shalaev, E. E. Narimanov, S. Stout, E. Hertz, T. Suteewong, and U. Wiesner, *Nature* **460**, 1110 (2009).

Chapter 6

Ga Nanoparticle-Enhanced Photoluminescence of GaAs

6.1. Overview

We have examined the influence of surface Ga nanoparticles (NPs) on the enhancement of GaAs photoluminescence (PL) efficiency. We have utilized off-normal focused-ion-beam irradiation of GaAs surfaces to fabricate close-packed Ga NP arrays. The enhancement in PL efficiency is inversely proportional to the Ga NP diameter. The maximum PL enhancement occurs for the Ga NP diameter predicted to maximize the incident electromagnetic (EM) field. The PL enhancement is driven by the surface plasmon resonance (SPR)-induced enhancement of the incident EM field which overwhelms the SPR-induced suppression of the light emission.

This chapter opens with background information, including a review of various mechanisms proposed to explain origins of NP motion on semiconductor surfaces. Next, the experimental details are given for the studies of Ga NP-enhanced PL efficiency of GaAs. We then compute the Ga NP diameter dependence of SPR-induced incident EM field enhancement and suppression of the light emission. Finally, we present experimental Ga NP diameter-dependent GaAs PL enhancements where the mechanism for the PL enhancement is discussed, based on the prediction from our computations. The chapter concludes with a summary.

6.2. Background

When electromagnetic (EM) radiation is incident upon metallic nanoparticles (NPs), a collective oscillation, termed a surface plasmon resonance (SPR), is generated. Recently, metallic NPs on semiconductor surfaces have shown significant promise for various applications including enhanced light emission,[1] efficient solar energy harvesting,[2] high sensitivity biosensing,[3] and negative refractive index metamaterials.[4] For example, metallic NP-induced photoluminescence (PL) enhancement has been demonstrated and attributed to the matching of the NP SPR energy with the spectral range of the semiconductor light emission energy.[1,5-7] To date, plasmonics research has focused nearly exclusively on Ag and Au NPs; however, their optical response is limited to low SPR energies (<3.5eV).[1,8] It was recently shown that Ga NPs produce size-dependent SPR, ranging from near-infrared to visible wavelengths.[9,10] Furthermore, 2D and 1D Ga NP arrays with SPR quality factors comparable to those from Ag and Au were reported.[9] However, the influence of Ga NPs, including the role of the Ga NP diameter (d_{Ga}) on GaAs PL emission has not been examined. Here, we use a combination of experiments and computations to determine the influence of d_{Ga} on the enhancement of GaAs donor-acceptor pair (DAP) emission, revealing a physical mechanism based upon the SPR-induced enhancement of the incident EM field which overwhelms the SPR-induced suppression of the light emission.

6.3. Experimental procedure

Close-packed arrays of Ga NP were fabricated on GaAs surfaces using off-normal Ga^+ FIB irradiation with 5 keV voltage, 0.23 nA current, 6.1 nm pitch, 50 ns dwell time, and off-

normal ion irradiation angles (θ_{ion}) ranging from 26° to 82°. Off-normal focused-ion-beam irradiation on GaAs surfaces leads to the preferential sputtering of As atoms, leading to a Ga-rich GaAs surface. Beyond a threshold ion dose, metallic NP consisting primarily of Ga are nucleated. Following fabrication, SEM imaging was used to quantify the NP dimensions and NP array configurations. Spatially-resolved PL measurements were performed on the samples mounted in a helium flow cryostat operating at 10K, using a 633 nm CW Helium-Neon laser by Ji-Eun Lee in Sih group. Pump powers varied from 0.04 to 4.34 mW, as measured before a 0.7 NA infinity corrected objective. The diameter of the normally-incident focused laser on the sample was 5 μm, and a confocal microscope configuration was used to collect the emission from a 3 μm diameter spot within only the FIB-patterned regions. PL was recorded using a 150 G/mm reflection grating in a 0.75 m spectrometer and a liquid nitrogen cooled Si CCD detector.[11] To take into account the Ga NP size dependence of the pump laser absorption and DAP emission, for each sample, the PL spectrum was normalized by the integrated intensity of the absorbed laser light, defined as the difference between the laser spectrum and laser-induced surface reflectivity. PL enhancement ratios were then defined as the ratio of the normalized PL intensities for regions of the GaAs layer with and without Ga NPs. We also note that we will show any Bragg scattering effects can be ruled out.

6.4. Morphology of Ga nanoparticle arrays

We discuss the influences of θ_{ion} on d_{Ga} and the density (n_{Ga}) of Ga NP arrays. Figures 6.1(a)-(d) present representative SEM images of close-packed Ga NP arrays on GaAs surfaces irradiated at various θ_{ion} values. In each image, bright features correspond to Ga NPs. A

combination of bright-field STEM, EDAX, and SAD data reveals nearly hemispheroidal amorphous Ga-rich NPs, without evidence of any oxide, at the surface of the irradiated GaAs.[12] Since the melting temperature of Ga is below 300 K, the Ga NPs might be liquid or a core/shell of liquid/solid.[12] Fits to log-normal distributions yield average d_{Ga} ranging from 69.1 ± 2.9 nm to 33.3 ± 1.3 nm, and n_{Ga} ranging from 6.1×10^9 /cm^2 to 2.7×10^{10} /cm^2. These show wider ranges of d_{Ga} and n_{Ga}, compared with reported values.[13] In Fig. 6.1(e), d_{Ga} (left) and n_{Ga} (right) are plotted as a function of θ_{ion}. It is interesting to note that n_{Ga} (d_{Ga}) is proportional (inversely proportional) to θ_{ion}, and the fractional surface coverages of Ga NPs is 23 ± 0.3 %. Irradiation-induced surface Ga NP formation results from the competition between sputtering and migration of Ga atoms.[9,13] Typically, d_{Ga} is minimized as the contribution of sputtering is increased. We note that a Ga-rich (non-stoichiometric) transition layer has been reported.[9,12,14] The irradiation-induced damage within the transition layer is proportional to θ_{ion},[15] while the thickness of the transition layer ranges from 6 nm to 1 nm with θ_{ion} increasing from 26^o to 82^o.[15-17] Thus, the total number of displaced atoms is expected to be independent of θ_{ion}.

6.5. Absorption and emission

We now consider the contribution of the NP arrays to the absorption and DAP emission from GaAs. Since wavelength of the laser (633 nm) and the GaAs DAP emission (833 nm) are significantly larger than the NP diameters (33 - 69 nm) and NP spacing (70 - 140 nm), Bragg scattering is expected to be negligible. The SPR in NPs induces an evanescent field which enhances the incident EM field in the GaAs.[18-21] Since the incident laser energy (1.96 eV) is greater than that of the GaAs energy bandgap (1.51 eV at 10 K), the enhanced incident EM field

leads to an increase in absorption in the GaAs.[18-21] We estimate a 24 - 40 nm evanescent field which is a fraction of the 280 nm incident laser penetration depth, but significantly thicker than the < 6 nm ion-damaged surface layer. Meanwhile, for Ga NPs whose SPR energy matches the spectral range of GaAs, photons emitted by the recombination of DAPs are coupled into the SPR of Ga NPs,[22] leading to the suppression of the light emission.

6.6. Computation on absorption and emission

To compare the relative influences of the SPR-induced enhancement of the incident EM field and the suppression of the light emission, we computed the absorption efficiency spectra of Ga NPs on GaAs surfaces, using Mie's analytical solution to Maxwell's equations.[23-26] Based upon the SEM images in Fig. 6.1, and the cross-sectional STEM images[12], the Ga NPs consist of hemispheroidal shapes on the top of the irradiated GaAs surface. Therefore, the computations assume that hemispheroidal Ga NPs are on the GaAs surface[27], as shown in the inset to Fig. 6.2. In our case, an unpolarized laser is normally incident on the hemispheroidal Ga NPs, and the spectra for s- and p-polarizations both correspond to in-plane oscillations. Therefore, there is no peak splitting caused by image dipoles interacting differently with s- and p- polarization-dependent electron oscillations in NPs.[28-30] For Ga NPs with diameters ranging from 10 to 80 nm, the resulting absorption efficiency spectra are shown in Fig. 6.2. The NP size dependence of the absorption efficiency at the incident laser energy (1.96 eV) was extracted from the computed absorption efficiency spectra for various sized NPs in Fig. 6.2, namely the intersection of the dotted line with each spectrum. Since the computed absorption efficiency at 1.96 eV increases with decreasing d_{Ga} from 69 nm to 33 nm as shown in Fig. 6.3(a), the EM field enhancement is

also expected to increase with decreasing d_{Ga} from 69 nm to 33 nm.[31] To compute the NP size dependence of SPR energy, E_{SPR}, we used Lorentzian fits to the absorption efficiency spectra in Fig. 6.2, thereby locating the maximum likelihood E values for each d_{Ga}, which were in turn attributed to E_{SPR} for each d_{Ga}.[9] Since the difference in E_{SPR} of Ga NPs and E_g of GaAs decreases with decreasing d_{Ga} from 69 nm to 33 nm as shown in Fig. 6.3(b), the GaAs-Ga NP energy transfer-induced suppression of the light emission is predicted to increase with decreasing d_{Ga} from 69 nm to 33 nm. Therefore, Ga NP-induced enhancements of the incident EM field and GaAs-Ga NP energy transfer are expected to have opposite effects on PL efficiency of GaAs as d_{Ga} decreases from 69 nm to 33 nm.

6.7. Experimental photoluminescence spectra

Figure 6.4 presents PL spectra normalized by the integrated intensity of the absorbed laser light for regions of the GaAs layer with and without Ga NPs. DAP emissions of GaAs occur at 832 nm (1.491 eV). DAP emission of GaAs with Ga NPs (quantum efficiencies of 46.4 - 90.1 %) is greater than that of GaAs without Ga NPs (a quantum efficiency of 27.3 %). Also DAP emission of GaAs with Ga NPs increases with decreasing Ga NP size. Fig. 6.3(c) shows the PL enhancement, estimated as the ratio of the normalized PL intensities for regions of the GaAs layer with and without Ga NPs, as a function of d_{Ga}. The PL enhancement ranges from 1.7 to 3.3, consistent with the values predicted using the analytical model of Khurgin and Sun.[32,33] It is interesting to note that the PL enhancement is inversely proportional to d_{Ga}, with a maximum PL enhancement at the value of d_{Ga} (33.3 ± 1.3 nm) at which both enhancements of the incident EM field and GaAs-Ga NP energy transfer are predicted to be maximized. It is likely that the

enhanced absorption overwhelms the suppressed emission, producing the net PL enhancement; therefore, the PL enhancement is attributed to Ga NP SPR-induced absorption enhancement.

6.8. Summary and conclusions

In summary, we have examined the influence of surface Ga NPs on the enhancement of GaAs PL efficiency. We computed the absorption spectra of hemispheroidally-shaped Ga NPs on GaAs surfaces using Mie's analytical solution to Maxwell's equations. We fabricated close-packed arrays of Ga NPs via off-normal FIB irradiation of GaAs surfaces, and we measured the enhancement of PL efficiency as a function of d_{Ga}. The maximum PL enhancement occurs for the value of d_{Ga} predicted to maximize the incident EM field enhancement. The PL enhancement is driven by the SPR-induced enhancement of the incident EM field which overwhelms the SPR-induced suppression of the light emission.

6.9. Figures and references

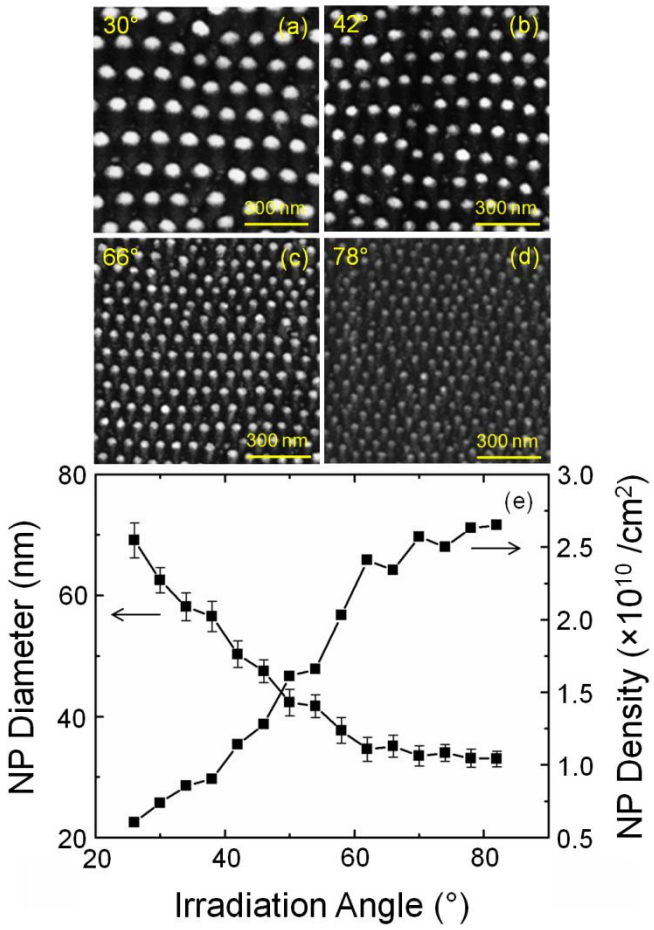

Fig. 6.1. SEM images of close-packed Ga NP arrays on GaAs surfaces irradiated at (a) $\theta_{ion} = 26^{\circ}$, (b) $\theta_{ion} = 42^{\circ}$, (c) $\theta_{ion} = 54^{\circ}$, and (d) $\theta_{ion} = 82^{\circ}$; (e) Plot of d_{Ga} (left) and n_{Ga} (right) as a function of θ_{ion} . It is interesting to note that n_{Ga} (d_{Ga}) is proportional (inversely proportional) to θ_{ion}, and the fractional surface coverages of Ga NPs is 23 ± 0.3 %.

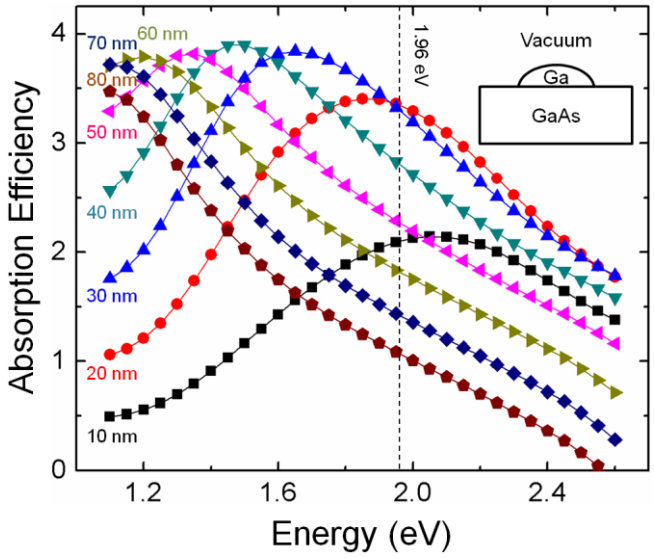

Fig. 6.2. Absorption efficiency spectra for Ga NPs (with diameters ranging from 10 to 80 nm), computed using Mie's analytical solution to Maxwell's equations, with the spectral dependence of the dielectric permittivities of GaAs and Ga NPs as input. The inset shows an illustration of hemispheroidally-shaped Ga NPs which share interfaces with both the GaAs substrate and vacuum. The dotted line corresponds to the incident laser energy (1.96 eV).

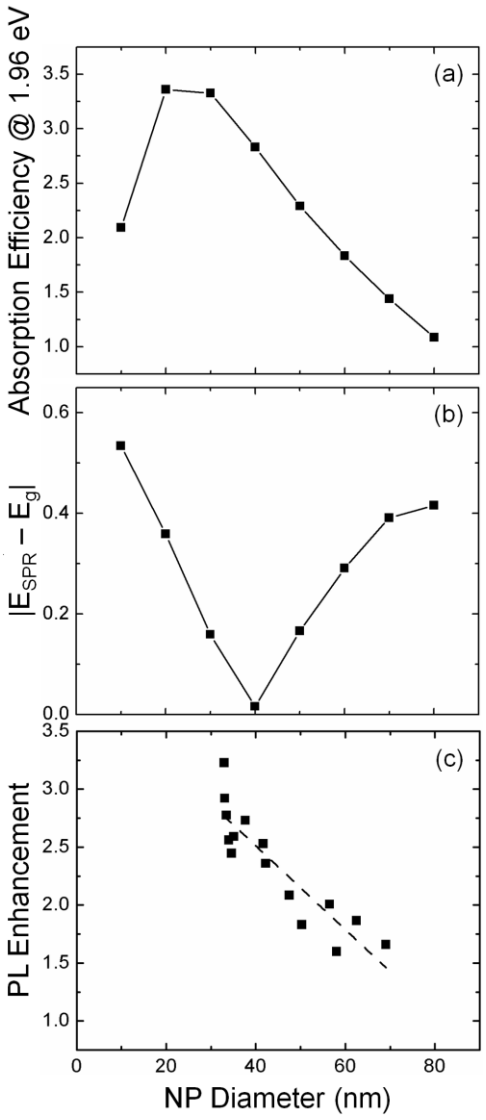

Fig. 6.3. (a) Computed absorption efficiency at 1.96 eV, (b) difference in computed E_{SPR} of Ga NPs and E_g of GaAs, and (c) measured PL enhancement, as function of d_{Ga}. In both (a), (b), and (c), the lines are intended to be guide to the eye. In (a), the Ga NP-induced incident EM field enhancement is predicted to increase with decreasing d_{Ga} from 69 nm to 33 nm. In (b), the GaAs-Ga NP energy transfer-induced suppression of the light emission is predicted to increase with decreasing d_{Ga} from 69 nm to 33 nm. In (c), the highest PL enhancement occurs for 33.3 ± 1.3 diameter Ga NPs.

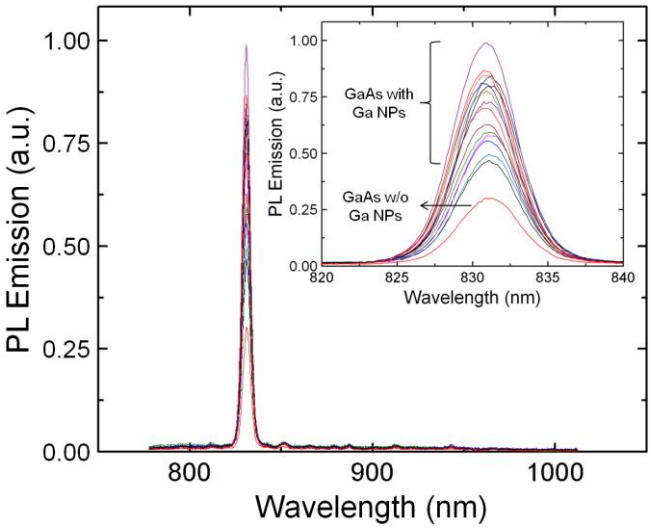

Fig. 6.4. PL spectra normalized by the integrated intensity of the absorbed laser light for regions of the GaAs layer with and without Ga NPs. DAP emissions of GaAs occur at 832 nm (1.491 eV). DAP emission of GaAs with Ga NPs is greater than that of GaAs without Ga NPs. Also DAP emission of GaAs with Ga NPs increases with decreasing Ga NP size.

[1]K. Okamoto, I. Niki, A. Shvartser, Y. Narukawa, T. Mukai, and A. Scherer, *Nature Mater.* **3**, 601 (2004).

[2]K. Nakayama, K. Tanabe, and H. A. Atwater, *Appl. Phys. Lett.* **93**, 121904 (2008).

[3]A. J. Haes, S. L. Zou, G. C. Schatz, and R. P. Van Duyne, *J. Phys. Chem. B* **108**, 6961 (2004).

[4]C. M. Soukoulis, S. Linden, and M. Wegener, *Science* **315**, 47 (2007).

[5]K. Munechika, Y. Chen, A. F. Tillack, A. P. Kulkarni, I. J. Pante, A. M. Munro, and D. S. Ginger, *Nano Lett.* **10**, 2598 (2010).

[6]A. A. Toropov, T. V. Shubina, V. N. Jmerik, and S. V. Ivanov, *Phys. Rev. Lett.* **103**, 037403 (2009).

[7]C. W. Cheng, E. J. Sie, B. Liu, C. H. A. Huan, T. C. Sum, H. D. Sun, and H. J. Fan, *Appl. Phys. Lett.* **96**, 071107 (2010).

[8]J. Lee, A. O. Govorov, J. Dulka, and N. A. Kotov, *Nano Lett.* **4**, 2323 (2004).

[9]M. Kang, T. W. Saucer, M. V. Warren, J. H. Wu, H. Sun, V. Sih, and R. S. Goldman, *Appl. Phys. Lett.* **101**, 081905 (2012).

[10]P. Wu, T. Kim, A. Brown, M. Losurdo, G. Bruno, and H. Everitt, *Appl. Phys. Lett.* **90**, 103119 (2007).

[11]T. W. Saucer, J.-E. Lee, A. J. Martin, D. Tien, J. M. Millunchick, and V. Sih, *Solid State Commun.* **151**, 269 (2011).

[12]M. Kang, J. H. Wu, S. Huang, M. V. Warren, Y. Jiang, E. A. Robb, and R. S. Goldman, *Appl. Phys. Lett.* **101**, 082101 (2012).

[13]Q. Wei, J. Lian, W. Lu, and L. Wang, *Phys. Rev. Lett.* **100**, 076103 (2008).

[14]J. H. Wu, W. Ye, B. L. Cardozo, D. Saltzman, K. Sun, H. Sun, J. F. Mansfield, and R. S. Goldman, *Appl. Phys. Lett.* **95**, 153107 (2009).

[15]M. Nastasi, J. W. Mayer, and J. K. Hirvonen, *Ion-Solid Interactions: Fundamentals and Applications*; Cambridge University Press: Cambridge, 1996.

[16]W. Ensinger, O. Lensch, T. Matsutani, and M. Kiuchi, *Surf. Coat. Tech.* **196**, 288 (2005).

[17]F. X. Wang, F. Lu, H. Hu, F. Chen, J. H. Zhang, and Q. M. Lu, *Appl. Surf. Sci.* **195**, 48 (2002).

[18]D. M. Schaadt, B. Feng, and E. T. Yu, *Appl. Phys. Lett.* **86**, 063106 (2005).

[19]C. Rockstuhl and F. Lederer, *Appl. Phys. Lett.* **94**, 213102 (2009).

[20]G. Sun and J. B. Khurgin, *Appl. Phys. Lett.* **97**, 263110 (2010).

[21]L. Hu, X. Chen, and G. Chen, *J. Comput. Theor. Nanosci.* **5**, 2096 (2008).

[22]A. Neogi, C. W. Lee, H. O. Everitt, T. Kuroda, A. Tackeuchi, and E. Yablonovitch, *Phys. Rev. B* **66**, 153305 (2002).

[23]G. Mie, *Ann. Phys.* **25**, 377 (1908).

[24]C. Bohren and D. Huffman, *Absorption and Scattering of Light by Small Particles*. (John Wiley & Sons, New York, 1982).

[25]C. Sonnichsen, Ph.D thesis (University of Munich, 2001).

[26]See supplemental material for computations of the size-dependence of SPR energies.

[27]R. J. Martin, *J. Mod. Optics* **40**, 2494 (1993).

[28]M. W. Knight, Y. Wu, J. B. Lassiter, P. Nordlander, and N. J. Halas, *Nano Lett.* **9**, 2188 (2009).

[29]P. Albella, B. Garcia-Cueto, F. Gonzalez, F. Morendo, P. C. Wu, T. Kim, A. Brown, Y. Yang, and H. O. Everitt, *Nano Lett.* **11**, 3531 (2011).

[30]M. W. Knight, J. Fan, F. Capasso, and N. J. Halas, *Opt. Express* **18**, 2579 (2010).

[31]N. Felidj, J. Aubard, and G. Levi, *J. Chem. Phys.* **111**, 1195 (1999).

[32]J. B. Khurgin and G. Sun, *J. Opt. Soc. Am. B* **26**, B83 (2009).

[33]Assuming that spherical Ga NPs, with diameters ranging from 33 to 69 nm, are embedded at the surface of GaAs, the PL emission is predicted to be enhanced by a factor of 12.6 to 18.5. Since the ratio of the evanescent field depth to the incident laser penetration depth ranges from 0.09 to 0.14, the weighted average PL enhancement is predicted to range from 2.0 to 3.5.

Chapter 7

SUMMARY AND SUGGESTIONS FOR FUTURE WORK

7.1. Summary

In this dissertation, FIB-induced fabrication and optical properties of metallic NPs on compound semiconductor surfaces were studied. Group III-rich metallic NPs were fabricated by FIB irradiation-induced preferential sputtering of Group V elements from III-V compound surfaces. The structure, composition, and properties of the metal-semiconductor heterostructures were investigated, and interplay between the formation, structure, and properties was discussed. Results presented in this thesis study suggest that FIB-induced Ga NPs are a promising alternative plasmonic material.

In Chapter 3, we used a combination of experiments and computations to examine the formation of ion irradiation-induced nanostructures consisting of Ga droplets on Ga-V surfaces, In islands on In-V surfaces, and Al islands on Al-V surfaces. We computed the ion doses needed to fully deplete group V elements from the surfaces. The group V depletion doses agree well with the threshold ion doses for nucleation of group III-rich droplets or islands. Since the group V depletion dose is inversely proportional to the sputtering yield of each III-V compound, we attribute the nanostructure formation to a mechanism based upon sputtering. This physical

mechanism may be used as a guide for nucleation of droplets or islands on a wide variety of compound semiconductor surfaces.

In Chapter 4, we examined origins of ion irradiation-induced Ga NP motion on GaAs surfaces. FIB irradiation of GaAs surfaces induces random walks of Ga NPs, biased opposite to the ion beam scan direction. v_i is constant, while v_d is linearly dependent on θ_{ion}, due to an enhanced $\Delta\delta$. It is hypothesized that the random walks are initiated by ion irradiation-induced thermal fluctuations, with biasing driven by anisotropic mass transport induced by $\Delta\delta$.

In Chapter 5, we demonstrated FIB-induced 2D square and 1D chain arrays of Ga NPs via pre-patterned holes on GaN surfaces where $d_{hole\text{-}hole}$, d_{hole}, and Z_{hole} determine $d_{Ga\text{-}Ga}$ ($d_{chain\text{-}chain}$), d_{Ga} (d_{chain}), and the array distribution, respectively. Extinction spectra of 2D square and 1D chain arrays reveal SPR energies in the visible and near-IR ranges. The SPR energies are blue-shifted with decreasing NP or chain diameter, due to particle diameter-dependent dipole interactions within the metallic NPs. This approach provides an opportunity to tune SPR over a wide energy range, with Q_{SPR} values comparable to those reported for Ag and Au NPs.

In Chapter 6, we examined the influence of surface Ga NPs on the enhancement of GaAs PL efficiency. We computed the absorption spectra of hemispheroidally-shaped Ga NPs on GaAs surfaces using Mie's analytical solution to Maxwell's equations. We fabricated close-packed arrays of Ga NPs via off-normal FIB irradiation of GaAs surfaces, and we measured the enhancement of PL efficiency as a function of d_{Ga}. The maximum PL enhancement occurs for the value of d_{Ga} predicted to maximize the incident EM field enhancement. The PL enhancement is driven by the SPR-induced enhancement of the incident EM field which overwhelms the SPR-induced suppression of the light emission.

7.2. Suggestions for future work

7.2.1. Overview

There are new questions that emerged as a consequence of this thesis study in terms of formation, property, and application for FIB-induced group III-rich metallic NPs. One of the remaining issues which have not been discussed in terms of NP formation is the evolution of irradiation-induced Ga NP arrays. FIB irradiation of pre-patterned GaAs surfaces induces monotonic increases in the NP volume and aspect ratio up to a saturation ion dose, independent of NP location within the array. Beyond the saturation ion dose, the NP volume continues to increase monotonically while the NP aspect ratio decreases monotonically. In addition, the NP volumes (aspect ratios) are highest (lowest) for the corner NPs.[1] Another important issue in terms of NP property is the spatial resolution of absorption measurement for SPR energy of NPs. Although the absorption measurement used in this thesis study is spatially resolved (1.5 μm), the resolution is still bigger than the diameter of NPs ranging from 30 nm to 200 nm. Recently, electron energy loss spectroscopy (EELS) has been used to observe lateral profiles of SPR of sub 10 nm-sized NPs along the NPs' diameter.[2] Finally, in terms of NP application, applying the ion-induced phenomena to a wide range of fields such as biochemistry and astrophysics is also a desirable approach. The preliminary results and specific suggestions for these topics are as follows.

7.2.2. Evolution of Ion-Induced Nanoparticle Arrays on GaAs Surfaces

Recently, focused-ion-beam (FIB) irradiation has been used to fabricate Ga NP arrays which exhibit SPR with performance comparable to those of silver and gold NPs.[3] In addition, these Ga NP arrays have enabled the enhancement of GaAs photoluminescence efficiency.[4] Furthermore, arrays of Group III-rich metallic NPs have been fabricated via FIB irradiation of a wide range of III-V compound semiconductor surfaces.[3-5] Typically, for finite-sized NP arrays, the corner NPs evolve to sizes larger than those of the side and interior NPs. It has been hypothesized that this array edge effect results from variations in the number of nearest neighbor NPs competing for the capture of diffusing Ga adatoms.[5] Here, we quantify the relative influences of bulk and surface diffusion on the evolution of ion-induced NP arrays. Initially, bulk Ga diffusion toward the bottom surface of the pre-patterned holes induces ion-dose-dependent monotonic increases in NP volume and NP aspect ratio up to a saturation value, independent of NP location within the array. Beyond the saturation ion dose, Ga surface diffusion enables the NP volume to continue increasing monotonically while the NP aspect ratio decreases monotonically. Interestingly, the NP volumes (aspect ratios) are highest (lowest) for the corner NPs. Thus, the NP array edge effect is driven primarily by Ga surface diffusion. The combination of bulk and surface diffusion is expected to be applicable to ion-induced NP array evolution on a wide variety of semiconductor surfaces.[5,6]

For the nanofabrication process, fifteen 5 × 5 arrays of holes with 300 nm diameter, 9 nm depth, and 1.5 μm interhole spacing were fabricated on GaAs surfaces, using FIB with 30 keV voltage, 50 pA current, and 1 μs dwell time. Subsequently, a Ga^+ ion beam with the same voltage, current, and dwell time was scanned over the region, containing the arrays. Following a

total dose of 2.3×10^{16} /cm^2, Ga NP formation was observed within the pre-patterned holes. We note that these ion irradiation conditions are expected to induce ~ 40 nm Ga-rich transition layer at the bottom surface of the pre-patterned holes.[5] Figure 7.1 shows representative scanning electron microscopy images of Ga NP arrays as a function of ion dose, ranging from 2.7×10^{16} to 4.8×10^{16} /cm^2. In each image, bright features corresponding to Ga NPs are observed. The dose-dependence of the Ga NP diameters, heights, and volumes are shown in Figs. 7.2(a), 7.2(b), and 7.2(c), where black, red, and blue symbols correspond to NPs on the array corner, side, and interior, respectively, as identified in the inset to Fig. 7.2(a). We assume that the NPs are spherical caps, with NP diameter, d, and height, h, such that the NP volume is $\pi h(3d^2 + 4h^2)/24$. Initially, the NP diameters, heights, and volumes increase monotonically with dose to a saturation value, independent of NP location within the array. Beyond the saturation dose, the NP diameters, heights, and volumes continue to increase monotonically. In addition, the NP diameters, heights, and volumes are highest for the corner NPs in comparison to those of the side and interior NPs.

To consider the relative roles of bulk and surface diffusion on NP array evolution, we consider the NP aspect ratio, h/d. As shown in Fig. 7.3, the NP aspect ratio increases monotonically with ion dose to a saturation value, independent of NP location within the array. In this regime, bulk Ga diffusion toward the hole edge leads to vertical Ga NP growth. Beyond the saturation ion dose, the NP aspect ratio decreases monotonically, with the lowest aspect ratios for the corner NPs in comparison to those of the side and interior NPs. In this regime, Ga surface diffusion to the NPs leads to lateral NP growth. The Ga NPs with fewer nearest neighbors are able to capture more Ga adatoms. For example, as shown in the inset to Fig. 7.2(a), Ga NPs on the corners, sides, and interiors of the arrays have two, three, and four nearest

neighbor NPs, respectively, resulting in the highest flux of captured Ga adatoms for the corner NPs. Therefore, the Ga surface diffusion-driven lateral growth of corner NPs is fastest for the corner NPs, leading to the lowest aspect ratio for the corner NPs.

A suggested future work is the extraction of ion irradiation-enhanced Ga bulk (surface) diffusivities in (on) GaAs from plots of ion dose-dependent Ga NP volumes. The increases in Ga NP volumes are proportional to fluxes of diffusing Ga atoms, enabling the extraction of Ga bulk (surface) diffusivities. Comparison of the resulting diffusivities with the values extrapolated from literature reports is also needed.

7.2.3. Electron energy loss spectroscopy measurements

In this thesis research, the absorption measurements used to quantify SPR energy of Ga NPs have 1.5 μm spatial resolution, much larger than the Ga NP diameters which range from 30 to 200 nm. Therefore, the data provide an ensemble-averaged value of SPR energies. To examine the SPR energies of individual NPs, an experimental method with a spatial resolution on the order of the size of the metallic NPs is needed.

Recently, electron energy loss spectroscopy (EELS) has been used to observe the local distribution of SPR energies inside sub 10 nm-sized metallic NPs.[2] EELS analyzes the distribution of the energies of electrons emergent from the TEM sample, from which SPR energies of the sample can be extracted. Since EELS is concerned with detecting the loss of electron energy due to an inelastic scattering, the resolution of EELS is not limited by the beam broadening effects, and therefore, EELS often has an excellent spatial resolution.[2]

7.2.4. Ion irradiation-induced DNA modification for dark matter detection

It has been expected that five-sixths of the matter in the universe consist of dark matter (DM) which does not interact via the electromagnetic or strong forces, rendering it invisible to our eyes and almost completely free to stream through our bodies.[7-9] The earliest evidence for dark matter was found by Fritz Zwicky.[10] While measuring the velocity dispersion of eight galaxies in the Coma cluster, he found that the they moved much more quickly than if they were only feeling the gravitational pull of the other visible objects. He concluded that there must be a significant amount of unseen matter within the cluster. Several questions remain: What is the "unseen matter" made of? How is it distributed throughout the Universe? How was it created? The community builds very sophisticated detectors to observe dark matter (DM) particles and study how they interact with themselves (indirect detection) and with ordinary matter (direct detection).[11] The number of experiments designed to detect the interaction of DM particles with nuclei increased significantly over the past few decades.[7-9] Although DM detectors which can spatially resolve length scales shorter than the penetration depth of the recoiling nucleus produced by incoming DMs have been proposed, they involve chambers which must be located underground for long time-period to minimize background noise.[12,13] A promising alternative approach to directional DM detection, consisting of 3D DNA arrays suspended from metal foils, has been proposed.[7-9]

The proposed approach for a DNA-based directional DM detector consists of thin parallel metal foils with arrays of DNAs hanging from them as shown in Fig. 7.4.[7-9] It is hypothesized that a DM particle would elastically scatter off a metal nucleus, sending the recoiling nucleus to travel through the arrays of suspended DNAs, cutting the strands it encounters. A recoiling

metal nucleus generated by DM-metal target collision is predicted to have an energy in the range 5 to 50 keV,[7-9,14] and the energetic metal nucleus cuts DNAs, generating strands. The strands would then fall away from the foil, and could be collected and analyzed. In general, the DM-induced fraction of cut DNAs, F, would be linearly related to the number of recoiling metal nuclei, N, by $F = \sigma N$ where σ corresponds to cross section of recoiling metal nucleus-DNA interaction.[14] At some values of N, N_{skin} for which recoiling metal nuclei of a given energy go as far as they can into the DNA and do not cause more DNA to be cut, F is expected to asymptotically approach a constant F_{max}. Intuitively, F_{max} depends on how deep the recoiling metal nuclei penetrate into the many layers of DNA. In general, F is expressed, as follows:

$$F = \begin{cases} \sigma N & \text{if } N < N_{skin} \\ F_{max} & \text{if } N \geq N_{skin} \end{cases}$$

The extraction of σ from plots of F vs. N will allow us to identify a type of recoiling nucleus, which in turn allows us to identify the origin (possibly DM) of recoiling nucleus generation.

To find σ, we study F as a function of N. To experimentally simulate the recoiling nuclei, we have used Ga^+ ions in FEI Nova dual beam FIB with an energy in the range 5 to 30 keV which is similar to the energy range (5 – 50 keV) of recoiling metal nucleus produced by DM-metal target interaction. Samples of DNAs were deposited in glass holders, and then irradiated by Ga^+ ion beam with ion doses ranging from 10^9 to 10^{13} /cm^2. Figure 7.5 shows a schematic diagram of the glass sample holder where Jordan Rowley in Andrzej Wierzbicki group injected (extracted) DNAs with pipettes. Glass was chosen to be a material for the sample holder to minimize ion irradiation-induced sputtering of the sample holder. The holders are loaded in the FIB chamber and the ion beam is located toward DNAs at normal incidence. The ion irradiation energy ranges from 5 to 10 keV, and the ion dose was varied for each sample. A simple way to

determine the relative lengths of ion irradiation-induced strands of DNA is gel electrophoresis as shown in Fig. 7.6.[15] Different samples of DNA, suspended in some liquid, are deposited into slots at one end of the gel. The gel is placed into a uniform electric field. The DNA, which is negatively charged, is pulled towards the positive electrode. Shorter strands of DNA are able to move more quickly through the gel than longer strands of DNA. We carried out two previous experiments where the first experiment involved plastic sample holders which presumably interfered with ion-DNA interactions due to ion irradiation-induced sputtering of plastic, and the second experiment involved heating of the glass holder including DNAs which presumably contributed to breaking DNAs. Therefore, the most recent experiments following these two were carried out with glass holders without thermal treatment.

Figure 7.7 shows plots of *F* vs. *N* for strands of DNA irradiated by 5 and 10 keV Ga ions from the most recent experiments. For both cases, it is interesting to note that *F* for double (single) stranded break increases (decreases) with *N*. Also, for double stranded break, *F* increases with *N* in a logarithm fashion rather than a linear fashion. Understanding these trends is in progress, and suggested future works include Ga^+ ion irradiation of DNAs with higher energies (15 - 30 keV) and variation of ions (Au and Ar) irradiated on DNAs.

7.3. Figures and references

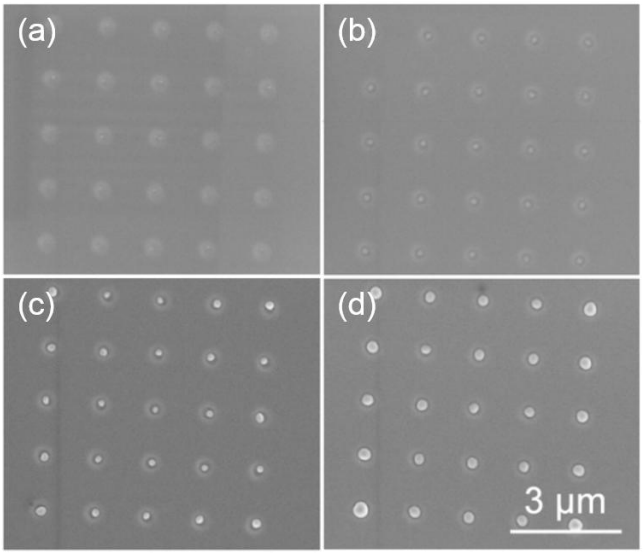

Fig. 7.1. SEM images of FIB-induced Ga NP arrays as a function of ion doses. Ga NP diameters appear to increase with ion dose, and the largest Ga NPs inhabit corners of arrays, followed by those on sides, and finally the smallest Ga NPs are found on interiors.

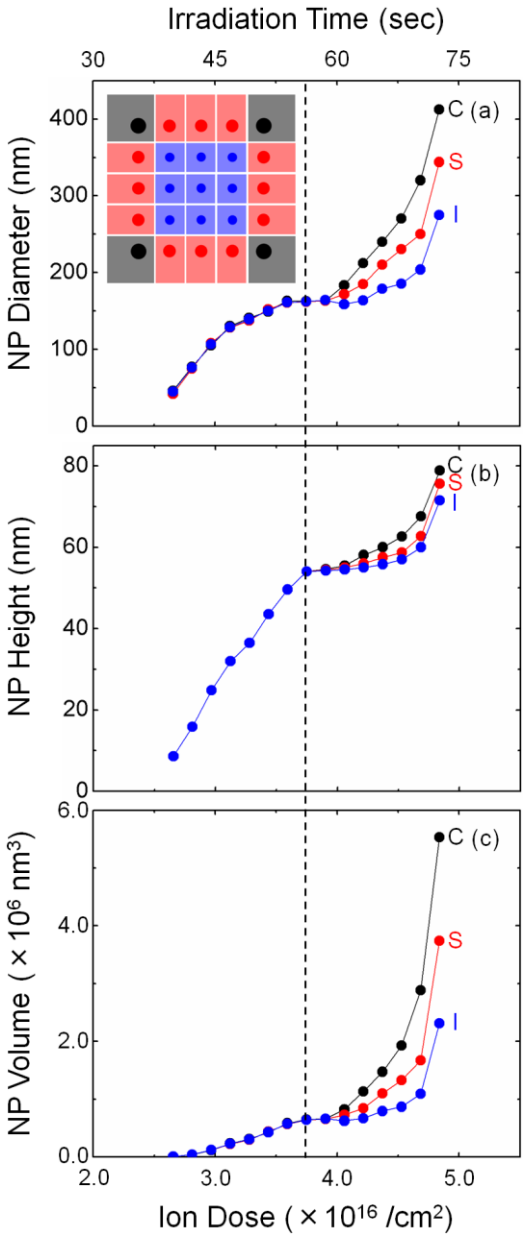

Fig. 7.2. Plots of diameters, heights, and volumes of Ga NPs vs. ion dose. An inset shows a schematic diagram of Ga NP arrays divided into three regions including corners (C), sides (S), and interiors (I) of arrays. Initially, the NP diameters, heights, and volumes increase monotonically with dose to a saturation value, independent of NP location within the array. Beyond the saturation dose, the NP diameters, heights, and volumes continues to increase monotonically. In addition, the NP diameters, heights, volumes are highest for the corner NPs.

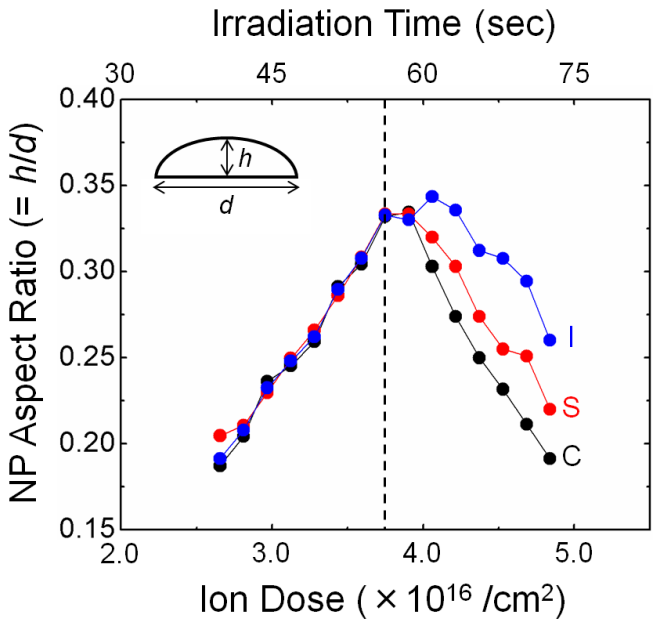

Fig. 7.3. Plots of aspect ratios of Ga NPs vs. ion dose. Initially, the NP aspect ratios, defined as *h*/*d* as shown in an inset, increase monotonically with dose to a saturation value, independent of NP location within the array. Beyond the saturation dose, the NP aspect ratio decreases monotonically, with the lowest aspect ratios for the corner NPs.

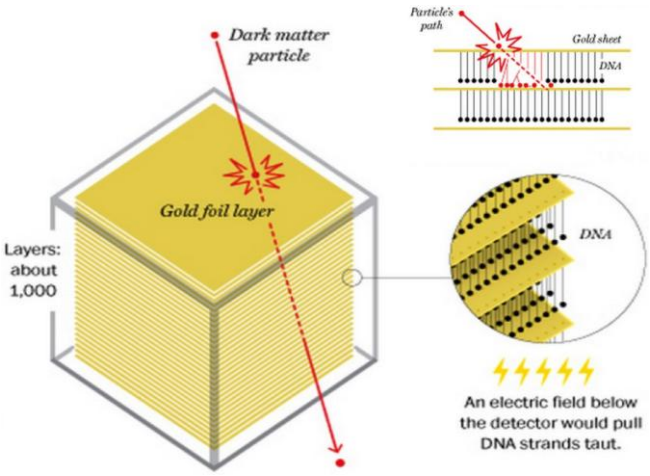

Fig. 7.4 A schematic diagram of the DNA dark matter detector.[7-9] A dark matter scatters elastically off a gold nucleus in the foil, sending that nucleus through the arrays of suspended DNAs. The nucleus breaks the strands it encounters.

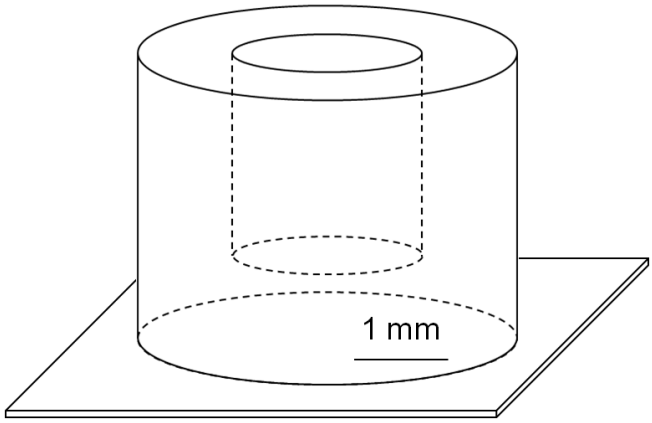

Fig. 7.5. A schematic diagram of the cup-shaped glass sample holder on the cover slip where DNAs are injected (extracted) by pipettes. Glass was chosen to be a material for the sample holder to minimize ion irradiation-induced sputtering of the sample holder. The holders are loaded in the FIB chamber and the ion beam is located toward DNAs at normal incidence.

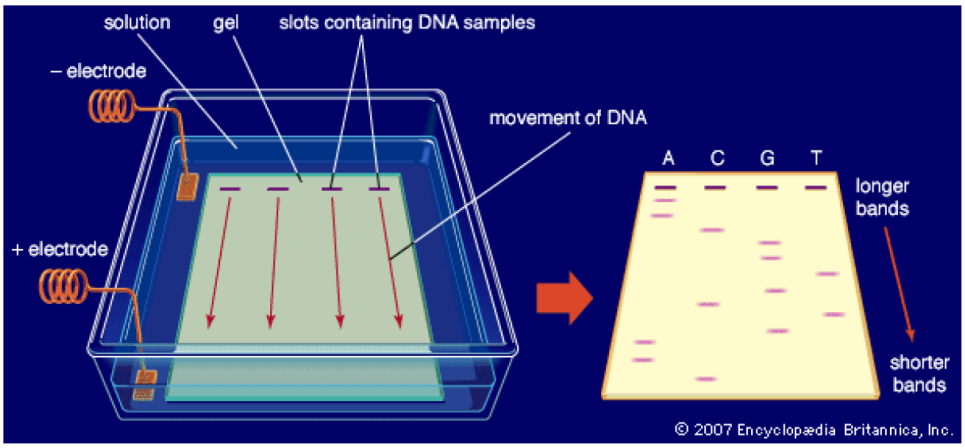

Fig. 7.6 A schematic diagram of gel electrophoresis.[15] The DNA is pipetted into the slots, and the electric field pulls the DNA through the gel. The shorter strands move faster than the longer strands.

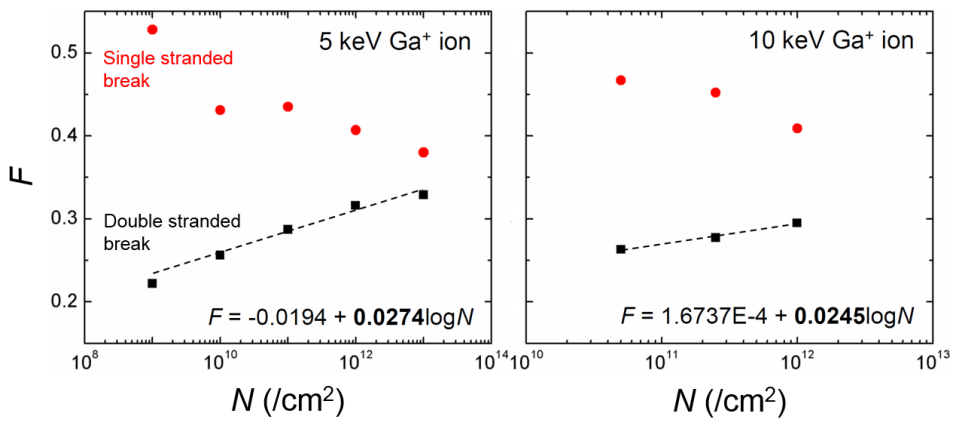

Fig. 7.7 Plots of *F* vs. *N* for strands of DNA irradiated by 5 and 10 keV Ga ions. For both cases, it is interesting to note that *F* for double (single) stranded break increases (decreases) with *N*. Also, for double stranded break, *F* increases with *N* in a logarithm fashion.

[1]M. Kang, I. Beskin, O. Shende, S. Huang, S. Jeon, A. A. Al-Heji, and R. S. Goldman (to be submitted)

[2]J. A. Scholl, A. L. Koh, and J. A. Dionne, *Nature* **483**, 421 (2012).

[3]M. Kang, T. W. Saucer, M. V. Warren, J. H. Wu, H. Sun, V. Sih, and R. S. Goldman, *Appl. Phys. Lett.* **101**, 081905 (2012).

[4]M. Kang, A. A. Al-Heji, J.-E. Lee, T. W. Saucer, S. Jeon, J. H. Wu, L. Zhao, A. L. Katzenstein, D. L. Sofferman, V. Sih, and R. S. Goldman, *Appl. Phys. Lett.* **103**, 101903 (2013).

[5]J. H. Wu, W. Ye, B. L. Cardozo, D. Saltzman, K. Sun, H. Sun, J. F. Mansfield, and R. S. Goldman, *Appl. Phys. Lett.* **95**, 153107 (2009).

[6]A. Botman, A. Bahm, S. Randolph, M. Straw, and M. Toth, *Phys. Rev. Lett.* **111**, 135503 (2013).

[7]A. K. Drukier, K. Freese, and D. N. Spergel, *Phys. Rev. D* **33**, 3495 (1986).

[8]K. Freese, "*New Dark Matter Detectors using DNA for Nanometer Tracking*", National Nanotechnology Initiative. Bonnie Berkowitz and Todd Lindeman - The Washington Post, (2012).

[9]M. M. Murskyj, Honors Senior Thesis (University of Michigan, 2013).

[10]F. Zwicky, *Helv. Phys. Acta* **6**, 110 (1933).

[11]L. Bergstrom, *Annalen Der Physik* **524**, 479 (2012).

[12]G. Sciolla, *Mod. Phys. Lett.* A **24**, 1793 (2009).

[13]D. N. Spergel, *Phys. Rev. D* **37**, 1353 (1988).

[14]C. Amsler, *Phys. Lett.* **B667**, 1 (2008).

[15]"*Gel Electrophoresis*", Encyclopedia Britannica, (2007).

Appendix A

Sample List

A.1. Sample list

This appendix describes details of samples used in this thesis study. Table A.1 presents types of III-V compound semiconductor substrates/templates, their surface crystallographic orientations, names of company/lab where the substrates/templates were purchased/grown, and research projects in which the substrates/templates were used.

Table A.1 Details of samples used in this study including types of substrates/templates, their surface orientations, names of company/lab where the samples were purchased/grown, and projects in which the samples were used

Substrate/ Template	Surface Orientation	Company/ Lab	Project
InSb	(001)	AXT	Formation[1]
InP	(001)	AXT	Formation[1]
InAs	(001)	AXT	Formation[1]
AlAs	(001)	AXT	Formation[1]
GaSb	(001)	AXT	Formation[1]
GaP	(001)	AXT	Formation[1]
GaAs	(001)	AXT	Formation[1], Motion[2]
1 μm GaAs buffer layers on GaAs (RMBE 590)	(001)	Substrate: AXT Buffer layer: Goldman group	PL[3]
GaAs	(111)	AXT	Motion[2]
5 μm GaN layers on Sapphire	(001)	Kyma Technologies	Formation[1], SPR[4]

Especially, for the fabrication of optically-active GaAs layer, we have fabricated a 1 μm GaAs buffer layer via exposure of Ga amd As_2 sources on bulk GaAs wafer in our Gen-II molecular beam epitaxy (MBE). The buffer layer was deposited at 580 ^{o}C with a V:III ratio of 12:1.

A.2. References

[1]M. Kang, J. H. Wu, S. Huang, M. V. Warren, Y. Jiang, E. A. Robb, and R. S. Goldman, *Appl. Phys. Lett.* **101**, 082101 (2012).

[2]M. Kang, J. H. Wu, D. L. Sofferman, I. Beskin, H. Y. Chen, K. Thornton, and R. S. Goldman, *Appl. Phys. Lett.* **103**, 072115 (2013).

[3]M. Kang, A. A. Al-Heji, J. -E. Lee, T. W. Saucer, S. Jeon, J. H. Wu, L. Zhao, A. L. Katzenstein, D. L. Sofferman, V. Sih, and R. S. Goldman, *Appl. Phys. Lett.* **103**, 101903 (2013).

[4]M. Kang, T. W. Saucer, M. V. Warren, J. H. Wu, V. Sih, and R. S. Goldman, *Appl. Phys. Lett.* **101**, 081905 (2012).

Appendix B

Determining Nanoparticle Size

B.1. Overview

This appendix describes the procedures used for identifying and quantifying the sizes of FIB-fabricated NPs on compound semiconductor surfaces based on SEM and AFM images. For these analyses, we utilized the Scanning Probe Image Processor (SPIP) and Origin software. We also discuss our method for determining NP size distributions. Types of size analysis conducted for each project are shown in Table B.1.

Table B.1. Types of size analysis conducted for each project

Project / Size	Formation[1]	Motion[2]	SPR[3]	PL[4]
Average/standard deviation	√	√	√	√
Distribution	√		√	

B.2. Procedure for determining the size of nanoparticles

To quantify the NP sizes,[1-4] SEM and AFM images consisting of 1024 × 884 and 1024 × 1024 pixels were opened in the SPIP software. For each NP, we performed the "single line profiling" across the NP center, saving the selected as a .dat file. We then open the ".dat" file in

Origin, and plot the first derivative of the height profile as a function of lateral distance. Finally, the lateral separation between the inflection points in the derivative of the height profile is defined as the NP diameter. An example of this procedure is shown in Fig. B.1.

B.3. NP size distribution

For all cases, the average and standard deviation of NP sizes were determined, as shown in Table B.1. In some cases, the NP size distributions were then determined as follows. Using bin sizes larger than the calculated standard deviations, we constructed histograms consisting of % vs. NP size, which were subsequently fit to single or bimodal log-normal distributions in Origin. The NP size distributions for SPR study were shown in Fig. 5.3,[2] while those of the formation study are shown in Fig. B.2.[1]

B.4. Figures and references

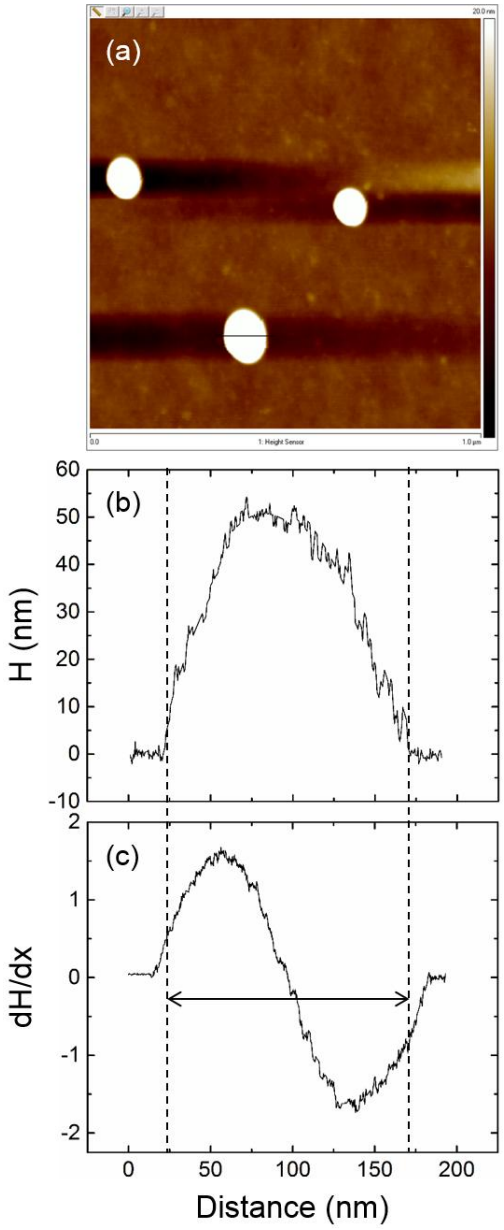

Fig. B.1. (a) The selected Ga NP with a line-cut across the NP center and (b) the corresponding height profile for the line-cut through the NP and (c) the first derivative of the height profile where the lateral separation between the inflection points indicated by vertical dashed lines is defined as the NP diameter.

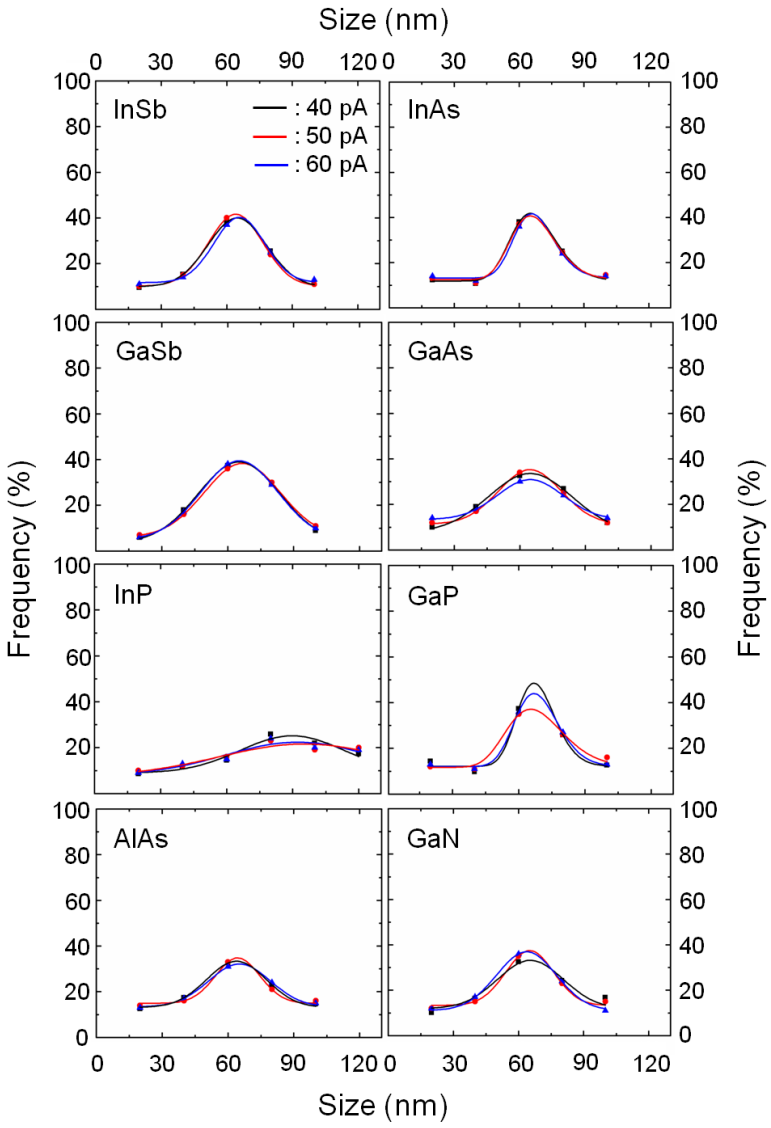

Fig. B.2. Size distributions for nanostructures fabricated at threshold ion doses on III-V compound semiconductor surfaces. The frequency is the percentage of NPs with diameters within a specified range, and fits to a log-normal distribution are shown as lines. The sizes of nanostructures nucleated at threshold ion doses are similar, ranging from 60 ± 20 to 80 ± 20 nm.

[1]M. Kang, J. H. Wu, S. Huang, M. V. Warren, Y. Jiang, E. A. Robb, and R. S. Goldman, *Appl. Phys. Lett.* **101**, 082101 (2012).

[2]M. Kang, J. H. Wu, D. L. Sofferman, I. Beskin, H. Y. Chen, K. Thornton, and R. S. Goldman, *Appl. Phys. Lett.* **103**, 072115 (2013).

[3]M. Kang, A. A. Al-Heji, J. -E. Lee, T. W. Saucer, S. Jeon, J. H. Wu, L. Zhao, A. L. Katzenstein, D. L. Sofferman, V. Sih, and R. S. Goldman, *Appl. Phys. Lett.* **103**, 101903 (2013).

[4]M. Kang, T. W. Saucer, M. V. Warren, J. H. Wu, V. Sih, and R. S. Goldman, *Appl. Phys. Lett.* **101**, 081905 (2012).

Appendix C

Calculation of Non-Stoichiometry

C.1. Calculations of sputtering yields

To calculate sputtering yields of the binary III-V compounds, we assume that the collision between incident ions and target atoms involves a linear collision cascade where the density of target atoms in motion remains sufficiently small so that collisions between atoms can be ignored.[1-4] With Y_{tot} estimated by Sigmund's sputtering theory,

$$Y_{tot} = \frac{4.2\alpha S_n}{U_{target}} \tag{1}$$

where α is the correlation factor; S_n is the nuclear stopping cross section; and U_{target} is the cohesive energy. Equations for α and S_n are as follows:[1-4]

$$\alpha = 0.15(1+\frac{m_{target}}{m_{Ga}})^{0.85} \tag{2}$$

$$S_n(E_0) = \frac{8.462\times10^{-15} Z_{Ga} Z_{target} m_{Ga} S_n(\varepsilon)}{(m_{Ga}+m_{target})(Z_{Ga}^{0.23}+Z_{target}^{0.23})} \tag{3}$$

where Z_{Ga}, Z_{target}, m_{Ga}, m_{target}, and $S_n(\varepsilon)$ are the atomic numbers of incident Ga^+ ion and target material, the atomic masses of incident Ga^+ ion and target material, and the nuclear stopping

cross section as a function of the reduced energy, ε.[1] For ε < 30 where nuclear stopping is dominant over electron stopping in our case, $S_n(\varepsilon)$ is expressed as follows:

$$S_n(\varepsilon) = \frac{\ln(1+1.1383\varepsilon)}{2(\varepsilon + 0.01321\varepsilon^{0.21226} + 0.19593\varepsilon^{0.5})} \tag{4}$$

where ε is expressed as follows:

$$\varepsilon = \frac{32.53 m_{target} E_0}{Z_{Ga} Z_{target} (m_{Ga} + m_{target})(Z_{Ga}^{0.23} + Z_{target}^{0.23})} \tag{5}$$

For binary compounds, we use a law of mixtures to calculate atomic mass (m_{target}), atomic number (Z_{target}), and surface binding energy (U_{target}) of target material.[4]

C.2. Derivation of the non-stoichiometry

To derive an expression for the non-stoichiometry of the group-III rich surface region, we define a projected volume and calculate the non-stoichiometry within that volume. At the surface, defined as z = 0, the normal-incidence ion beam produces a nearly circular cross-sectional area with radius, R_0. We assume a Gaussian increase in the lateral projected range, R(z), from $R(0) = R_0$ at the surface (z = 0) to $R(z_p) = R_p$ at the endpoint of the ion trajectory (the longitudinal projected range, $z = z_p$) as follows:[1-4]

$$R(z) = R_p e^{\frac{-\ln\frac{R_p}{R_0}}{z_p}(z-z_p)^2} \tag{6}$$

The projected volume, V_p, is then determined by integrating the circular cross-sectional area as a function of the depth from z = 0 to z_p, as shown in Fig. C.1.

For an initially stoichiometric surface,

$$N_{III}(0) = N_V(0) = \frac{V_p \rho}{M_{III} + M_V} \tag{7}$$

where $N_{III}(0)$ and $N_V(0)$ are the initial number of group III and V atoms in the projected volume; V_p is the projected volume; ρ is the mass density of the III-V compound; and $M_{III\,(V)}$ is the atomic mass of group III (V) elements. The sum of the sputtered group III and V elements are expressed as follows:

$$N_{S,III}(t) + N_{S,V}(t) = (Y_{III} + Y_V) \cdot \frac{dN_{ion}}{dt} \cdot t \tag{8}$$

where dN_{ion}/dt is the Ga^+ ion dose rate, quantified as $dN_{ion}/dt = I/qA$ (I = ion beam current, q = elementary charge, and A = the cross-sectional area); t is the irradiation time; $Y_{III\,(V)}$ is the sputtering yield of group III (V) elements. The resulting the number of extra group III elements following ion-irradiation for a time t is expressed as follows:

$$N_{S,V}(t) - N_{S,III}(t) = (Y_V - Y_{III}) \cdot \frac{dN_{ion}}{dt} \cdot t \tag{9}$$

where $N_{S,III}(t)$ and $N_{S,V}(t)$ are the number of atoms sputtered from the projected volume following ion-irradiation for a time t. We define the surface non-stoichiometry, δ, in terms of $III_{1+\delta}V_{1-\delta}$. Following ion-irradiation for a time t, δ is given by the ratio of the difference to the sum of group III ($N_{III}(t)$) and group V ($N_V(t)$) elements within V_p.

$$\delta = \frac{[N_{III}(t) - N_V(t)]}{[N_{III}(t) + N_V(t)]} \tag{10}$$

where $N_{III}(t)$ and $N_V(t)$ are defined as follows:

$$N_{III}(t) = N_{III}(0) - N_{S,III}(t) \tag{11}$$

$$N_V(t) = N_V(0) - N_{S,V}(t) \tag{12}$$

Finally, the resulting expression for the non-stoichiometry following ion-irradiation for time *t* is formulated as follows:

$$\delta(t) = \frac{(Y_V - Y_{III}) \cdot \frac{dN_{ion}}{dt} \cdot t}{[2N_{III}(0) - (Y_{III} + Y_V) \cdot \frac{dN_{ion}}{dt} \cdot t]} \tag{13}$$

As shown in Fig. C.2, the beam spots have overlapped regions where δ was calculated as a function of ion dose. We computed δ in the regions of beam spot overlap as a function of ion dose. Plots of the non-stoichiometry vs. ion dose are presented in Fig. C.3.

C.3. Figures and references

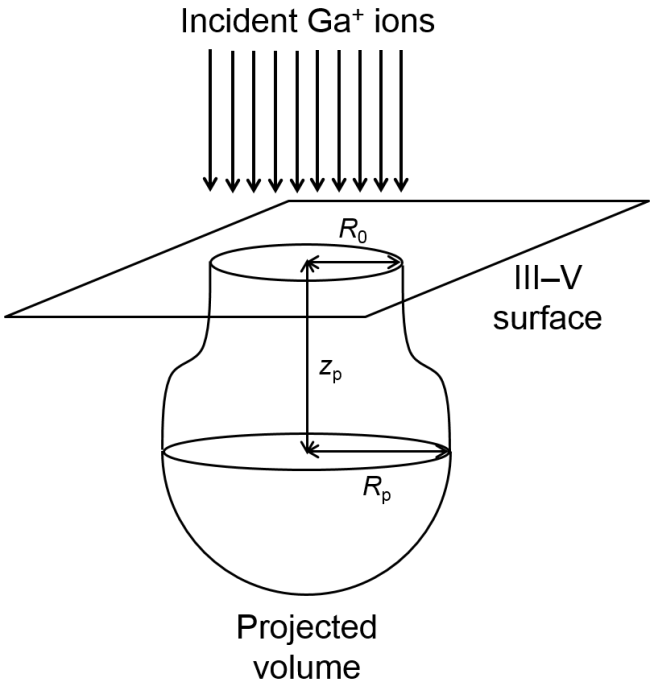

Fig. C.1. A schematic diagram of the projected volume produced by an ion beam incident upon III-V compound semiconductor surfaces. R_0, z_p, and R_p correspond to the radius of beam spot, longitudinal projected range, and lateral projected range, respectively.

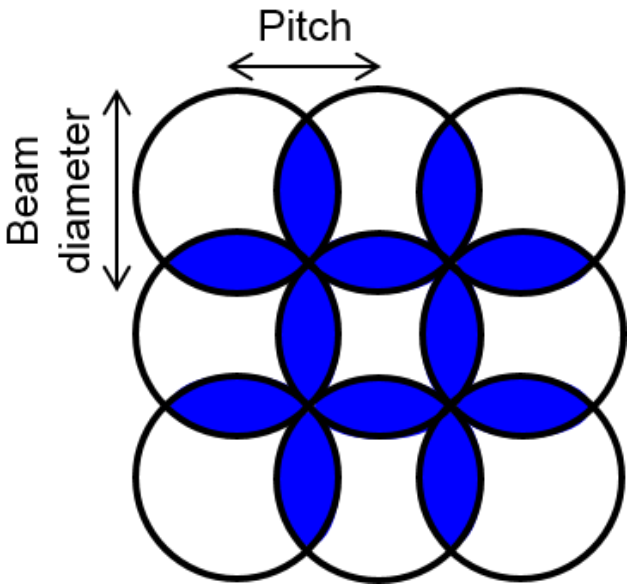

Fig. C.2. A schematic diagram of beam diameter, pitch, and ion beam overlap. In the regions of ion beam overlap, δ is computed as a function of ion dose.

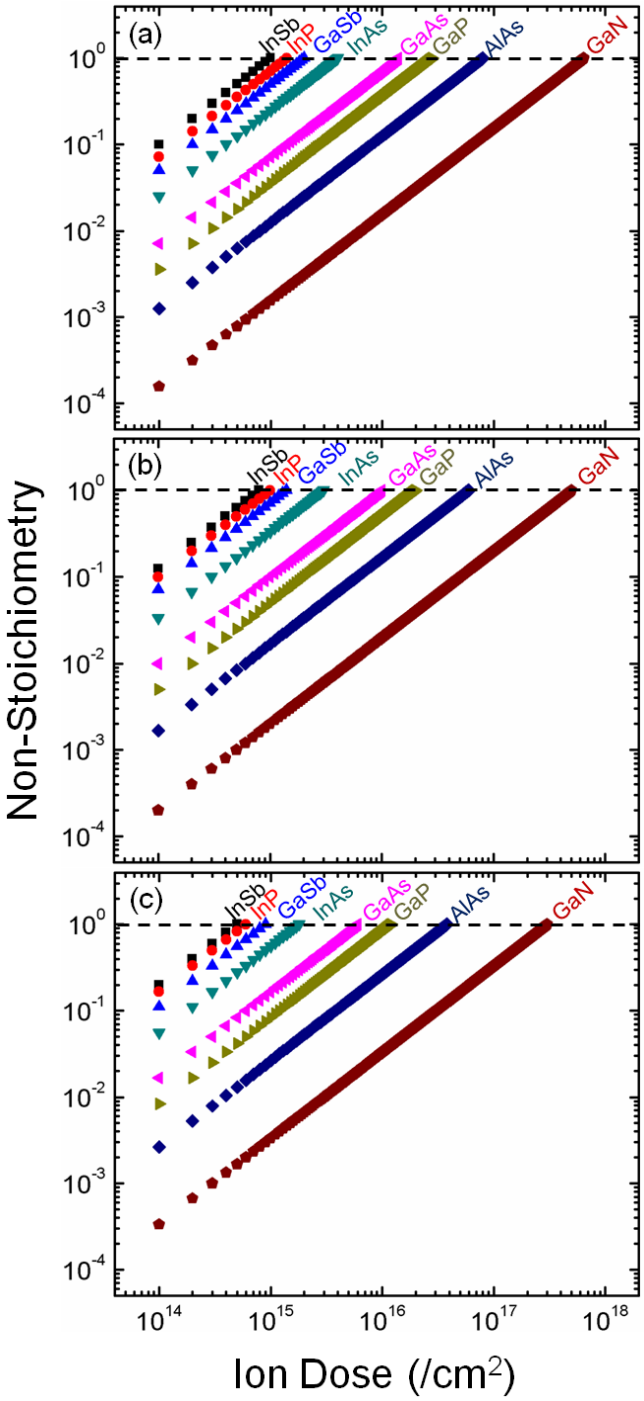

Fig. C.3. Plots of the non-stoichiometry vs. ion dose for (a) 40 pA, (b) 50 pA, and (c) 60 pA ion current. The non-stoichiometry increases with increasing ion dose; the dose at which δ = 1, shown as a dashed horizontal line, is considered to be the computed Group V depletion dose.

[1]P. Sigmund, *Phys. Rev.* **184**, 383 (1969).

[2]J. Orloff, M. Utlaut, and L. Swanson, *High Resolution Focused Ion Beams*; Kluwer Academics/Plenum Publishers: NY, 2003.

[3]M. Nastasi, J. W. Mayer, and J. K. Hirvonen, *Ion-Solid Interactions: Fundamentals and Applications*; Cambridge University Press: Cambridge, 1996.

[4]J. Tesmer and M. Nastasi, *Handbook of Modern Ion Beam Materials Analysis*; Materials Research Society: PA, 1995.

Appendix D

Tracking of Nanoparticle Motion

D.1. Process of nanoparticle tracking

The codes have been developed in the Interactive Data Language (IDL) by Jia-Hung Wu in Goldman group and Hsun-Yi Chen in Thornton group, utilized to track Ga NP motion on FIB-irradiated GaAs surfaces. The codes are named "PRO readimage" and "PRO tracking". Both codes were written to input .tif image file. "PRO readimage" identifies Ga NPs in terms of its position and radius in each image frame via the contrast difference between Ga NPs and GaAs surfaces. Subsequently, "PRO tracking" tracks Ga NPs in consecutive image frames.

Movies of real-time Ga NP motion were recorded by collecting ion irradiation-induced secondary electrons. The movies include an imaging area of $6.3 \times 5.4\ \mu m^2$, consisting of 512×440 pixels. Image frames are extracted from the movies every 0.1 s, and saved as .tif image files. "PRO readimage" reads .tif image files, and converts pixels in the data into arrays of gray-scale values. The gray-scale threshold for identification of Ga NPs and GaAs surfaces is then determined. Subsequently, "PRO readimage" labels each Ga NP with (#, x, y, r) where # is the frame number, x and y are the positions of the Ga NP center of mass, and r is the equivalent circular radius of the Ga NP. Since the Ga NPs are not typically exactly circular, the code counts up all pixels in a Ga NP, identifies the center of mass for those pixels, and builds an equivalent

circular region surrounding the center of mass. After PRO readimage labels all Ga NPs in each image frame, the indices are used to track the Ga NP motions in consecutive frames by "PRO tracking".

D.2. IDL codes

PRO readimage

```
window,xsize=512,ysize=440
Finalarr = make_array(335, 5, 200,/float,value = 0)
for J = 0L, 334L, 1L do begin
filename = STRCOMPRESS('/Applications/IDL/test(.1nA)_154/'+STRING(j)+'.jpg',
/REMOVE_ALL)
read_jpeg, filename, gray_image
; Smooth and threshold gray scale image
sgi=smooth(gray_image,6,/edge_truncate)
if (j ge 0 and j le 50) then threshImg = smooth(sgi,2,/edge_truncate) GE 193
        sgi=smooth(gray_image,7,/edge_truncate)
        threshImg = smooth(sgi,3,/edge_truncate) GE 195
endif
; Label the particle and display it in window 0
regions = LABEL_REGION(threshImg)
hist = HISTOGRAM(regions)
; define the criterion for particle area and get rid of the small particles, which are likely be
```

```
noise
;Plot particle Area Size Distribution histogram
index = where (hist lt 100000 AND hist gt 0)
areas = hist(index)
bin_size=1
ASD=histogram(areas,binsize=bin_size, locations=xbin)
xbin=xbin + bin_size/2.
;Calculate the particle radius and plot a particle radius histogram
radii = (areas/3.14)^0.5
bin_size=1.5
PSD = HISTOGRAM (radii, locations=xbin,max=15, min=0,nbin=10)
xbin=xbin+bin_size/2
xbin=[min(xbin)-bin_size,xbin]
PSD=[0,PSD]
;To count the particle number of each snapshot
PN = n_elements(index)
; To calculate index of all selected particles in every snapshot
  for i = 1L, PN, 1L do begin
    PI = where (regions eq i, count)
      y =floor (PI/512)
        finalarr[j,2,i] =total(y)/n_elements(y)
          x = (PI-512*y)
        finalarr[j,1,i]=total(x)/n_elements(x)
```

```
      finalarr[j,3,i] = (count/3.14)^0.5
     finalarr[j,4,i] = count
    finalarr =i
  endfor
endfor
; to save the finalarr in a new file
save, finalarr, filename = '/Applications/IDL/test(.1nA)_154/finalarr.sav'
stop
END
```

PRO tracking

```
;track the particles in consecutive frames
; 1 pixel = 12.269939 nm
restore, '/Applications/IDL/test(.1nA)_154/finalarr.sav'
;create a trackingarr and strat to track
frames=335
dropletsInst=200
Compared_arr1 = make_array(frames, 2, 4202,/float)
Compared_arr2 = make_array(frames, 2, 4202,/float)
Result_arr = make_array(frames, 1, 4202,/float)
correspondarr=make_array(frames,4202,/float,value=-1)
transferarr=make_array(frames,5,dropletsInst,/float)
```

```
;if the particle area is less than 25 pixels, it is defined as being noise, so zeroed and erased from
final array
for A=0,(frames - 1) do begin
for P=0,(dropletsInst - 1) do begin
        if finalarr[A,4,P] lt 25 then begin
                finalarr[A,1,P]=0
        endif
endfor
endfor
y=0
for r=0,(dropletsInst - 1) do begin
  existence=where(finalarr[*,1,R] gt 0)
  if existence[0] ge 0 then begin
    transferarr[*,*,y]=finalarr[*,*,r]
    transferarr[*,0,y]=y
    y++
  endif
endfor
finalarr=0
finalarr=transferarr
save,finalarr,filename='/applications/idl/test(.1nA)_154/finalarr2.sav
Trackingarr = make_array(frames, 5, 4202,/float)
for N=0,(dropletsInst - 1) do begin
```

```
  Trackingarr[0,*,N] = finalarr[0,*,N]
  correspondarr[0,N]=N
endfor
numberTracked = n_elements(where(trackingarr[0,1,*] gt 0))
for G=0,(frames - 2),1 do begin
print,G
for M = G, G do begin
 for K = 0L, 4201L, 1L do begin
  Oldmin = 4200
   for L = 0, (dropletsInst - 1) do begin
Newmin = abs(Finalarr[M+1,1,L]-trackingarr[M,1,K]) + abs(Finalarr[M+1,2,L]-
trackingarr[M,2,K]) + abs(Finalarr[M+1,3,L]-trackingarr[M,3,K])
; if the corresponding newmin smaller then previous one, the particle is identified as the same
one
    if Newmin lt Oldmin then begin
     trackingarr[M+1,1,k] = finalarr[M+1,1,L]
      trackingarr[M+1,2,k] = finalarr[M+1,2,L]
     trackingarr[M+1,3,k] = finalarr[M+1,3,L]
    trackingarr[M+1,4,k] = finalarr[M+1,4,L]
    Oldmin = Newmin
    Lfinal=L
   endif
     trackingarr[M+1,0,k] = k
```

```
   endfor
     correspondarr[M+1,k]=Lfinal
 endfor
endfor
;if the particle radius increase more than twice, the particle is defined as being merged
   for o = 0L, 4201L, 1L do begin
     deltaR1 = (trackingarr[G+1,3,o]-trackingarr[G,3,o])/trackingarr[G,3,o]
      if trackingarr[G,1,o] NE 0 and trackingarr[G,2,o] NE 0 then begin
       if abs(deltaR1) gt 1 then begin
         trackingarr[G+1,1,o]=0
         trackingarr[G+1,2,o]=0
       endif
     endif
   endfor
;save the tracking result and compare it with the result after velocity limit criterion
;Compared_arr1 = make_array(frames, 2, dropletsInst,/float)
    for D = 0L, 4201L, 1L do begin
      Compared_arr1(G,0,D) = trackingarr(G,1,D)
        Compared_arr1(G,1,D) = trackingarr(G,2,D)
     endfor
;if the particle velocity is larger than its radius between two consecutive frames and larger than
228nm/s
   ;this particle is defined as disappeared and its trackingarr[N,3,O] are set as 0
```

```
for B = 0L, 4201L, 1L do begin
  P_velocity = 61.35*((trackingarr[G+1,1,B]-
trackingarr[G,1,B])^2+(trackingarr[G+1,2,B]-trackingarr[G,2,B])^2)^0.5
  if (P_velocity gt (61.35 * trackingarr[G,3,B]) and P_velocity gt 228) then begin
    trackingarr[G,1,B]=0
    trackingarr[G,2,B]=0
  endif
endfor
;save the tracking result and compare it with the result after particle merged criterion
;Compared_arr2 = make_array(frames, 2, dropletsInst,/float)
;Result_arr = make_array(frames, 1, dropletsInst,/float)
   for F = 0L, 4201L, 1L do begin
   Compared_arr2(G,0,F) = trackingarr(G,1,F)
    Compared_arr2(G,1,F) = trackingarr(G,2,F)
    Result_arr(G,0,F) = compared_arr1(G,0,F) - compared_arr2(G,0,F)
   endfor
;The particle indices in the frame which is after the frame with xy indices = [0,0] are set as
[0,0,0,0]
  for s=0,4201 do begin
        I=where(trackingarr[*,1,S] ne 0)
        I2=where(trackingarr[*,1,S] ne 0)
        if I[0] eq -1 and I2[0] eq -1 then continue
  if trackingarr[G,1,S] eq 0 or trackingarr[G,2,S] eq 0 then begin
```

```
      for H = G, (frames - 2) do begin
        trackingarr[H,1,S] = 0
        trackingarr[H,2,S] = 0
        trackingarr[H,3,S] = 0
        trackingarr[H,4,S] = 0
            correspondarr[H,S]=-1
      endfor
    endif
  endfor
;add new particles from finalarr
for C=0, (n_elements(where(finalarr[G+1,1,*] gt 0)) - 1) do begin
counted=0
for E=0,4201 do begin
   if correspondarr[G+1,E] eq C then counted = 1
endfor
if counted ne 1 then begin
          trackingarr[G+1,1,numberTracked]=finalarr[G+1,1,C]
          trackingarr[G+1,2,numberTracked]=finalarr[G+1,2,C]
          trackingarr[G+1,3,numberTracked]=finalarr[G+1,3,C]
          trackingarr[G+1,4,numberTracked]=finalarr[G+1,4,C]
          trackingarr[G+1,0,numberTracked]=numberTracked
          numberTracked++
  endif
```

```
endfor
endfor
;if the particle only lasted under 10 seconds it is defined as being noise
for Q=0,4201 do begin
  duration=where(trackingarr[*,1,Q] gt 0)
  duration2=where(trackingarr[*,2,Q] gt 0)
  if duration[0] eq -1 and duration[0] eq -1 then continue
  if n_elements(duration) lt 50 then begin
      trackingarr[*,1,Q] = 0
      trackingarr[*,2,Q] = 0
      trackingarr[*,3,Q] = 0
      trackingarr[*,4,Q] = 0
  endif
endfor
;check the particle path
window,3,title='particle path 0'
plot,trackingarr[*,1,0],trackingarr[*,2,0],psym=-6
Window, 2, TITLE='particle path 20'
plot, trackingarr[*,1,20], trackingarr[*,2,20], psym=-6
Window, 3, TITLE='particle path 42'
plot, trackingarr[*,1,42], trackingarr[*,2,42], psym=-6
for zz=0,650 do begin
        print,string(zz) + string(n_elements(where(trackingarr[*,1,zz] gt 0)))
```

```
endfor
save,trackingarr,filename='/applications/idl/test(.1nA)_154/trackingarr.sav
stop
END
```

Appendix E

Calculation of Mie Analytical Solution

E.1. Overview

This appendix is intended to validate our computations in PL studies and provide Mathematica code for the Mie analytical solution to Maxwell equations. As shown in Fig. D.1, we consider that monocromated light (0.5 - 2.5 eV) is incident on hemispheroidal Ga NPs on both GaAs and GaN surfaces for the computation. Real and imaginary parts of dielectric functions of Ga, GaAs, and GaN are inserted into the Mie analytical solution to Maxwell equations. We vary Ga NP diameter (10 - 200 nm) in the code to compute SPR energy of Ga NPs on each surface as a function of Ga NP diameter.

E.2. Validity of computations in our study

Although SPR energies of metallic NPs are dependent on the dielectric properties of both the NPs and the substrates, the SPR energies of Ga NPs on GaAs surfaces have not been reported. Typically, for Ga NPs with $d_{Ga} < 100$ nm, SPR energies in the range 2.0 to 5.8 eV have been reported. However, the bandgap energy of GaAs at 10 K is 1.5 eV. Thus, incident EM waves that would be influenced by Ga NPs would likely also be absorbed by the GaAs substrate.

Therefore, to predict the expected SPR energy of Ga NPs, a validated computation is required. We have validated computations using the Mie analytical solution to Maxwell equations[1-4] through a comparison with experimental absorption efficiency spectra of Ga NPs on GaN.[5] Figure D.2 presents computed SPR energies for Ga NPs on GaAs and GaN surfaces, in comparison with measured SPR energies for Ga NPs on GaN surfaces. As shown in Fig. D.1, both the computed and measured SPR energies for Ga NPs on GaN surfaces are inversely proportional to the Ga NP diameter, with similar ranges of energy values. The computed SPR energies for Ga NPs on GaAs are also inversely proportional to the Ga NP diameter. It is interesting to note that the SPR energies are very different for Ga NPs on GaAs and GaN surfaces, consistent with earlier studies showing the SPR energies for Ga NPs on various surfaces.[6]

E.3. Mie analytical solution

The Mie analytical solution describes the response of metallic NPs to an incident EM field where the size of NPs is much smaller than the wavelength of incident EM wave so that the electromagnetic phase is constant throughout the uncharged NPs.[1-3] Especially, we are interested in the absorption efficiency where SPR energies can be determined, The absorption efficiency is expressed as follows:[1-3]

$$A^{(n)} = \frac{2}{x^2}(2n+1)[\mathrm{Re}(a_n + b_n) - |a_n|^2 - |b_n|^2]$$

with $A^{(n)}$ = absorption efficiency, $x = kr$ (k = wave vector and r = NP radius), n = multipole extension of the field ($n = 1$ for dipole mode and $n \geq 2$ for multipole mode)

and a_n and b_n = Mie coefficients, which are expressed by:[1-3]

$$a_n = \frac{m\psi_n(mx)\psi'_n(x) - \psi_n(x)\psi'_n(mx)}{m\psi_n(mx)\xi'_n(x) - \xi_n(x)\psi'_n(mx)}$$

$$b_n = \frac{\psi_n(mx)\psi'_n(x) - m\psi_n(x)\psi'_n(mx)}{\psi_n(mx)\xi'_n(x) - m\xi_n(x)\psi'_n(mx)}$$

where $m = \varepsilon_{particle}/\varepsilon_{med}$ ($\varepsilon_{particle}$ and ε_{med} = NP and medium dielectric functions), and ψ_n and ξ_n = Riccati-Bessel functions.[2] Therefore, the expression for the absorption efficiency includes input parameters including r, $\varepsilon_{particle}$, and ε_{med} from which we can calculate the NP size-dependent spectral absorption efficiency of any combination of metallic NP and medium. The symbols for input parameters used in the text and code are shown in Table D.1, and the code using Mathematica software is followed:[3]

Table E.1. Symbols for input parameters used in the text and code

	Text	**Code**
NP diameter	r	
NP dielectric function	$\varepsilon_{particle}$	$N_{particle}$
Medium dielectric function	ε_{med}	N_{med}
Absorption efficiency	A	Q_{abs}

```
j [n_, x_] := (Sqrt [Pi / (2 x)]) BesselJ [n + 1 / 2, x]

y [n_, x_] := (Sqrt [Pi / (2 x)]) BesselY [n + 1 / 2, x]

h1 [n_, x_] := j [n, x] + i y [n, x]

h2 [n_, x_] := j [n, x] – i y [n, x]

psi [n_, x_] := x j [n, x]

xi [n_, x_] := x h1 [n, x]
```

psidev [n_, x_] := Derivative [0, 1] [psi] [n, x]

xidev [n_, x_] := Derivative [0, 1] [xi] [n, x]

a [n_, x_, m_] := (m psi [n, m x] psidev [n, x] – psi [n, x] psidev [n, m x]) / (m psi [n, m x] xidev [n, x] – xi [n, x] psidev [n, m x])

b [n_, x_, m_] := (psi [n, m x] psidev [n, x] – m psi [n, x] psidev [n, m x]) / (psi [n, m x] xidev [n, x] – m xi [n, x] psidev [n, m x])

X [w_, r_] := w r Nmed / 197

M [w_] := Nparticle [w] / Nmed

Qsca [n_, w_, r_] := (2 / X [w, r] ^2) (2 n + 1) (Abs [a [n, X [w, r], M [w]]] ^2 + Abs [b [n, X [w, r], M [w]]] ^2)

Qext [n_, w_, r_] := (2 / X [w, r] ^2) (2 n + 1) Re [a [n, X [w, r], M [w]] + b [n, X [w, r], M [w]]]

Qabs [n_, w_, r_] := Qext [n, w, r] – Qsca [n, w, r]

E.4. Figures and references

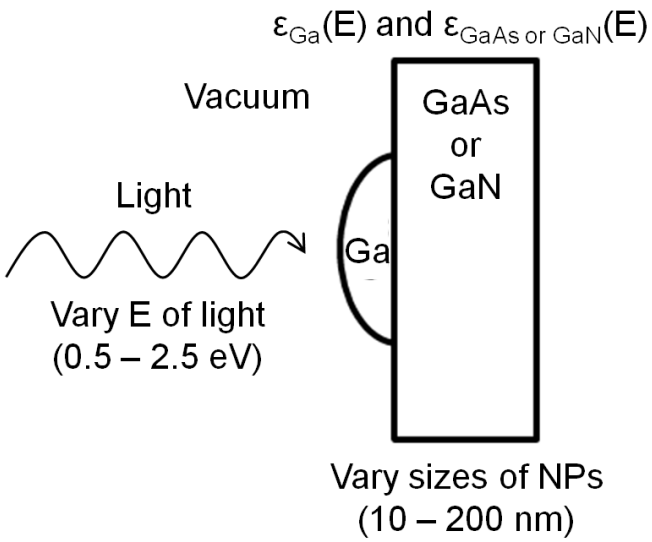

Fig. E.1. A schematic diagram showing the conditions reflected in the Mie analytical solution to Maxwell equations.

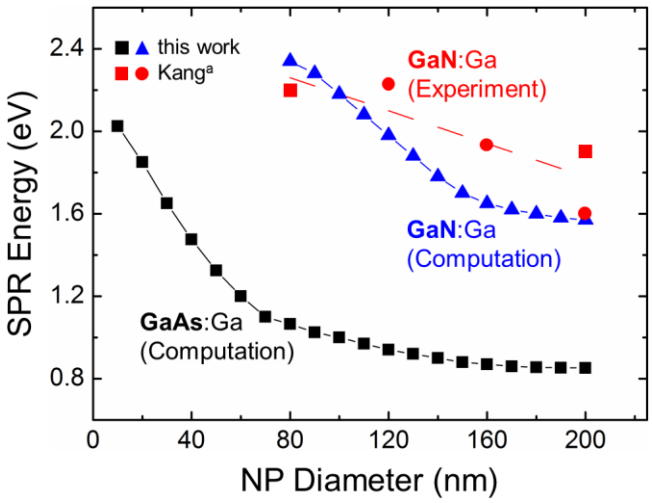

Fig. E.2. SPR energy vs. NP diameter for Ga NPs on GaAs (computation) and GaN (computation and experiment) surfaces. SPR energies are inversely proportional to the Ga NP diameter. It is interesting to note that the computed SPR energies for Ga NPs on GaN surfaces match measured data well, and the SPR energies are very different for Ga NPs on GaAs and GaN surfaces. [a]See Ref. 5.

[1]G. Mie, *Ann. Phys.* **25**, 377 (1908).

[2]C. Bohren and D. Huffman, *Absorption and Scattering of Light by Small Particles.* (John Wiley & Sons, New York, 1982).

[3]C. Sonnichsen, Ph.D thesis (University of Munich, 2001).

[4]Literature values for the spectral dependence of the dielectric permittivities of GaAs [P. C. Wu, Ph.D thesis (Duke University, 2009)], GaN [Y. H. Tu, C. M. Kwei, and C. J. Tung, *Surf. Sci.* **601**, 865 (2007)], and Ga NPs [M. Scalora, M. A. Vincenti, V. Roppo, J. V. Foreman, J. W. Haus, N. Akozbek, and M. J. Bloemer, *IEEE.* **132** (2009)] are used.

[5]M. Kang, T. W. Saucer, M. V. Warren, J. H. Wu, H. Sun, V. Sih, and R. S. Goldman, *Appl. Phys. Lett.* **101**, 081905 (2012).

[6]P. C. Wu, M. Losurdo, T. H. Kim, M. Giangregorio, G. Bruno, H. O. Everitt, and A. S. Brown, *Langmuir* **25**, 924 (2009).

Appendix F

Materials Parameters

In this appendix, several materials parameters used in the calculations of motion and PL studies are summarized in table F.1.

Table F.1. Values of *M*, *Z*, and *U* used in the calculation of formation study.

	***M* (g/mol)**[1]	***Z***[1]	***U* (eV)**[1]
Ga	69.723	31	2.81
In	114.820	49	2.52
Al	26.982	13	3.39
As	74.922	33	2.96
P	30.974	15	3.43
N	14.007	7	4.92
Sb	121.750	51	2.75

Table F.2. Values of v, μ, θ_A, θ_B, $d\gamma/dT$, γ_{Ga}, R, and J used in the calculation of motion study

Parameter	**Value**
v (m/s)	6.19×10^{-9} - 5.26×10^{-8}
μ (kg/sm)	2.13×10^{-3}
θ_A (degree)	26.66 - 43.1
θ_B (degree)	32.5 - 52.3
$d\gamma/dT$ (kg/s^{2o}C)^2	-0.066
γ_{Ga} (Kg/s^2)^2	0.708
R (m)	1.25×10^{-7} - 1.73×10^{-7}
J (m^{-1})	1.47×10^{5}

Table F.3. Values of ε_{Ga} and ε_{GaAs} used in the calculation of PL study

Wavelength (nm)	Ga[3]		GaAs[4]	
	Real part	Imaginary part	Real part	Imaginary part
400	-4.500	4.235	14.600	18.600
420	-4.958	4.362	17.600	14.800
440	-5.546	4.556	20.600	11.000
460	-5.874	4.801	20.300	8.200
480	-6.332	5.088	20.000	5.400
500	-6.790	5.410	18.700	4.200
520	-7.145	5.760	17.400	3.000
540	-7.500	6.136	16.700	2.600
560	-7.858	6.533	16.000	2.200
580	-8.215	6.948	15.700	2.000
600	-8.573	7.378	15.400	1.800
620	-8.930	7.822	15.000	1.700
640	-9.144	8.277	14.600	1.600
660	-9.358	8.742	14.450	1.500
680	-9.572	9.216	14.300	1.400
700	-9.786	9.695	14.150	1.200
720	-10.000	10.181	14.000	1.000
740	-10.214	10.670	13.925	0.900
760	-10.428	11.163	13.850	0.800
780	-10.642	11.658	13.775	0.700
800	-10.856	12.154	13.700	0.600
820	-11.070	12.651	13.625	0.500
840	-10.535	13.148	13.550	0.400
860	-10.000	13.643	13.475	0.200
880	-10.830	14.138	13.400	0.000
900	-11.660	14.631	13.000	0.000
920	-12.500	15.121	12.600	0.000
940	-12.320	15.609	12.450	0.000
960	-12.140	16.093	12.300	0.000
980	-12.320	16.574	12.150	0.000
1000	-12.500	17.051	12.000	0.000
1020	-11.605	17.525	11.990	0.000
1040	-10.710	17.994	11.980	0.000
1060	-10.934	18.459	11.970	0.000
1080	-11.158	18.919	11.960	0.000
1100	-11.382	19.375	11.950	0.000
1120	-11.606	19.826	11.940	0.000
1140	-11.830	20.272	11.930	0.000
1160	-12.054	20.714	11.920	0.000
1180	-12.278	21.150	11.910	0.000
1200	-12.500	21.581	11.900	0.000

References

[1]J. Tesmer and M. Nastasi, *Handbook of Modern Ion Beam Materials Analysis*; Materials Research Society: PA, 1995.

[2]M. L. Ford and A. Nadim, *Phys. Fluids* **6**, 3183 (1994).

[3]P. C. Wu, M. Losurdo, T. H. Kim, M. Giangregorio, G. Bruno, H. O. Everitt, and A. S. Brown, *Langmuir* **25**, 924 (2009).

[4]M. Scalora, M. A. Vincenti, V. Roppo, J. V. Foreman, J. W. Haus, N. Akozbek, and M. J. Bloemer, *IEEE WTM* 130 (2009).